TAMPEREEN TEKNILLINEN YLIOPISTO
TAMPERE UNIVERSITY OF TECHNOLOGY

Tuomo Nyyssönen

# Quenching and Partitioning of High-Aluminum Steels

Julkaisu 1451 • Publication 1451

Tampere 2017

Tampereen teknillinen yliopisto. Julkaisu 1451
Tampere University of Technology. Publication 1451

Tuomo Nyyssönen

# Quenching and Partitioning of High-Aluminum Steels

Thesis for the degree of Doctor of Science in Technology to be presented with due permission for public examination and criticism in Festia Building, Auditorium Pieni Sali 1, at Tampere University of Technology, on the 13th of January 2017, at 12 noon.

Tampereen teknillinen yliopisto - Tampere University of Technology
Tampere 2017

ISBN 978-952-15-3892-6 (printed)
ISBN 978-952-15-3896-4 (PDF)
ISSN 1459-2045

# ABSTRACT

The quenching and partitioning response of aluminum-containing steels was investigated primarily through dilatometry and microstructural analysis through electron backscatter diffraction. It was found that 2-3 wt-% aluminum content raises the $Ac_3$ temperature to levels that cannot be predicted by current thermodynamic models. New information was gained on the nucleation and austenite growth behavior of high-aluminum steels during intercritical annealing. The exact orientation relationship between intercritical austenite and ferrite for high-aluminum steels was also determined.

Quenching the material from an intercritically annealed state into temperatures between $M_s$ and $M_f$ results in a partially complete martensitic transformation, after which the steel can be partitioned at 450 °C for extended periods with no excessive austenite decomposition, resulting instead in the migration of the supersaturated carbon from the martensite to the austenite phase, stabilizing it to room temperature. The resulting microstructure has a comparable strength to a corresponding dual-phase steel microstructure with an improved uniform elongation. It was found that the microstructure is very sensitive to heating rate and intercritical annealing conditions, necessitating good process control during initial annealing.

A fully automated iterative algorithm was developed for the reconstruction of austenite orientation maps from electron backscatter diffraction data. The algorithm determines the correct orientation relationship from the boundary misorientations between martensitic blocks. The determined orientation relationship is then used to assemble a graph cluster from the boundary misorientations, which is then divided into discrete clusters using Markov cluster analysis. The austenite orientation map can finally be reconstructed from the resulting discrete cluster network. The method is fast, can be used for the automatic analysis of datasets measured with both fine and coarse step sizes and is suitable for previously challenging microstructures, such as fully bainitic or partially martensitic-bainitic microstructures.

In this work, the developed algorithm was used to analyze the intercritical austenite-ferrite microstructure reconstructed from the EBSD data of quenched, intercritically annealed steel. It was found that the austenite nucleates after the recrystallization of ferrite on the ferrite grain boundaries, typically sharing a Kurdjumov-Sachs-type grain boundary with one or more neighboring ferrite grains. The orientation relationship between the intercritical ferrite and austenite could be measured accurately from the reconstructed data. The reconstruction also gave direct access to the intercritical austenite grain size and the phase fractions. It was found that the nucleation of austenite is relatively fast, after which austenite grain growth occurs primarily through slow reconstructive interfacial growth into the direction of ferritic grains with incoherent phase boundaries with the growing austenite.

# PREFACE

The work presented here was, for the most part, carried out at the Department of Materials Science, Tampere University of Technology during 2012-2016. The work was financed by the Graduate School CE Tampere and SSAB. The work was guided by Professor Veli-Tapani Kuokkala and Assoc. professor Pasi Peura. I thank them both for their advice and the trust they have put in me and my work during these years.

I give special thanks to Dr. Matti Isakov for his help with the orientation relationship determination and reconstruction algorithm. The staff and members of the Department of Materials Science also deserve thanks for their support. The Department has been a very good environment to work and develop my skills as a metallurgist and crystallographer. I also appreciate the help and support from the Materials Engineering and Production Technology Research Group at the University of Oulu given to me in the beginning of this project.

I thank Emil Aaltonen Foundation, Walter Ahlström Foundation, KAUTE Foundation and TES Foundation for their financial support. I am also grateful to the Advanced Steel Processing and Products Research Center at the Colorado School of Mines for my period as a visiting scholar there. The time spent at ASPPRC was extremely helpful and significantly advanced my studies.

Tampere, December 14, 2016

Tuomo Nyyssönen

# AUTHOR'S CONTRIBUTION

The author performed the calculations and numerical simulations presented in the thesis and designed the alloys and the heat treatment parameters. He planned and conducted the dilatometry experiments, heat treatments, XRD studies, tensile tests and the electron microscopy studies. He developed the iterative method for orientation relationship determination and orientation map reconstruction with help from Dr. Matti Isakov. The author also evaluated and interpreted all the results presented in the thesis.

The Mössbauer measurements were conducted and the results interpreted by professor Don Williamson at the Department of Physics of the Colorado School of Mines. The TEM characterization was conducted by Dr. Mari Honkanen at the Department of Materials Science of the Tampere University of Technology.

The material concerning the iterative method for orientation relationship determination in Sections 4.3 and 5.1 has, for the major part, been already published in Metallurgical and Materials Transactions A [1].

The manuscript was written by the author and commented by the supervisors, Professor Veli-Tapani Kuokkala and Assoc. professor Pasi Peura.

# LIST OF SYMBOLS AND ABBREVIATIONS

*Greek symbols*

| | |
|---|---|
| $\alpha$ | Ferrite phase |
| $\alpha'$ | Martensite phase |
| $\Delta F^{\gamma \rightarrow \alpha' *}$ | Critical driving force for martensitic transformation |
| $\Delta G^{\gamma \rightarrow \alpha}$ | Free energy difference between austenite and ferrite |
| $\Delta G^{\gamma \rightarrow \alpha'}$ | Free energy difference between austenite and martensite |
| $\Delta G^{\gamma}$ | Free energy of austenite |
| $\Delta G^{\alpha}$ | Free energy of ferrite |
| $\Gamma_C^{\alpha}$ | Henrian activity coefficient of carbon in ferrite |
| $\Gamma_C^{\gamma}$ | Henrian activity coefficient of carbon in austenite |
| $\gamma$ | Austenite phase |

*Latin symbols*

| | |
|---|---|
| $a_x$ | Lattice parameter of phase $x$ |
| $C_i$ | Crystallographic symmetry operator $i$ |
| $f$ | Volumetric fraction |
| $G_{Zener}$ | Zener ordering energy |
| $L_{\gamma}$ | Grain size of parent austenite |
| $M$ | Misorientation |
| $M_s$ | Martensite start temperature |
| $O_{\gamma}$ | Austenite crystallographic orientation |
| $O_{\alpha}, i$ | Martensite crystallographic orientation $i$ |
| $R$ | Universal gas constant |
| $T$ | Temperature |
| $T_P$ | Partitioning temperature |
| $T_Q$ | Initial quench temperature |
| $T_{\gamma \rightarrow \alpha}$ | Orientation relationship between $\alpha$ and $\gamma$ |
| $V$ | Volume |
| $V_m$ | Volume fraction of martensite |
| $W_0^X$ | Frictional work of element $X$ |
| $X_k^l$ | Concentration of alloying element $k$ in phase $l$ |

*Abbreviations*

| | |
|---|---|
| bcc | Body-centered cubic crystal structure |
| EBSD | Electron Backscatter Diffraction |
| EPMA | Electron probe microanalysis |
| fcc | Face-centered cubic crystal structure |
| IPF | Inverse pole figure |
| K-M | Koistinen-Marburger |
| K-S | Kurdjumov-Sachs |
| MCL | Markov Cluster analysis |
| N-W | Nishiyama-Wassermann |
| ODF | Orientation density function |
| OR | Orientation relationship |
| Q&P | Quenching and partitioning |
| RT | Room temperature |
| XRD | X-ray diffraction |

# Contents

# 1 Introduction

Technological progress places ever-stricter demands on the strength and toughness of sheet steels. Traditionally, these two properties have been thought of as mutually exclusive. The resolution of the conflict between strength and toughness has been one of the primary goals of steel research in the last few decades. The old notion of grain refinement to increase strength by hindering the movement of dislocations has to be combined with some way to increase elongation; in other words, to prevent or suppress the events leading to necking and, eventually, to rupture. The phase transformation from austenite to martensite as the result of deformation has been succesfully employed to this end. Some method to produce a microstructure containing both fine-grained martensite and a sufficient amount of retained austenite is therefore desirable.

Quenching and partitioning (Q&P) is one such method. By interrupting the martensitic transformation and stabilizing the retained austenite with carbon partitioned from the transformed martensite, a microstructure consisting of fine martensitic laths and retained austenite films can be produced. The heat treatment relies on assumptions whose experimental verification requires sophisticated characterization methods. The expected microstructure contains features such as nanoscale film-like retained austenite and nanosized carbides embedded in a similarly nanoscale lath martensite matrix. Visual observation through optical or electron microscopy is not enough to reliably identify these features, necessitating crystallographic studies. Through methods such as electron backscatter diffraction (EBSD), spatial maps of crystallographic orientations can be constructed, providing large amounts of data on the various phases and their crystallographic relationships in the microstructure. The sheer amount of data obtained in this way makes it necessary to develop new analytical tools for proper statistical analysis.

Quenching and partitioning has been shown to produce excellent mechanical properties for silicon-alloyed steels quenched from a fully austenitized condition. However, the necessity to quench the steel from a fully austenitized state to an intermediate homogeneous temperature (in the 200-350 °C range) would require significant adjustments to existing annealing lines, requiring considerable investments. In addition, silicon makes hot dip galvanization a very difficult procedure, precluding the use of these alloys in applications where corrosion protection is a necessity. This is a big hindrance, considering that the major target application for high-strength steels is the automotive industry. Finally, before client companies can adopt the new Q&P alloys, new production methods and structural designs are required to fully take advantage of the enhanced properties. Incremental improvements are still necessary before taking the next big leap forward.

A logical step on the way to adopting quenched and partitioned microstructures in steel-based industry would be the development of an intermediate-level alloy in terms of strength, which would still benefit from the increased formability resulting from the Q&P treatment. A dual-phase steel with a quenched and partitioned microstructure replacing the marten-

sitic phase would fill these requirements. Preferentially, the steel should also be galvanizable with the current level of technology. Aluminum is an alloying element that can be used to achieve the same effect as silicon, and it has been shown to cause less problems in hot dip galvanizing [2].

With this in mind, the research question of the thesis can be summarized as follows:

*Can aluminum alloyed steel processed with the Q&P route be used to produce DP steels with improved elongation and a microstructure with metastable retained austenite intermixed within the martensitic islands?*

To answer this question, a broad literature survey and a considerable amount of experimental work consisting of alloy and heat treatment design, dilatometry and mechanical and microstructural characterization had to be carried out. Chapter 2 describes the quenching and partitioning method and the state of the art, Chapter 3 discusses the relevant crystallography to the martensitic transformation, Chapter 4 summarizes the experimental methodology used in this work and Chapter 5 describes and discusses the experimental results. The research question is readdressed and the concluding remarks are given in Chapter 6.

The scientific contributions resulting from this work are:

1. A fully automated analytical tool was developed for determining the orientation relationship between martensite and austenite and for reconstructing the parent austenite orientations and microstructure from martensitic EBSD data. The analytical tool was used for the crystallographic characterization of the microstructures quenched from fully austenitized and intercritically annealed states.

2. The quenching behavior of steels with an unconventionally high aluminum content was characterized when quenched from an intercritically annealed state.

3. It was shown that the parent austenite orientation maps in the intercritically annealed steels could be reconstructed from the recorded EBSD data using the fully automated algorithm proposed in the thesis. The morphology, orientations and the phase fraction of the parent austenite phase could then be accessed directly from the reconstructed data and the orientation relationship of the austenite with neighboring intercritical ferrite could be measured exactly.

4. It was demonstrated that 2-3 wt-% aluminum content in a steel prevents the formation of carbides in martensite formed into intercritical austenite when held at 450 °C after interrupted quenching, even at extended partitioning times of 1000 s. Instead of forming carbides, the supersaturated carbon in the martensite diffuses into austenite, giving it metastability at room temperature.

# 2 Quenching and Partitioning

Lath-shaped martensite is a commonly occurring martensite morphology in most modern high-strength steels. The laths are formed from the parent austenite grains by a displacive transformation when an austenitized steel is rapidly cooled to temperatures where the diffusive movement of iron atoms is too slow for a reconstructive phase transformation [3].

The martensite morphology varies according to the chemical composition and especially the carbon content of the steel [4]. For steels with a total carbon content of approximately 0.2 weight percent, the laths are grouped together into blocks, which in turn form packets, as shown in Figure 2.1. The high-angle boundaries between the packets and the blocks act as obstacles to dislocation movement, granting improved tensile strength and fracture resistance upon the material. It bears mentioning that some boundaries between martensitic laths are not high-angle ones: Morito et al. [5] classified certain martensitic variant combinations as sub-blocks on account of their low mutual misorientation angle. In any case, fully martensitic microstructures are typically characterized by a high strength but relatively low uniform elongation.

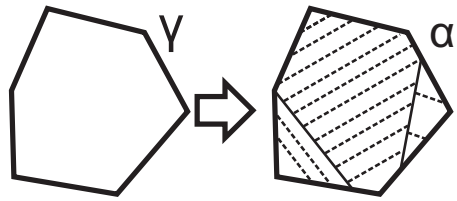


**Figure 2.1:** *Schematic presentation of a parent austenite grain (left) transformed to martensite [5]. Packet boundaries are indicated by thin solid lines and block boundaries by thin dotted lines.*

Quenching and partitioning (Q&P) is a heat treatment process proposed by Speer et al. [6] in 2003 to address the toughness issues of martensitic alloys while preserving high strength. The goal is a microstructure that has undergone an unfinished martensitic transformation, resulting in a mixture of transformed martensite and untransformed retained austenite. The austenite is further stabilized to room temperature by carbon diffusing from the martensitic phase to the austenite. The process is visualized schematically in Figure 2.2. Ideally, retained austenite appears as nanometer scale thin films between the martensitic laths in the Q&P microstructures. In practice, at least three distinct morphologies are frequently encountered: nanoscale interlath [7–11], bulkier interblock [7,12,13], and bulky epitaxial [12] retained austenite.

The Q&P process is based on several key assumptions:

1. The martensite transformation is assumed to be completely athermal. The degree of

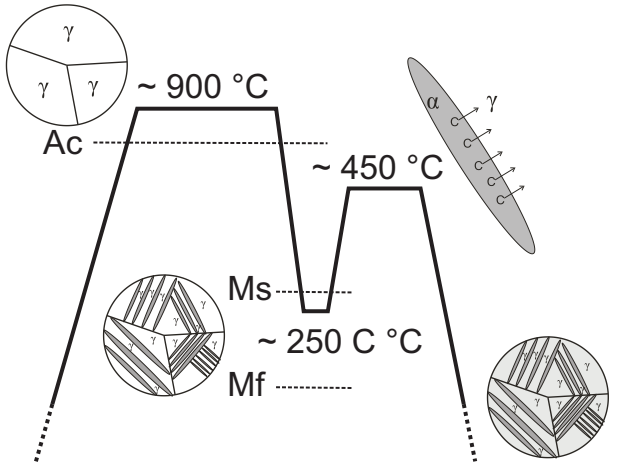


**Figure 2.2:** *Schematic presentation of the quenching and partitioning process as proposed by Speer et al. [14].*

transformation can therefore be controlled by quenching the steel to a predetermined temperature. Martensite formation thermodynamics and kinetics are discussed in Chapter 2.1.

2. There is no movement of carbon between the phases during the displacive transformation of austenite to martensite. Thus the martensite is in a supersaturated state immediately following the transformation. Afterwards, the carbon atoms can move diffusionally across the phase boundaries, thus migrating (partitioning) to the retained austenite from the supersaturated martensite. This assumption is based on the constrained paraequilibrium (hereafter referred to as CPE) condition, which is discussed in Chapter 2.3.

3. During the partitioning of carbon, iron atoms remain immobile.

4. There are no competitive processes (such as carbide precipitation) to hinder the partitioning of carbon between the phases.

The expected microstructure for a Q&P processed steel is martensite with controlled amounts of filmlike retained austenite between the martensitic laths. The primary goal of alloying is threefold. The first goal is to enable martensite formation in a practical temperature range where quenching can be halted at a specific temperature as per item 1. The second goal is to suppress or delay carbide formation so that carbon is free to diffuse from the martensite to the austenitic phase without competing reactions (item 3). The first condition can be easily controlled with carbon content, as discussed in Section 2.1. The second condition is most commonly satisfied by alloying with an element that is insoluble in cementite [15], necessitating the diffusion of the element out of the base matrix prior to precipitation. The element most commonly used for precipitation suppression is silicon [8, 10, 11, 16, 17]. Aluminum [12, 18, 19] has been studied as well to a lesser extent, as well as the effect of nickel, chromium [20] and manganese additions [7, 21]. Finally, the alloy must contain enough carbon to stabilize a desired amount of retained austenite to room temperature. A carbon

content of 0.2 wt-% is a typical value, allowing for the stabilization of approximately 15 vol-% of retained austenite at room temperature when calculated using the methodology of Speer et al. [14].

In this Chapter the Q&P process is discussed starting from the onset and athermal progression of the martensite transformation during quenching to the thermodynamics of the constrained paraequilibrium condition during partitioning.

## 2.1 Martensite formation

Martensite forms when a steel is first annealed at a temperature sufficient to promote the nucleation of austenite and then quenched rapidly to a suitably low temperature. The cooling must be rapid enough so that there is insufficient time for a diffusion-controlled phase transformation to ferrite. The driving force for the transformation increases with decreasing temperature, resulting in a shear transformation of the face centered cubic lattice of austenite to body-centered tetragonal [22] or, in the case of carbon contents lower than approximately 0.6 wt-%, body-centered cubic martensite [23, 24]. The transformation occurs as a series of small-scale displacements of atoms across a moving semicoherent interface. The result is the formation of lenticular martensitic laths inside the parent austenite grains. As the transformation progresses, new laths are formed inside the parent austenite grains until all of the austenite has transformed. Martensite crystallography theory is discussed in more detail in Chapter 3.1.

The ability to predict the temperature of the onset of the martensitic transformation ($M_s$ for short) as well as the progression of the transformation with respect to temperature is crucial with regard to Q&P heat treatment design. Speer et al. [14] proposed that the ferritic laths formed in an unfinished martensitic transformation have the potential to act as constrained boundaries as per the CPE model. Carbon in the supersaturated martensite would then be free to diffuse to the film-like retained austenite between the laths as predicted by the model, if competing mechanisms have been suppressed or sufficiently delayed.

Several empirical and physical models for predicting the $M_s$ temperature have been proposed over the years. The empirical models typically assume a linear relationship between alloying content and $M_s$, such as in Equation 2.1 proposed by Stuhlmann [25]:

$$M_s(^\circ\mathrm{C}) = 550 - 350C - 40Mn - 20Cr - 10Mo - 17Ni - 8W - 35V - 10Cu + 15Co + 30Al \quad (2.1)$$

In Equation 2.1, the variables stand for the mass fractions of the respective alloying elements in $\mathrm{wt} - \%$. When using empirical equations, it must be kept in mind that they are typically limited to only a narrow composition range of alloys and an experimental verification should always be carried out.

A more general approach to predicting $M_s$ is to use free energy equations by balancing the critical driving force necessary for martensitic transformation against the resulting change in free energy accompanying the transformation. This is shown schematically in Figure 2.3.

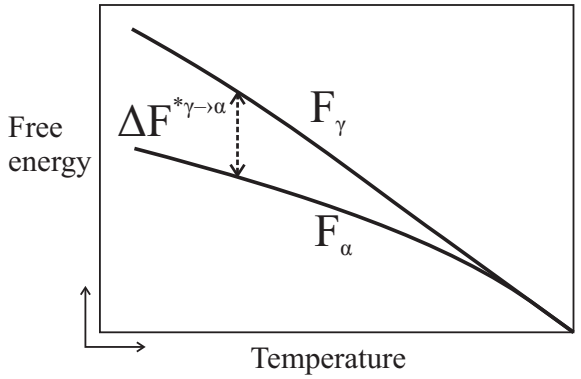


**Figure 2.3:** *Schematic representation of the free energies of ferrite ($F^{\alpha}$) and austenite ($F^{\gamma}$) with respect to temperature. The critical driving force $\Delta F^{\gamma\rightarrow\alpha}*$ necessary to initiate the martensitic transformation is shown as the difference between the two curves. [26]*

The free energy difference is the difference between the free energy of austenite and the free energy of ferrite of the same composition, $\Delta G^{\gamma\rightarrow\alpha} = G^{\alpha} - G^{\gamma}$. The calculation of the energies of both phases involves terms for free energy, mixing entropy and magnetic contributions. In addition, Zener ordering energy has to be taken into account. The free energy difference acting as a driving force for the martensitic transformation is then given as $\Delta G^{\gamma\rightarrow\alpha'} = \Delta G^{\gamma\rightarrow\alpha} + G_{Zener}$.

One such model was proposed by Bhadeshia [26, 27] in 1981. In this model, substitutional alloying atoms in the austenite phase are taken into account by averaging their effect on the magnetic and non-magnetic components of the free energy change. The available driving force for the martensitic transformation at a given temperature is then calculated and compared to the critical driving force. The general assumption is, of course, that the amount of compositional elements does not exceed the saturation limit of the solid solution. The method of Bhadeshia et al. [26] covers a broad range of low-alloy steels, but slightly overestimates $M_s$ when compared to a large amount of experimental data. A full account of the method as it is used in this work is given in Appendix 1.

All thermodynamic models used to predict the $M_s$ temperature have to make some estimation as to the critical driving force required to start the transformation. In the case of Bhadeshia's model, the assumption is that the critical driving force (or the driving force at $M_s$) for the martensitic transformation increases monotonically with carbon content:

$$\Delta F_{M_s}^{\gamma\rightarrow\alpha'*} = -1026 - 10568x; \tag{2.2}$$

where $x$ is the carbon content of the alloy in at-%. This linear estimation is based on empirical data. According to Ghosh and Olson [28], the critical driving force can be thought of as the frictional work of a forming martensitic interface. It consists of two terms, the first including strain and interfacial energies of the forming martensite lath and the second the interfacial frictional work between the austenite matrix and the martensite nucleus. The

second term is composition dependent and the whole equation is given as:

$$-\Delta F_{M_s}^{\gamma\rightarrow\alpha'} = W_0^{Fe} + \sqrt{\sum_i (K_o^i X_i^{0.5})^2} + \sqrt{\sum_j (K_o^j X_j^{0.5})^2} + \sqrt{\sum_k (K_o^k X_k^{0.5})^2} + K_0^{Co} X_{Co}^{0.5} \quad (2.3)$$

where $W_0^{Fe}$ is the level of frictional work for pure iron, $X$ represents the concentration of the alloying element in at-%, and $K_0^n$ is the athermal strength factor for the fcc/bcc interface for a given solute. The sub- and superscript notation is $i$ = C, $j$ = Cr, Mn, Mo, Nb, Si, Ti, V and $k$ = Al, Cu, Ni, W. In Equation 2.3, the various solutes are divided into three categories based on the level of the strength factor, assuming a linear superposition between categories and a pythagoral superposition within a category. The $K$ values were estimated based on an empirical assessment of a large amount of experimental data. Cool and Bhadeshia [29] used Equation 2.3 in a thermodynamic model to improve the $M_s$ predictions for power plant weld steels rich in several different alloying elements.

According to Peet [30], the reliance on empirical evidence used to determine an equation for the critical driving force is a distinct weakness of thermodynamic models, as empirical equations like these may not be able to capture the interdependencies between the alloying elements. Bayesian neural network analysis can overcome this weakness to some degree. According to Bhadeshia [31], neural networks are often able to capture and model interdependencies between variables, even if the physical principles behind the phenomena are not clearly understood. With a suitable amount of experimental data, a single model can be used on a wide variety of alloy compositions. Capdevila et al. [32] have developed one such model, which could be used to assess the interdependency of Cr and C when affecting $M_s$. Conversely, linear empirical models (as well as the thermodynamic model by Bhadeshia et al. [26]) tend to assume the sensitivity of $M_s$ to carbon concentration to be independent of other alloying elements. In fact, even in binary solid solutions, there appears to be a non-linear dependence between $M_s$ and the solute concentration [33].

The weakness of neural network models is their inability to predict outside the bounds of data on which they were trained [31]. An estimation of uncertainty should therefore always be provided with a neural network prediction. In a literature review by Peet [30], commercial thermodynamic database and modeling software gave the best predictions when compared to Bayesian neural networks. Peet stated that when accompanied by an appropriate warning when the predictions have to be extrapolated outside the bounds of known data, neural networks still give useful estimations.

The $M_s$ prediction models most typically take into account only the chemical composition of the alloy, even though it has been acknowledged for some time that the transformation is affected by anything impeding the motion of the transformation interface, such as the elastic stress state of the material, prior plastic deformation, and grain size [34]. Yang et al. [35] studied the effect of parent austenite grain size on the martensite start temperature. They

found the following semi-empirical relationship fitted over a large amount of experimental data:

$$M_s^0 - T = \frac{1}{b} ln[\frac{1}{aV_\gamma}\{e^{-\frac{ln(1-f)}{m}} - 1\} + 1] \tag{2.4}$$

In the Equation, $b$ and $a$ are empirically determined fitting constants with values 1 $mm^{-3}$ and 0.2689, respectively. $f = 0.01$ represents the first detectable fraction of martensite, $m = 0.05$ represents the aspect ratio of a martensite lens. $V_\gamma$ is the volume of the parent austenite grain and is approximated by $L_\gamma^3$, $L_\gamma$ representing the grain size of the parent austenite. Figure 2.4 shows the amount of undercooling from the theoretical $M_s$ with the parent grain size; it is clear that below 20 $\mu$m, the diminishing size of the parent grain has a significant effect on the stability of austenite.

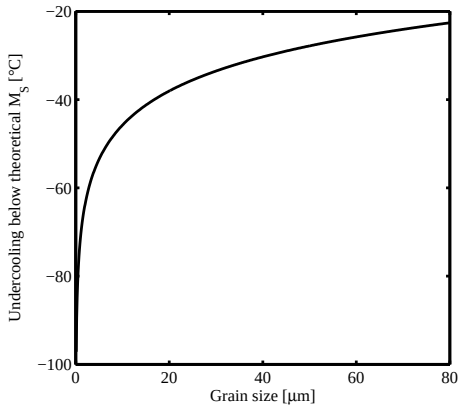


**Figure 2.4:** *Effect of parent austenite grain size on the undercooling below the $M_s$ temperature based on Equation 2.4. [35]*

Any model for determining the $M_s$ temperature shows that carbon is a very effective stabilizer of the austenitic phase. Figure 2.5 shows the effect of varying carbon content on the $M_s$ temperature of a Fe-2Mn alloy, calculated with Equation 2.1 [25] and Bhadeshia's method [26]. It is clear that the choice of the $M_s$ calculation method significantly affects the prediction of room temperature stability with regard to carbon content. Despite all the work done to predict $M_s$ temperatures either with thermodynamic equations or neural networks, any prediction made for a previously unexplored steel alloy composition should be taken with a grain of salt.

## 2.2 Athermal progression of the martensitic transformation

The progression of the martensitic transformation with respect to temperature has been empirically modeled by a number of authors. Koistinen and Marburger [36] showed in 1959

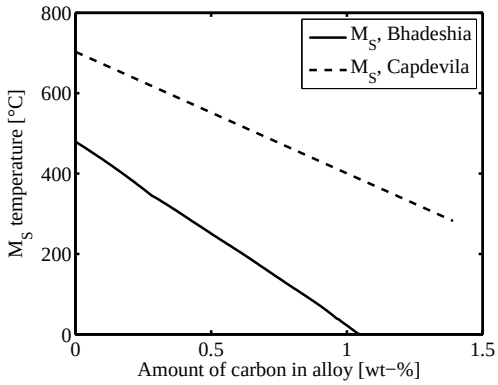


**Figure 2.5:** *Effect of carbon content on the $M_s$ temperature based on Eq. 2.15 by Capdevila et al. [32] and Eq. 7.4 by Bhadeshia et al. [26]*

.

that for plain carbon steels the martensitic fraction with respect to temperature can be modeled as 2.5:

$$V_m = 1 - e^{(-K(M_s - T))} \tag{2.5}$$

In Equation 2.5 (hereafter referred to as the K-M model), T is the temperature in K, $M_s$ is the temperature of the onset of martensitic transformation in K and $K$ is an empirically determined variable. By quenching plain carbon steels to various temperatures and measuring the retained austenite content by means of X-ray diffraction, Koistinen and Marburger determined the value of K = 0.011 to produce a good fit with the experimental data. The empirical equation was later theoretically justified by Magee [37], who based it on martensite nucleation theory.

Khan and Bhadeshia [38] modified the K-M equation to accommodate the possible effects of autocatalytic nucleation. Van Bohemen and Sietsma [39] studied the compositional dependence of the K parameter in Equation 2.5 and proposed the following relationship:

$$K_{BS}(K^{-1}) = 0.0224 - 0.0107C - 0.0007Mn - 0.00005Ni - 0.00012Cr - 0.0001Mo \tag{2.6}$$

The amount of each alloying element in Equation 2.6 is in wt-%. The Equation indicates that increasing carbon content strongly decreases the rate of the martensitic transformation. This contradicts with the K-S model, which is a general equation describing the behavior of plain carbon steels with carbon contents of 0.37, 0.50, 0.81, and 1.10 wt-% C. Van Bohemen and Sietsma [39, 40] justify the decreasing transformation rate with increasing carbon content on the shape deformation of the austenite phase next to the transformation interface. Carbon acts as a solid solution strengthener and introduces a higher degree of dislocation strengthening in the surrounding austenite matrix when martensite is first formed. The subsequent formation of martensite plates therefore requires a higher driving force, as the dislocation strengthened austenite matrix is less able to accommodate the shape change

inherent to the transformation.

The effects of alloy composition on the kinetics of martensite transformation were further investigated by Lee and Van Tyne [41]. They proposed an exponential function with two empirically determined parameters to better adjust to observed transformation curves:

$$V_m = 1 - e^{(-K_{LV}(M_s - T)^{n_{LV}})} \tag{2.7}$$

The parameters $K_{LV}$ and $n_{LV}$ are functions of the steel's chemical composition:

$$K_{LV}(K^{-1}) = 0.0231 - 0.0105C - 0.0017Mn + 0.0074Cr - 0.0193Mo \tag{2.8}$$

$$n_{LV} = 1.4304 - 1.1836C + 0.7527C^2 - 0.0258Ni - 0.0739Cr + 0.3108Mo \tag{2.9}$$

Despite the existence of alternative models, the Koistinen-Marburger model remains a popular equation for predicting the progression of the martensitic transformation [8, 11, 42, 43] in experimental Q&P treatments. In several studies the $K$ constant in Equation 2.5 has been empirically determined by curve fitting on dilatometric data [17, 20].

## 2.3 Constrained paraequilibrium condition

Under equilibrium conditions, a microstructure containing retained austenite and martensite in a binary Fe-C alloy should transform to ferrite and precipitated iron carbides [22], as indicated by the standard Fe-C phase diagram. When substitutional alloying elements are introduced, long-range diffusion at low temperatures is still limited primarily to carbon. The substitional atom - iron ratios are expected to remain unchanged in the different phases, even if migration would be favored thermodynamically. This condition is described by Hultgren [44] as paraequilibrium. Although long-range diffusion of iron and substitutional atoms is assumed to be neglibigle, phase fractions may still be adjusted via the interface migration between the phases facilitated by short-range diffusion.

Under conditions where carbide precipitation is suppressed (such as with suitable substitutional alloying), the solution will still attempt to reach conditions of minimum free energy. When austenite and ferrite are present in the alloy, this is achieved by the adjustment of the carbon contents of the phases (with long-range diffusion of carbon) and the phase fractions (via interface migration) until the chemical potential of iron and carbon in both phases is equal and the solution has reached a state of *paraequilibrium*. In *constrained paraequilibrium*, the iron and substitutional atoms are assumed to be completely immobile. The phase fractions are now fixed and the only way to achieve paraequilibrium is by the diffusion of carbon between austenite and ferrite until the chemical potential of carbon reaches equilibrium.

According to Speer et al. [6], the carbon content of the phases in a CPE state can be calculated using published thermodynamic data, specifically from the work on the chemical activity of carbon in austenite and ferrite by Geiger and Lobo [45, 46]:

$$RT \ln \frac{\Gamma_C^\alpha}{\Gamma_C^\gamma} = 76.789 - 43.8T - (169.105 - 120.4T)X_C^\gamma \tag{2.10}$$

In Equation 2.10, $\Gamma_C^\alpha$ and $\Gamma_C^\gamma$ stand for the Henrian activity coefficients for carbon in ferrite and austenite, T is the absolute temperature and R is the universal gas constant. The activity of carbon in each phase is given by the product of the activity coefficient and the mole fraction of carbon. Equation 2.10 can then be written as:

$$X_C^\gamma = X_C^\alpha e^{\frac{76.789 - 43.8T - (169.105 - 120.4T)X_C^\gamma}{RT}} \tag{2.11}$$

where $X_C^\alpha$ and $X_C^\gamma$ are the mole fractions of carbon in ferrite and austenite at a CPE state. The matter balance for iron is given by Speer et al. [6] as:

$$f_{CPE}^\gamma (1 - X_{C_{CPE}}^\gamma) = f_1^\gamma (1 - X_C^{alloy}) \tag{2.12}$$

where $f_{CPE}^\gamma$ and $f_1^\gamma$ stand for the phase fractions of austenite at the constrained paraequilibrium and initial states respectively. The total carbon content in the alloy is given by the sum of the amounts in each of the phases:

$$f_{CPE}^\alpha (X_{C_{CPE}}^\alpha) + f_{CPE}^\gamma (X_{C_{CPE}}^\gamma) = X_C^{alloy} \tag{2.13}$$

and the relationship between the phase fractions is assumed to be simply:

$$f_{CPE}^\alpha + f_{CPE}^\gamma = 1 \tag{2.14}$$

By using the matter balance equations in conjunction with Equation 2.11, the range of phase compositions at a given temperature or the carbon contents of a desired phase fraction at a range of temperatures can be calculated when given the total carbon content of a steel alloy. The equations show that when competing mechanisms have been suppressed, carbon will diffuse nearly completely to austenite. This opens possibilities for stabilizing the austenite at room temperature, preventing any further martensite transformation when the alloy is brought to room temperature from the partitioning state.

## 2.4 Method for calculating Q&P heat treatment parameters

The methodology proposed by Speer et al. [14] for the Q&P heat treatment design aims to predict the initial quenching temperature where a sufficient fraction of martensite is formed to a) enable enough carbon to be transported to the austenitic phase to stabilize it at room temperature and b) to leave a desired amount of austenite in the microstructure. For the purposes of simplifying the calculations, the kinetics of carbon partitioning are ignored here and it is assumed that full partitioning takes place: that is, all of the carbon in the martensitic phase will be diffused to the austenitic phase with no cementite or transitionary carbide formation to hinder the process. The methodology necessitates the calculation of $M_s$ temperatures and a function to predict the martensitic transformation curve for a given steel alloy composition. Functions such as Eq. 2.1 for $M_s$ calculation and Eq. 2.5 for predicting

the transformation curve based on undercooling below $M_s$ can be used for this purpose.

Initially, the $M_s$ temperature is calculated for what is assumed to be a fully austenitized steel and used to predict the martensitic transformation curve with respect to temperature. For a given quenching temperature, full partitioning is assumed to take place and the carbon content of the remaining austenite can be estimated by using the lever rule. For the final cooling, $M_s$ is recalculated taking into account the increased carbon content of the retained austenite, and Eq. 2.5 is again used to estimate the fraction of austenite that transforms to martensite upon final cooling to room temperature.

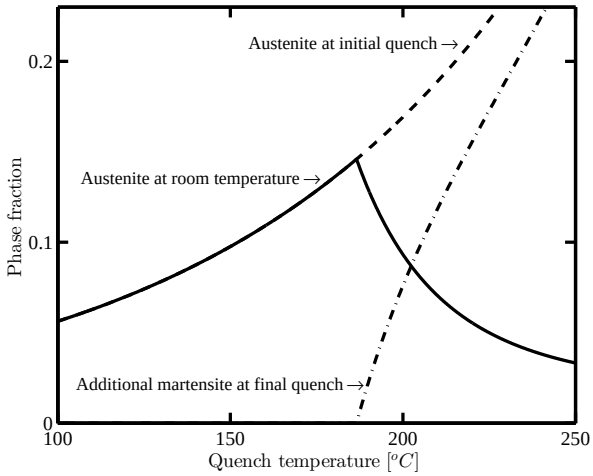


**Figure 2.6:** *An example calculation of retained austenite contents with respect to initial quench temperature using the Q&P calculation methodology proposed by Speer et al. [14]*

Figure 2.6 shows the predicted retained austenite content after a Q&P treatment for a 0.2C-1.5Si-1.5Mn steel alloy. The $M_s$ temperature was calculated using Equation 2.15 proposed by Capdevila et al. [32], and the transformation curve was determined using the K-M model presented in Equation 2.5. The model estimates the peak retained austenite content at the initial quenching temperature where the carbon content in the austenite stabilizes it at exactly room temperature (RT). When the quenching is interrupted above this initial quench temperature, the carbon content of the austenite is insufficient to prevent martensitic transformation during the final quenching to RT. Below this temperature enough austenite transforms to martensite, the excess carbon diffusing into the austenitic phase and stabilizing it to below the final quench temperature.

$$M_s(^\circ\mathrm{C}) = 762 - 302.6C - 30.6Mn \\ - 16.6Ni - 8.9Cr + 2.4Mo - 11.3Cu + 8.58Co + 7.4W - 14.5Si \quad (2.15)$$

In Eq. 2.15 [32], the variables represent mass fractions in weight percent. It must be stressed that the choice of equations for the $M_s$ calculation and for obtaining the martensite transfor-

mation curve significantly affects the predicted initial quench temperature for retaining the maximum amount of retained austenite. Figure 2.7 shows three Q&P prediction curves calculated using Equation 2.15 for calculating the $M_s$ value and three different kinetic models. The optimal quench temperature varies by more than 100 °C between the three models.

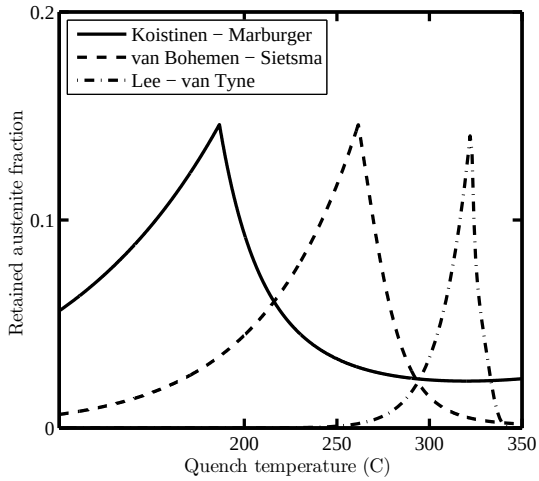


**Figure 2.7:** *An example calculation of retained austenite contents with respect to the initial quench temperature using the empirical transformation equations by Koistinen and Marburger [36], van Bohemen and Sietsma [39], and Lee and van Tyne [41].*

## 2.5 Competing mechanisms with partitioning

In practice, carbide precipitation or the formation of other phases during the partitioning step can rarely be completely suppressed, thus violating the CPE condition [12,17,47]. The observed mechanisms interfering with the partitioning phase include carbide precipitation, bainite formation and the migration of grain boundaries during partitioning.

### 2.5.1 Carbide precipitation

The formation of carbides is associated with martensite tempering, which occurs at similar time and temperature regime where partitioning also takes place. In tempering, the martensitic microstructure approaches a free energy equilibrium aided by thermal activation. As mentioned previously, carbon tied up in carbides becomes unavailable for partitioning, lessening the potential maximum amount of retained austenite in the final microstructure.

The carbides most typically associated with martensite tempering are cementite and various transition carbides. The formation of cementite occurs at temperatures of above approximately 100 °C, while transition carbides rarely appear in the final microstructure after tempering above temperatures of 250 °C if the formation of cementite is unhindered [22].

Cementite initially forms in the microstructure as a set of plates in a Widmanstätten distribution sharing an orientation relationship with the martensitic matrix [22]. As the martensitic phase becomes depleted of carbon, it loses its tetragonality and becomes ferrite. The orientation relationship between the now carbon-free ferrite and the newly formed cementite has been defined as the Bagaryatski orientation relationship, as shown in Table 2.1.

Silicon is an effective cementite formation suppressor, forming a kinetic barrier to the growth of cementite. As the solubility of silicon in cementite is very low, excess silicon must be rejected to the surrounding matrix via diffusion prior to cementite growth [48]. The substitutional diffusion of silicon is slow, extending the time necessary for cementite formation. Other elements such as aluminum, copper and phosphorus that also have a very low solubility in the cementite phase can be used to retard its growth. 1.5 wt-% silicon is generally considered to be enough to suppress cementite formation during partitioning [7, 9].

**Table 2.1:** *Orientation relationships between ferrite (martensite) and various carbides. [3]*

| | | |
|---|---|---|
| $(211)_{\alpha'} \parallel (011)_{Fe_3C}$ | Bagaryatski [3] | Cementite, $\theta$ |
| $[01\bar{1}]_{\alpha'} \parallel [100]_{Fe_3C}$ | | $Fe_3C$ |
| $[\bar{1}11]_{\alpha'} \parallel [010]_{Fe_3C}$ | | |
| $(101)_{\alpha'} \parallel (101\bar{1})_{\epsilon}$ | Jack [22] | $\epsilon$-carbide |
| $(011)_{\alpha'} \parallel (0001)_{\epsilon}$ | | $Fe_2C/Fe_3C$ |
| $[11\bar{1}]_{\alpha'} \parallel [12\bar{1}0]_{\epsilon}$ | | |
| $(010)_{\alpha'} \parallel (110)_{\eta}$ | Hirotsu et al. [49] | $\eta$-carbide |
| $[100]_{\alpha'} \parallel [001]_{\eta}$ | | $Fe_2C/Fe_3C$ |
| $(100)_{\alpha'} \parallel (0\bar{1}1)_{NbC}$ | Baker-Nutting [50] | $NbC$ |
| $[010]_{\alpha'} \parallel [011]_{NbC}$ | | |

Transition carbides appear before cementite during the initial stages of tempering, forming on the cube planes of the carbon-saturated martensite matrix. The $\epsilon$-carbide has a close-packed hexagonal structure, forming as rods or platelets and sharing the Jack orientation relationship with the martensite matrix, shown in 2.1 [22]. It should be noted that the precipitation of this type of carbide may occur even prior to the partitioning step, if the quench interruption temperature (QT) is high enough and the isothermal holding time at this temperature before partitioning is sufficient. Another commonly observed carbide is the $\eta$-carbide with an orthorhombic structure. The two carbides are difficult to distinguish, as the hexagonal structure of the $\epsilon$-carbide may be transformed into an orthorhombic structure with lattice parameters of $a_{\epsilon'} = \sqrt{3}a_{\epsilon}$, $b_{\epsilon'} = c_{\epsilon'}$ and $a_{\epsilon'} = a_{\epsilon}$ that are very close to those of $\eta$ [51]. The morphology of $\eta$ is also similar to that of $\epsilon$, with the carbide appearing as sets of platelets that may be arranged in crosswise patterns [17]. The carbides were observed by Hirotsu et al. [49] after tempering a martensitic 0.45C steel for 1-40 days at 120 °C and 1-3 hours at 200 °C. The carbides were found to have a well-defined orientation relationship to

the tempered martensite matrix, shown in Table 2.1.

Substitutional alloying with aluminum or silicon is not as effective a deterrent against the formation of $\epsilon$- or $\eta$-carbides as against cementite [52, 53]. It has been reported that silicon is not rejected into the surrounding matrix in a similar magnitude from $\epsilon$-carbides as it does from cementite [54]. According to *ab initio* calculations by Jang et al. [55], silicon addition improves the coherency of the $\epsilon$-carbide with the martensitic lattice, resulting in improved stability over cementite. Aluminum additions, on the other hand, were calculated to reduce coherency. HajyAkbary et al. [56] observed the formation of $\epsilon$-carbides in the martensitic matrix in a 0.3C-1.6Si-3.5Mn steel after 5 s of isothermal holding at 400 °C. The carbide fraction in the microstructure was found to decrease with increasing partitioning time. Conversely, the carbon content of the retained austenite increased when the holding time at the partitioning temperature was increased. It was proposed that rather than transforming into cementite, the $\epsilon$-carbides are re-dissolved during extended holding at the partitioning temperature, after which the excess carbon becomes available for partitioning to the retained austenite. It should be noted that the carbides were identified through TEM observation of the lattice parameter and the orientation relationship with the matrix, with only $\epsilon$-carbides and cementite considered as candidates.

Pierce et al. [17, 57] found that transition carbide formation took place both immediately after interrupted quenching at 225 °C as well as during partitioning afterwards at 400 and 450 °C for a 0.38C-1.54Mn-1.48Si steel alloy austenitized at 820 °C. In this case, the carbides were characterized as $\eta$-type in TEM studies based on lattice parameter analysis and orientation relationship determination. The plate-like $\eta$ formations were interspersed within a ferritic (martensitic) matrix. The amount of carbides were found to initially decrease during partitioning until 30 s, after which point austenite decomposition to ferrite and cementite was found to occur. Pierce et al. [57] attributed the apparent initial decrease in the $\eta$ fraction to reduced precipitation rather than to dissolution of existing carbides. In any case, it was shown that carbide formation was in competition with partitioning at both partitioning temperatures.

Additions of small amounts of rare earth elements such as niobium or vanadium may result in the formation of small, complex carbides during partitioning [8]. Zhou et al. [8] found that partitioning a 0.25C-1.5Mn-1.2Si-1.5Ni-0.05Nb steel at 350 °C for 30 s resulted in the formation of $\epsilon$-type transition carbides, while at a partitioning temperature of 425 °C for 30 s complex niobium carbides were formed. The carbides generally had a spherical morphology with a size of 20 $\pm$5 nm. In addition to niobium carbides, globular cementite was found and presumed to have formed as a result of decomposing austenite after a 3600 s partitioning at 425 °C. Wang et al. [58] found that for a 0.5C-1.2Mn-1.2Si-1Ni-0.2Nb steel, partitioning at 400 °C for 10 s to 1800 s resulted in continuous nucleation and growth of small-sized globular niobium carbides. After 10 s of partitioning, $\epsilon$-carbides with a Jack orientation relationship were also found to have formed. After extended partitioning, no $\epsilon$-carbides were found and they were assumed to have decomposed. Wang et al. [59] observed similar behavior in a 0.25C-1.5Mn-1.2Si-1.5Ni-0.05Nb steel partitioned for 30 s at 400 °C. Fine (10-20 nm) NbC carbides were found dispersed in the tempered martensite matrix. In both studies [58,59] the carbides were found to have a Baker-Nutting [50] orientation relationship with the parent matrix (shown in Table 2.1). After extended tempering at 400 °C, the carbides disappear

and are replaced by globular cementite.

### 2.5.2 Formation of isothermal martensite

The decomposition of austenite has also been observed during holding at temperatures above $M_s$ but below the regimes of reconstructive phase transformations or bainite formation [60]. In such cases, the term isothermal martensite is often applied, as the newly formed phase has a similar morphology to martensite and its formation is not associated with carbide formation. The critical temperature for isothermal martensite formation is denoted $M_{si}$ [61]. Below this temperature martensite can form as a function of time and can be described by C-curves in a similar manner to diffusional transformations of austenite. According to a broad literature survey by Borgenstam and Hillert [60], the phenomenon has been observed on plain carbon steels at a temperature range of room temperature up to above 300 °C, at specific temperatures both above and below $M_s$.

Kurdjumov [62] proposed in 1960 that the formation of isothermal martensite occurs in a similar manner to athermal martensite. The transformation starts when a martensite embryo located at a potential nucleation site reaches a supercritical size and develops into fast growing martensite; in the case of athermal transformation, the growth of an embryo is so fast that it has no time to be observed. Borgenstam and Hillert [61] modeled the embryo growth process as a series of reactions either promoting or hindering growth, which after some time results in the formation of martensite.

From a Q&P point of view, the formation of isothermal martensite is not strictly in competition with partitioning if the partitioning temperature is higher than $M_{si}$. However, the situation is not straightforward after athermal martensite formation has already occurred during the quenching step. Also, it should be noted that the steel should not be held at the quenching temperature longer than strictly necessary to prevent (as far as possible) the formation of isothermal martensite.

### 2.5.3 Austenite decomposition to bainite

De Moor et al. [18] studied the effects of varying silicon and aluminum contents on Q&P processing. They found that increased partitioning times generally lead to a lower retained austenite fraction at room temperature for fully austenitized steels. Increasing the aluminum content in particular led to a sharp decrease in the retained austenite content with increased partitioning times at temperatures of 350 and 450 °C. The exact mechanism of retained austenite decomposition was not identified, although it was observed in dilatometric experiments that it was related to a volume expansion during partitioning.

The volume expansion during the partitioning step has also been observed by Santofimia et al. [20]. A possible mechanism for this behavior is the formation of bainite from austenite, suggested by both Santofimia et al. [20] and de Moor et al. [18]. It was observed by Mahieu et al. [63] that when quenching directly to a temperature of 400 or 450 °C and holding for 10 - 1000 s, austenite decomposition through an isothermal bainite transformation occurs rapidly for steels with aluminum contents of 0.91 - 1.73 wt-%. According to their studies, increasing the aluminum content accelerates the kinetics of the bainitic transformation.

Santofimia et al. [20] studied the Q&P heat treatment response of a 0.2C-2.5Mn-1.5Ni-1Cr-1.50Si wt-% steel alloy, specifically designed to retard or inhibit bainite, ferrite and pearlite formation as well as to prevent the precipitation of carbides during partitioning. The steels, however, underwent expansion during the partitioning stage. This expansion was most significant at a partitioning temperature of 350 °C and was attributed to bainite formation and growth, as bainite was identified in optical micrographs. No bainite could be identified at partitioning temperatures of 400 and 450 °C, at which the expansion was more limited and attributed to the isothermal growth of martensite. Despite apparent bainite formation, the retained austenite contents at room temperature reached a maximum at a partitioning temperature of 350 °C.

### 2.5.4 Grain and phase boundary migration

The immobility of grain and phase boundaries during partitioning is a key assumption of the CPE condition. Zhong et al. [9] observed interphase boundary growth of existing martensite into austenite. They found that for a Fe-0.2C-1.5Si-1.67Mn steel, a partitioning time of 80 s at 480 °C caused a notable change in the martensitic microstructure when compared to a holding time of 6 s. During 80 seconds of partitioning, the martensite grains lost their rigidly defined plate/block morphology as the grain boundaries became curved with a longer partitioning time. In TEM studies, these vaguely shaped ferritic grains were confirmed to have a similar orientation relationship with adjacent retained austenite as the morphologically sound martensitic laths partitioned for a shorter time, providing strong evidence of martensitic interfacial growth during partitioning.

Santofimia et al. [42, 64] calculated a semicoherent austenite/martensite interface to be bidirectionally mobile, the direction of interface migration depending on the austenite film thickness. De Knijf et al. [65] measured the change in the width of a retained austenite film in a hot stage TEM during partitioning at 400 °C. The material was a 1C-3Mn-1.5Si wt-% steel consisting of a mixed martensitic/austenitic microstructure prior to partitioning. The retained austenite film width increased from 96 nm to a maximum of approximately 112 after 20 minutes of partitioning. The phase boundary migration did not affect the Mn content of the phases, leading to the presence of a Mn gradient in the austenite grain after partitioning.

High-manganese steels with silicon additions have been studied by Santofimia et al. [7] and de Moor et al. [47]. In the studies by de Moor et al. [47], a high combination of ductility (15-17 %) and strength (1350 - 1500 MPa) was obtained for 0.2/0.3C-3Mn-1.6Si alloys after full austenitization, quenching to 200 °C and partitioning at 400 °C for 10-30 s. Intercritical annealing of these alloys at temperatures of appr. 700 °C resulted in low retained austenite contents and the presence of cementite in the final microstructure, suggesting that the annealing temperature was insufficient to dissolve carbides. A similar alloy studied by Santofimia et al. [7] (0.2C-3.5Mn-1.5Si) was annealed at 770 °C, quenched to 240 °C and partitioned at 350 °C for 3-5000 s. No cementite was detected in the final microstructures. The retained austenite fraction peaked at 0.18 at a partitioning time of 100 s. At partitioning times of 1000 s and 5000 s, the lath martensitic microstructure had largely disappeared, being replaced by a ferritic structure resembling upper bainite in morphology. This new phase did not, however, lower the observed carbon level in the austenite nor lessen the re-

tained austenite fraction in a significant manner, which would have been the case if upper bainite had formed. It was suggested that the new phase may be the result of the interfacial growth of martensite into austenite. A steel with the composition 0.2C-3.5Mn-0.45Si-0.22Al was subjected to a similar Q&P treatment: at all partitioning times, the fraction of retained austenite in the final microstructure was lower than that of the higher-silicon alloy. In addition, lower bainite with fine carbon precipitates was observed at all partitioning times, leading to the conclusion that a combination of small amounts of silicon and aluminum does not prevent carbide precipitation as effectively as a higher amount of silicon.

## 2.6 Intercritical annealing

Intercritical annealing of steels occurs at temperatures where two distinct phases, austenite and ferrite, are simultaneously at an equilibrium. The range of temperatures applicable for this type of annealing is largely governed by the steel alloy composition. As the volume fraction of phases in the microstructure changes, the chemical potentials of the various constituents are no longer at an equilibrium. This inequilibrium acts as a driving force for the diffusive migration of alloying atoms across the phase boundaries, meaning that if an alloy is given sufficient time to achieve a thermodynamic equilibrium at a given intercritical temperature, the chemical composition of the phases will be different. The situation is essentially similar to the CPE condition described in Chapter 2.3, with the difference that constraints related to the phase fractions and the atomic mobility are relaxed.

Quenching from an intercritically annealed state introduces several complexities into the prediction of the optimal Q&P temperature. During annealing, the diffusion of alloying elements between phases has to be taken into account, which in turn affects both the $M_s$ temperature as well as the kinetics of the martensitic phase transformation [39].

For binary alloys, the chemical composition of the phases at equilibrium can be readily obtained from phase diagrams by using the lever rule. In the case of multicomponent alloys, it is a common practice to use a suitable thermodynamic database, such as TCFE7 Steels/Fe-alloys database version 7 [66] incorporated in the Thermo-Calc® software [67]. A phase fraction-temperature diagram can be constructed to predict the phase fractions and compositions for a desired range of intercritical annealing temperatures.

From a Q&P perspective, varying the intercritical annealing temperature opens up some interesting heat treatment design possibilities. By selecting the annealing temperature to produce a smaller fraction of intercritical austenite, the alloying composition changes correspondingly and most notably the carbon content of the austenitic phase increases. Thus by carefully selecting the intercritical annealing temperature, the $M_s$ temperature of the selected alloy can be modified and thus the optimal quench temperature can be controlled (e.g. set to room temperature), which may be desirable from a production point of view.

Aluminum is an alloying element that, based on calculations with JMATPRO® [68], raises $Ac_1$ and $Ac_3$ temperatures significantly, to temperatures that enable fast recrystallization and diffusion of alloying elements between phases during intercritical annealing. An example calculation for a hypothetical intercritically annealed steel with the composition Fe-0.2C-

2Mn-2Al is shown in Figure 2.8. The phase fractions and compositions were calculated for the steel alloy using Thermo-Calc with the TCFE7 database for a temperature range of 700-900 °C with 10 °C intervals. For each annealing temperature interval, the composition of the austenite phase was used to calculate the optimal quench temperature using the methodology described in Chapter 2.4. Bhadeshia's method was used to calculate the $M_s$ temperatures and Bohemen-Van Sietsma's kinetic equations (Eq. 2.5 and 2.6) were used to calculate the extent of the martensitic transformation with respect to temperature.

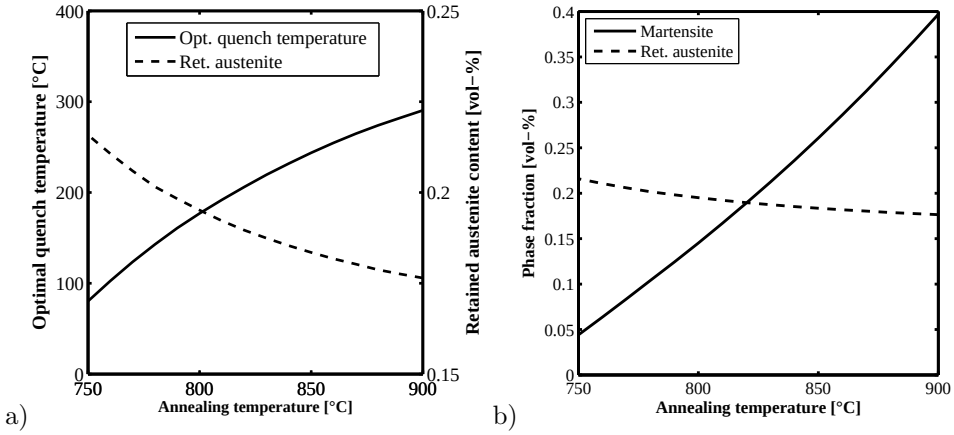


**Figure 2.8:** *Calculations with Speer's method for modeling the optimal Q&P quench temperature for various intercritical austenite fractions and chemical compositions (modeled with JMATPRO® [68]): a) Calculated optimal quench temperature and maximum retained austenite content with respect to annealing temperature. (b) Calculated maximum retained austenite content and corresponding martensite content with respect to annealing temperature.*

Figure 2.8 shows that as the intercritical annealing temperature drops, the optimal quench temperature decreases while the maximum obtainable retained austenite content increases. This is explained by the diffusion of manganese to the intercritical austenite during annealing. According to JMATPRO® calculations, manganese stabilizes austenite [68] and thus increases the maximum obtainable retained austenite fraction at room temperature.

It is worth noting that the intercritical annealing temperature affects the balance of all phases in the final microstructure. For example, the martensite fraction of the final microstructure when the intercritical annealing temperature is 750 °C is only approximately 5 vol-%. Would the steel be quenched to 25 °C from the annealing temperature instead of the calculated optimal quench point, the austenite content would drop to approximately 11 vol-% and the martensite content rise to approximately 15 vol-%. The predicted fractions of martensite and retained austenite in the final microstructure are shown in Figure 2.8b.

## 2.7 Cooling from an intercritical annealing state

During intercritical annealing, the phase fractions and compositions move towards an equilibrium. When the cooling towards the optimal quench temperature begins, this equilibrium is disturbed. This results in a driving force for a phase transformation of the intercritical austenite to ferrite. Whether the transformation will be reconstructive, displacive or whether it occurs at all depends on the cooling rate and the kinetics of the phase transformations involved.

### 2.7.1 Reconstructive ferrite growth

Reconstructive phase transformation mechanisms involving the diffusive movement of atoms require both time and a suitably high temperature, and if the cooling is very fast, there may not be enough time to accommodate the transformation. Phase transformations employing this mechanism include allotriomorphic, isotriomorphic or massive ferritic growth and the formation of pearlite. The ferrite reaction may occur with or without the partitioning of substitutional alloying elements between the phases. If partitioning occurs, the growth of the ferritic phase is slow and is controlled by the diffusion of alloying elements across the phase boundaries. For substitutional alloying elements such as Si, Mo, Co, Al, Cr and Cu, the solute partitioning is very limited and does not inhibit ferritic growth. An extreme case of this is a state of paraequilibrium proposed by Hultgren [44] (and modified for the CPE condition), where the ferritic reaction is fast enough so that only carbon moves across the phase boundary.

Massive ferrite growth (shown schematically in Figure 2.9) has been observed to occur relatively rapidly at temperatures above 600 °C. Hamada et al. [69] observed the growth of massive ferrite at $\gamma/\alpha$ boundaries in a low-carbon Fe-2Mn alloy to be as fast as appr. 50 $\mu m/s$ when quenched from 1200 °C at 20 °C/s. Santofimia et al. [12, 19] have also observed the migration of $\gamma/\alpha$ grain boundaries from ferrite towards austenite and martensite even at cooling rates of 100 °C/s, coining the term "epitaxial ferrite" for this type of intercritical ferrite growth. Dilatometric curves suggested that the interfacial growth occurred approximately in the temperature range of 750 - 600 °C.

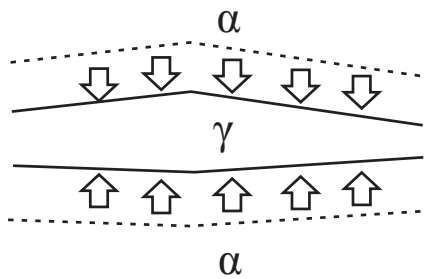


**Figure 2.9:** *Epitaxial growth of ferrite [12] or the formation of massive ferrite towards austenite during cooling*

The formation of pearlite during cooling is normally avoided in Q&P steels [7, 13] by alloy design. In general, as the concentration of alloying elements is increased, the formation of pearlite is precluded. Silicon is a particularly effective cementite formation suppressor, forming a kinetic barrier to the growth of cementite. As the solubility of silicon in cementite is very low, excess silicon must be rejected to the surrounding matrix prior to cementite growth [48]. The substitutional diffusion of silicon is slow, extending the time necessary for cementite formation. Other elements such as aluminum, copper and phosphorus that also have a very low solubility in the cementite phase can be used to retard its growth.

### 2.7.2 Displacive ferrite growth

Displacive transformations are very fast and involve coordinated movement of atoms across a moving interface [3, 22]. Due to the rate of transformation, the diffusion of substitutional alloying elements across the transformation interface is limited. This type of phase change also involves a shape deformation that must be accommodated by the surrounding matrix either elastically or plastically. The transformed phase usually assumes a thin plate shape to minimize strain.

Displacive transformations may occur at various temperatures. Widmanstätten ferrite can form at temperatures of around 700 °C as thin plates on the grain boundaries of intercritical or allotriomorphic ferrite that share a specific orientation relationship with the austenite phase [22]. Carbon has time to diffuse to the austenitic matrix during transformation, but the growth rate is not inhibited by carbon diffusion. This is due to the plate shape that allows much of the carbon to diffuse to the sides of the plate, while the tip encounters fresh austenite. Cheng et al. [70] observed the growth of Widmanstätten formations in a Fe-C-Mn steel during isothermal holding at a temperature range of approximately 550 to 800 °C. Acicular ferrite has a similar growth mechanism to Widmanstätten ferrite, but nucleates at intragranular inclusions.

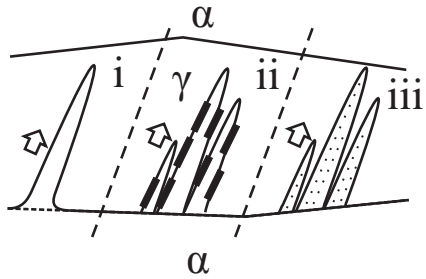


**Figure 2.10:** *A schematic showing the growth of secondary Widmanstätten ferrite (i), upper bainite (ii) or lower bainite (iii) during cooling. [22]*

Either upper or lower bainite (shown in Figure 2.10ii and iii) may also form during cooling if the formation of these phases has not been sufficiently retarded with suitable alloying. These mechanisms are shown schematically in Figure 2.10. Upper bainite (Figure 2.10ii) forms as platelike structures with lamellar cementite precipitated between the plates. In lower bainite, the laths tend to assume an acicular shape in micrographs (although in truth

they have a thin lenticular shape) with fine carbide precipitates inside the bainitic laths. If the steel has been alloyed with silicon or other element suppressing carbide formation, the cementite phase may be absent and instead retained austenite can be found in the intersheaf spaces [11]. The film-like austenite can be stabilized with carbon diffused from the supersaturated bainite.

### 2.7.3 Effect of intercritical annealing on Q&P processing

While the aforementioned mechanisms do not strictly violate the constrained paraequilibrium condition, they will complicate the prediction of the initial quench point. One factor to consider is that as the phase fractions change during cooling, the chemical potential of carbon in the phases will also be altered. Similarly to partitioning, this imbalance in chemical potential will act as a driving force for the diffusion of carbon from the ferritic to the austenitic phase, stabilizing it towards room temperature. This behavior is not limited to carbon. An electron probe microanalysis (EPMA) study revealed epitaxial ferrite growth when quenching a 0.19C-1.6Mn-0.35Si-1.1Al-0.09P steel to RT from 900 °C at 50 °C/s [20]. The finding was based on line profile elemental analysis, in which a gradient in alloying element contents was found at the edges of ferrite grains next to martensitic islands. This was interpreted as an incomplete segregation of alloying elements between phases, necessitated by the epitaxial growth of ferrite. Santofimia et al. [12, 71] have attempted to model epitaxial ferrite growth after quenching from an intercritically annealed state. In the model, the driving force behind interface mobility is the difference between the equilibrium carbon content in both phases: if the austenite phase is enriched relative to equilibrium, interface motion from austenite to martensite is preferred, and vice versa. The model predicts interface motion from austenite to martensite during initial partitioning, as the carbon content of austenite is higher than equilibrium close to the interface; however, the interface motion is reversed when the carbon content in the austenite evens out due to diffusion. In the calculations, the interface movement at equilibrium was approximately 0.05 $\mu$m towards austenite.

From the viewpoint of Q&P process design, it is of course necessary to be able to predict the amount of both the increase in the ferrite phase fraction during cooling and the final balance of carbon between the phases prior to the onset of martensitic transformation. In addition, the segregation of additional alloying elements (particularly silicon and aluminum) caused by epitaxial ferrite growth will also affect the behavior of the steel during partitioning.

# 3 Martensite formation and related crystallography

The desirable mechanical properties of Q&P steels are related to their unique microstructure. The unfinished martensitic transformation of the parent austenite results in a very fine microstructure of martensitic laths and retained austenite. In addition, the austenite has been stabilized with carbon diffused from the neighboring martensite. As the properties of martensite are intrinsically linked to the crystallography of the phase transformation, crystallographic methods are required to properly characterize Q&P materials. The crystallography of the martensitic transformation is discussed in this Chapter. Crystallographic methods for Q&P material characterization are also presented and discussed.

## 3.1 Martensite crystallography

Martensite is formed via the co-ordinated movement of atoms across a moving interface, leading to a rigidly defined orientation relationship between the parent austenite and martensite orientations. The orientation relationship between the parent austenite and martensitic lattices can usually be summarized as the parallelism or near-parallelism of certain close-packed planes and directions.

The Bain correspondence proposed by Bain [72] in 1924 is an early attempt to explain the orientation relationships found between martensite and austenite, as well as the observed volume change during martensitic transformations in steel. The crystal structure of austenite consists of a face-centered cubic (fcc) lattice (Figure 3.1a). Between two adjacent fcc cells, a body-centered tetragonal unit cell can be drawn, as shown in Figure 3.1b.

When the austenitic lattice is subjected to a suitable strain, the body-centered tetragonal austenite lattice is transformed to body-centered cubic martensite, as illustrated in Figure 3.1c and 3.1d. This type of homogenous deformation in the lattice is called Bain strain [3] and it explains the volume change (approximately 3 vol-%) observed during a martensitic transformation. It also results in the exact parallelism of the (111) planes of austenite and the (011) planes of martensite.

In practice, however, only near-parallelism between close-packed planes and directions is observed. According to the phenomenological theory of martensite crystallography developed by Kelly [73] in 1953, this is because of the nature of the martensitic transformation rather than any deficiency in the measurement accuracy. According to the theory, the martensitic transformation is caused by a rapidly moving, semicoherent interface between the austenitic and martensitic lattices [3]. To preserve interfacial coherency, it is necessary that the interface must contain an invariant line, which is unaffected in direction and magnitude by the transformation. This requirement can only be met if the Bain strain is combined with a suitable rigid-body rotation to bring an invariant line to the interface. Combining these two operations results in the orientation relationships (ORs) observed in crystallographic analy-

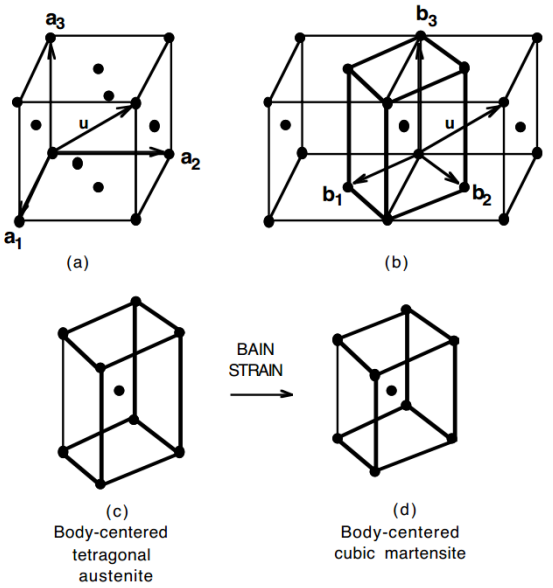


**Figure 3.1:** *a) A face-centered cubic cell of austenite, b) two adjacent fcc austenite cells with a body-centered tetragonal austenite cell drawn between them, c) a body-centered tetragonal austenite cell undergoing deformation into d) a body-centered cubic martensite cell. [3]*

ses. Table 3.1 gives the near-parallel close-packed planes and directions of some theoretical and observed orientation relationships.

**Table 3.1:** *Some well-known ORs between austenite and martensite.*

| | |
|---|---|
| $\{111\}\gamma \| \{011\}\alpha$ | Kurdjumov-Sachs |
| $\langle 10\bar{1}\rangle\gamma \| \langle 11\bar{1}\rangle\alpha$ | |
| $\{111\}\gamma \| \{011\}\alpha$ | Nishiyama-Wasserman |
| $\langle 10\bar{1}\rangle\gamma$ *appr. 5.3 ° from* $\langle 11\bar{1}\rangle\alpha$ *towards* $\langle \bar{1}1\bar{1}\rangle\alpha$ | |
| $\{111\}\gamma$ *appr. 0.2 ° from* $\{011\}\alpha$ | Greninger-Troiano |
| $\langle 10\bar{1}\rangle\gamma$ *appr. 2.7 ° from* $\langle 11\bar{1}\rangle\alpha$ *towards* $\langle \bar{1}1\bar{1}\rangle\alpha$ | |

It should be noted that the Kurdjumov-Sachs and Nishiyama-Wasserman orientation relationships assume parallel planes between the $\gamma$ and $\alpha$ phases and therefore cannot have an invariant line at the interface. True ORs differ from these by a small degree. It is also worth mentioning that the rotation described by OR does not incorporate the shape deformation needed to change the lattice size.

A crystal with cubic symmetry has 24 equivalent crystallographic solutions; in other words, an orientation can be expressed in 24 mutually equivalent ways with respect to specimen symmetry. However, the rotation to bring an orientation from the austenitic coordinate system to the martensitic one produces different orientations with respect to specimen sym-

metry when the rotation is performed on different crystallographic solutions in the parent lattice. This produces 24 different possible variant orientations for the martensite originating from a parent austenite orientation. These can be generated from the OR using symmetry operations for cubic crystals. In the case of orientation relationships such as Nishiyama-Wasserman, a lesser amount of variants are generated because of the multiple occupations of some orientations. For N-W OR specifically, only 12 variants of separate orientation can be found.

Morito et al. [5] have classified the 24 variants generated by the Kurdjumov-Sachs orientation relationship into groups of four packets. In a packet, all variants share the parallelism of the same close-packed planes. Each packet contains six variants (e.g. V1 to V6) with parallel direction relationships on the close-packed parallel planes. All 24 variants are shown in Table 3.2 along with the axes and angles of misorientation of a given variant from V1.

Although the exact parallelism of planes and directions of the K-S OR cannot be observed in actual crystallographic measurements of martensite, the consistent variant labeling system by Morito et al. [5] has been used to successfully characterize a number of martensitic microstructures with varying orientation relationships between austenite and martensite [4,74].

The martensitic transformation is constrained by parent austenite grain boundaries. The interface between the forming martensite and the parent austenite is referred to as the habit plane. The constraints of the surrounding matrix impose a thin lenticular lath-like shape on the forming martensite, making the habit plane curved on a macroscopic level. The average plane of the lath is very nearly parallel to the habit plane. For low-alloy steels, the habit plane indices are approximately {111} as related to the austenite lattice. The morphology and the macroscopic orientation of the martensitic laths are therefore largely predetermined. The same types of constraints on morphology and macroscopic orientation apply also to other phases resulting from a shear-assisted transformation. For example, in Widmanstätten structures (shown in Figure 2.10a) the long axis of the formed grains is very nearly parallel to the habit plane.

## 3.2 Accommodation and variant selection

The orientations of martensitic laths are rigidly constrained to a set of 24 variants. The mechanism by which particular variants are favored over the others has been a subject of intense study in recent years [4, 74–78]. This type of selection is often linked to the shape deformation inherent to the martensitic transformation, which may or may not comply with an external stress [79], such as that imposed for example by a previously formed martensitic variant. Based on their analysis of reconstructed parent austenite EBSD orientation maps, Miyamoto et al. [76] proposed a variant selection model in which variants with habit planes parallel to the slip planes activated by strain were preferentially formed. Essentially, dense dislocation walls formed on the slip planes are replaced by an austenite/martensite interface, reducing the free energy change necessary for the nucleation of martensite and thus promoting the selection of variants with a habit plane parallel to the activated slip plane.

Within a packet, self-accommodation typically occurs: that is, the formation of a specific variant next to an already formed one is favored if this results in a smaller value of trans-

**Table 3.2:** *24 variants in martensite as defined by the Kurdyumov-Sachs orientation relationship. [5]*

| **Variant** | **Plane parallel** | **Direction parallel** | **Rotation from Variant 1** | |
|---|---|---|---|---|
| **No.** | | $[\gamma]\|\|[\alpha']$ | **Axis (indexed by martensite)** | **Angle [deg.])** |
| V1 | | $[\bar{1}01]\|\|[\bar{1}\bar{1}1]$ | - | - |
| V2 | | $[\bar{1}01]\|\|[\bar{1}1\bar{1}]$ | [0.5774 -0.5774 0.5774] | 60 |
| V3 | $(111)\gamma$ | $[01\bar{1}]\|\|[\bar{1}\bar{1}1]$ | [0.0000 -0.7071 -0.7071] | 60 |
| V4 | $\|\|(011)\alpha'$ | $[01\bar{1}]\|\|[\bar{1}1\bar{1}]$ | [0.0000 0.7071 0.7071] | 10.53 |
| V5 | | $[1\bar{1}0]\|\|[\bar{1}\bar{1}1]$ | [0.0000 0.7071 0.7071] | 60 |
| V6 | | $[1\bar{1}0]\|\|[\bar{1}1\bar{1}]$ | [0.0000 -0.7071 -0.7071] | 49.47 |
| V7 | | $[10\bar{1}]\|\|[\bar{1}\bar{1}1]$ | [-0.5774 -0.5774 0.5774] | 49.47 |
| V8 | | $[10\bar{1}]\|\|[\bar{1}1\bar{1}]$ | [0.5774 -0.5774 0.5774] | 10.53 |
| V9 | $(1\bar{1}1)\gamma$ | $[\bar{1}\bar{1}0]\|\|[\bar{1}\bar{1}1]$ | [-0.1862 0.7666 0.6145] | 50.51 |
| V10 | $\|\|(011)\alpha'$ | $[\bar{1}\bar{1}0]\|\|[\bar{1}1\bar{1}]$ | [-0.4904 -0.4625 0.7387] | 50.51 |
| V11 | | $[011]\|\|[\bar{1}\bar{1}1]$ | [0.3543 -0.9329 -0.0650] | 14.88 |
| V12 | | $[011]\|\|[\bar{1}1\bar{1}]$ | [0.3568 -0.7136 0.6029] | 57.21 |
| V13 | | $[0\bar{1}1]\|\|[\bar{1}\bar{1}1]$ | [0.9329 0.3543 0.0650] | 14.88 |
| V14 | | $[0\bar{1}1]\|\|[\bar{1}1\bar{1}]$ | [-0.7387 0.4625 -0.4904] | 50.51 |
| V15 | $(\bar{1}11)\gamma$ | $[\bar{1}0\bar{1}]\|\|[\bar{1}\bar{1}1]$ | [-0.2461 -0.6278 -0.7384] | 57.21 |
| V16 | $\|\|(011)\alpha'$ | $[\bar{1}0\bar{1}]\|\|[\bar{1}1\bar{1}]$ | [0.6589 0.6589 0.3628] | 20.61 |
| V17 | | $[110]\|\|[\bar{1}\bar{1}1]$ | [-0.6589 0.3628 -0.6589] | 51.73 |
| V18 | | $[110]\|\|[\bar{1}1\bar{1}]$ | [-0.3022 -0.6255 -0.7193] | 47.11 |
| V19 | | $[\bar{1}10]\|\|[\bar{1}\bar{1}1]$ | [-0.6145 0.1862 -0.7666] | 50.51 |
| V20 | | $[\bar{1}10]\|\|[\bar{1}1\bar{1}]$ | [-0.3568 -0.6029 -0.7136] | 57.21 |
| V21 | $(11\bar{1})\gamma$ | $[0\bar{1}\bar{1}]\|\|[\bar{1}\bar{1}1]$ | [0.9551 0.0000 -0.2962] | 20.61 |
| V22 | $\|\|(011)\alpha'$ | $[0\bar{1}\bar{1}]\|\|[\bar{1}1\bar{1}]$ | [-0.7193 0.3022 -0.6255] | 47.11 |
| V23 | | $[101]\|\|[\bar{1}\bar{1}1]$ | [-0.7384 -0.2461 0.6278] | 57.21 |
| V24 | | $[101]\|\|[\bar{1}1\bar{1}]$ | [0.9121 0.4100 0.0000] | 21.06 |

formation strain. Takaki et al. [80] found a type of variant selection to occur in nanosized retained austenite: when the size of a parent austenite grain was below 1 $\mu$m, martensitic variants forming in an austenite grain were typically restricted to those in a single packet.

## 3.3 Parent austenite reconstruction

The orientation relationship between a martensitic lath and the parent austenite grain is expressed in Equation 3.1.

$$O_\gamma \cdot C_i \cdot T_{\gamma\to\alpha} = O_{\alpha,i} \tag{3.1}$$

where $O_{\alpha,i}$ and $O_\gamma$ denote the martensitic and austenitic crystallographic orientations in 3x3 orientation matrix notation, respectively. $T_{\gamma\to\alpha}$ denotes the orientation relationship or the rotation used to bring the austenitic orientation to the martensitic one and $C_m$ stands for one of the 24 crystal symmetry operators for cubic crystals. The parent austenitic orientation can be obtained using this equation, if the correct symmetry operator and the orientation relationship are known.

However, as a martensitic lath is always one of the 24 variants produced from a single parent austenite orientation, it is impossible to deduce the orientation of the parent austenite grain from a single martensitic orientation measurement. It is therefore necessary to obtain crystallographic measurements from multiple variants produced from the same parent austenitic grain. Assuming a defined orientation relationship (such as Greninger-Troiano in Table 3.1), all potential parent austenite orientations are calculated for all of the measured orientations, resulting in several sets of 24 variant orientations. Since all the martensitic laths share the same parent austenite grain, a mutual orientation can be found that will appear in all of these sets. This orientation can be assumed as the parent austenite grain orientation.

The process of finding the parent austenite orientation is clarified in Figure 3.2. Figure 3.2a shows an IPF TD orientation map overlaid on an EBSD band contrast image of martensite. The IPF TD orientations shown all originate from a single parent austenite grain. The orientations are shown in a (100) pole figure in 3.2c. Figure 3.2d shows a (100) pole figure of an orientation distribution function (ODF) of all possible parent austenite orientations calculated with Equation 3.1. The ODF pole figure shows a clear intensity peak for a specific orientation. The peak orientation is that of the parent austenite grain. Plotting the parent austenite orientation in Figure 3b places it neatly at the centers of the three truncated square shapes, suggesting a convenient visual method for determining parent austenite orientations from a (100) pole figure.

It should be stressed that when reconstructing parent austenite orientations, the orientation relationship should initially be determined experimentally. The use of theoretical orientation relationships such as K-S results in lower accuracy and erroneous twin parent orientations. The tendency for twin misindexation when using assumed ORs is explained by the exact close-packed plane parallelism in the K-S and N-W orientation relationships. A single packet of martensite will contain only variants sharing the same parallel relations between close packed planes (such as variants V1-V6, all sharing the $(111)\gamma$ // $(011)\alpha'$ parallelism). For these variants, there are in fact two austenite orientations with a twin relationship to one another that can satisfy the condition of the parallel relations of close-packed planes. The parent austenite orientation cannot therefore be calculated explicitly using orientations of a single packet and an OR that assumes total parallelism of close-packed planes. Conversely, Miyamoto et al. [75] have shown that the parent austenite orientation can be calculated using only two variants when sufficiently accurate measurements and an experimentally determined OR are used.

It should be clear by now that when the goal is the total reconstruction of the parent austenite orientation map from a martensitic orientation map, some method of dividing the

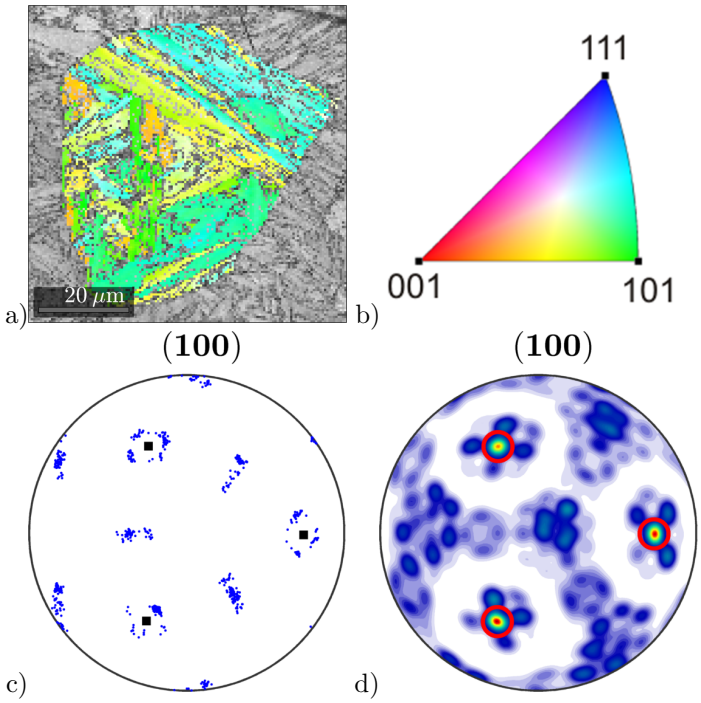


**Figure 3.2:** *(a) IPF TD orientation map of martensite originating from a single parent austenite grain overlaid on a band contrast EBSD image. (b) The color scheme of the IPF image. (c) The orientation pixel measurements originating from the parent austenite grain in a) shown in a (100) pole figure. Parent austenite orientation annotated with dark squares. d) A (100) pole figure of the ODF of all potential parent austenite orientations. Peak orientation emphasized with circles (red).*

individual orientation measurements into clusters is required, with each cluster containing only orientations belonging to a single parent austenite grain. Several approaches have been made in recent years [76,81]. A novel approach by Gomes and Kestens [82] treated the grain map constructed from martensitic EBSD data as a geometric graph cluster, with each grain in the map becoming an individual node in the graph. The intergranular grain boundary misorientations were then evaluated and given a value based on the likelihood of representing a misorientation between two martensite blocks originating from the same parent austenite grain. The resulting graph cluster was then dissected into smaller clusters corresponding to parent austenite grains using Markov Cluster Analysis (hereafter referred to as MCL) developed by van Dongen [83].

The MCL process utilizes random walks for the retrieval of cluster structure in graphs [83]. The graph consists of nodes connected by edges, with many edges inside clusters of nodes and only few edges between clusters. In this context, a random walk is considered as a journey starting from a random node, from which a walker departs and chooses as destination another node by chance. The likelihood of choosing a new node is determined by the strength of the edge connecting the destination node and the current node. At each

node, the random choice is made again. The probability to reach another cluster by this method is low, because of the few edges connecting nodes between clusters and the many edges connecting nodes within clusters.

In the MCL process, many random walks are simulated. The result can be considered a flow of random traffic, which is manipulated so that flow between clusters is diminished and flow within clusters is encouraged. Eventually, the flow between clusters evaporates and the result is a set of discrete clusters. In practice, a stochastic matrix is constructed from the graph and subjected to an alternating set of two algebraic operations, expansion and inflation, until a set of discrete clusters is achieved. The method as it is used in this work is described in more detail in Section 4.4.

# 4 Experimental methods

In the experimental part of this study, the response of several intercritically annealed high-aluminum steels to Q&P processing was characterized. The details of materials manufacture and initial heat treatment design are described in Section 4.1.

As the ability to predict the microstructure of the steel at the initial quenching temperature is critically important to achieve a Q&P microstructure, particular attention was paid to the behavior of the steel when quenched from both fully austenitized and intercritically annealed states. The phase transformation kinetics during cooling were studied with dilatometry, and a microstructural analysis on the quenched specimens was conducted using a variety of methods described in Section 4.2. The characterization of the quenched microstructures necessitated the use of electron microscopy and electron backscatter diffraction (EBSD) analysis. The study of some of the observed microstructural features was only possible through the reconstruction of the parent austenite microstructure from martensitic EBSD data with the methodology described in 4.4. To this end, the orientation relationships between the martensitic and austenitic phases were first determined using the methodology described in Section 4.3.

After determining suitable quench temperatures, the specimens were partitioned to allow carbon diffusion from martensite into austenite. The microstructure of the partitioned steels was analysed, the level of carbon in retained austenite and the amount of carbides were studied using scanning and transmission electron microscopy, XRD measurements and Mössbauer spectroscopy.

## 4.1 Test materials and heat treatment design

### 4.1.1 Specimen manufacture

Table 4.1 shows the chemical compositions of the two experimental steels, both of them containing significant amounts of aluminum. Steel B contains additions of copper and nickel in an attempt to partially balance the tendency of aluminum to stabilize ferrite and consequently increase the austenitization temperatures. In addition, increase in copper content has been observed to increase retained austenite contents after austempering in ADI [84]. Steel A has some silicon in addition to aluminum to provide additional resistance to the formation of carbides during partitioning and phosphorus to increase the stability of retained austenite [85]. Chromium additions have also been observed to have some capability for retarding carbide precipitation and bainite formation at partitioning temperatures [20]. Niobium has the effects of grain refinement and precipitation hardening [58] and has also been observed to retard the isothermal bainite transformation [86, 87].

The samples were vacuum-cast as 40x40x180 mm billets (approx. 2 kg in weight) into a water-cooled copper die in a low pressure casting furnace at Swerea KIMAB Research Cen-

**Table 4.1:** *Chemical compositions of the investigated steels.*

| Element [wt-%] | C | Mn | Si | Al | P | Ni | Cu | Nb | Cr |
|---|---|---|---|---|---|---|---|---|---|
| Steel A | 0.19 | 1.99 | 0.38 | 1.96 | 0.05 | 0.02 | 0.02 | 0.03 | 0.11 |
| Steel B | 0.22 | 2.03 | 0.04 | 2.93 | 0.01 | 0.48 | 0.96 | 0.03 | 0.12 |

tre, Stockholm. The cast specimens were soaked at 1200 °C for 30 minutes prior to hot and cold rolling into sheets using a laboratory rolling mill at the University of Oulu. The samples were first hot rolled into 3 mm sheets with the finish rolling temperature (FRT) well above the recrystallization limit temperature, then quenched to 600 °C, followed by slow cooling by wrapping the hot rolled samples into an insulator blanket. The specimens were subsequently cold rolled into 60 mm wide and 1.3 mm thick sheets.

### 4.1.2 Heat treatment design

Calculations were made using JMATPRO® [68] to predict the $A_1$ and $A_3$ temperatures for the steels, as well as the ferrite/austenite ratios and the balances of alloying elements between the phases in between these temperatures. Figure 4.1 shows the aluminum, manganese and carbon contents of the austenite phase at the intercritical temperatures, as well as the fraction of austenite.

The method proposed by Speer et al. [14] was used to determine parameters for a preliminary quenching and partitioning treatment. The $M_s$ temperatures were calculated with Bhadeshia's method for the 900 °C intercritical state using the austenite compositions in Table 4.2. Equation 2.5 was used to predict the athermal progression of martensitic transformation, with the $K$ parameter calculated using Equation 2.6 by van Bohemen and Sietsma [39]. Based on the calculations, quenching temperatures ($T_Q$) of 270 °C and 280 °C were selected for Steels A and B, respectively. The final retained austenite content was predicted to be 15 vol-% with a carbon content of 1.23 wt-% for Steel A and 16 vol-% with a carbon content of 1.203 wt-% for Steel B. The heat treatment cycle is shown schematically in Figure 4.2.

More accurate parameters for the Q&P heat treatments were left to be determined after the dilatometry experiments. These are covered in detail in Section 5.4.

In addition, $M_s$ temperatures were calculated for the steels for a range of temperatures, beginning from $A_1$ and ending at $A_3$. The method used for $M_s$ calculation was that proposed by Bhadeshia, as outlined in Appendix 1. For temperatures between $A_1$ and $A_3$, the $M_s$ temperature was calculated for the austenite phase using the compositions given by JMATPRO® [68]. The results are shown in Figure 4.1.

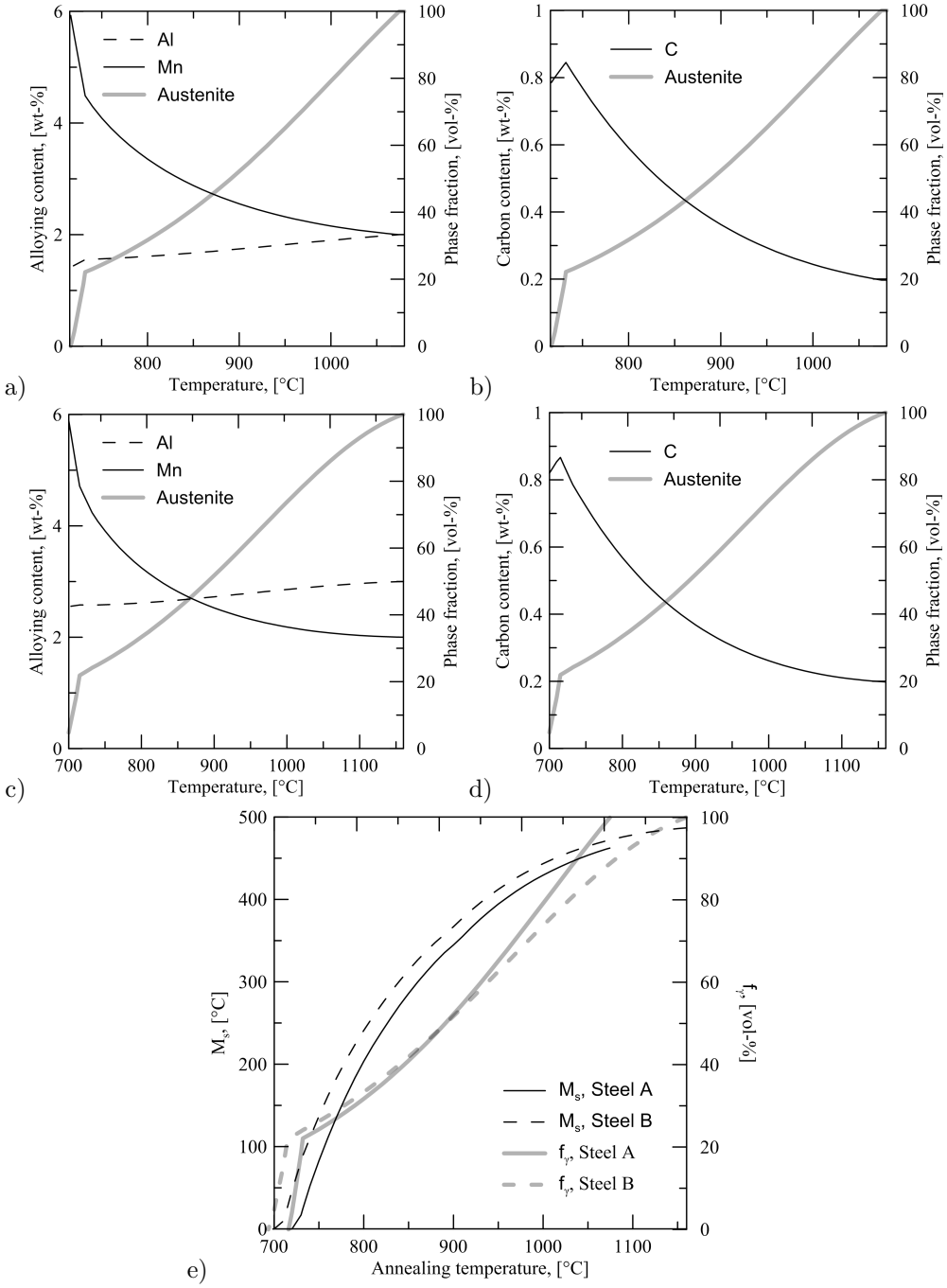


**Figure 4.1:** *Alloy contents in austenite of selected components along with austenite fraction with respect to temperature: a) and b) Steel A, c) and d) Steel B. e) $M_s$ and $f_\gamma$ with respect to temperature.*

### 4.1.3 Preliminary heat treatments and dilatometry

The preliminary Q&P heat treatments were conducted on a Gleeble 3800 thermomechanical simulator at the University of Oulu. 10x60 mm strips were cut from the laboratory rolled sheet sample for simulation experiments. The cutting direction was transverse to the rolling direction. In Gleeble, the specimens were subject to computer-controlled, programmed resistance heating, followed by controlled cooling with high pressure argon gas jet. The temperature of the sample was monitored with a K-type thermocouple.

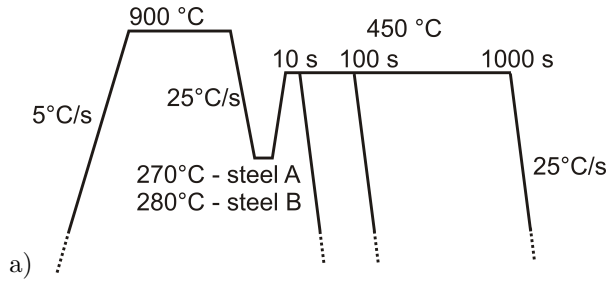


**Figure 4.2:** *Heat treatment cycle for the preliminary Q&P tests.*

The specimens were heated to 900 °C at a rate of 5 °C/$s$, held for 3 minutes and quenched to the initial quench temperature $T_Q$ at a rate of 25 °C/$s$, held there for 10s and heated to a partitioning temperature $T_P$ of 450 °C at a rate of 100 °C/$s$. The holding times at $T_P$ were 10, 100 and 1000 s to observe the effects of holding on the retained austenite content and phase morphology. The specimens were then quenched to room temperature at a cooling rate of 25 °C/$s$.

Dilatometry experiments were conducted to study the applicability of the $M_s$ calculation method and the progression of the martensite transformation with respect to temperature. The experiments consisted of annealing the specimens at fully austenitized and intercritical temperatures, followed by quenching to room temperature at various cooling rates. The specimens were heated to a temperature of 1200 °C at a rate of 5 °C/s, held for 2 minutes and cooled to room temperature at rates of 10,30 and 50 °C/s. The annealing temperature of 1200 °C was chosen based on thermodynamic calculations with the JMATPRO® software and database [68] to obtain a fully austenitized microstructure prior to the cooling step. The thermal dilatation of the specimen was measured with an extensometer fitted with silica rods.

Further dilatometric experiments were carried out at the Colorado School of Mines with the TA Instruments model TA805L dilatometer. Four intercritical annealing temperatures were selected for dilatometry studies: 750, 800, 850 and 900 °C. 5x10mm strips were cut from the sheets and induction heated in a low vacuum to the annealing temperature. After holding, the specimens were quenched with an argon gas jet at a rate of 25 °C/s to room temperature. Dilatation was measured with an extensometer fitted with silica rods. The expected austenite fractions and phase compositions at the studied intercritical annealing temperatures are shown in Table 4.2. The holding time was varied between 3, 10 and 60 minutes for the annealing temperatures of 750, 800, and 850 °C. At a temperature of 900

°C, only the holding time of 3 minutes was studied.

The transformation curves were extracted from the dilatometric data by line fitting over the linear thermal contraction portion of both the austenite and martensite phases, as indicated in Figure 4.3a. Martensite and austenite cooling contraction curves were extrapolated from the linear portions of the curve. The extent of the martensitic transformation was calculated by using the lever rule. A curve corresponding to Equation 2.5 was then fitted to this data. The fitting was done using Trust-Region-Reflective Least Squares Algorithm in the Matlab® Curve Fitting Toolbox. Parameters for $K$ and $M_s$ were then obtained for Equation 2.5 from the fitting result. The transformation data up to 0.2 martensite fraction were excluded from the fitting to reduce the effect of the initial gradual martensite start on the fit. Figure 4.3 shows a single martensite transformation curve along with a visualization of the data exclusion. Cooling contraction coefficients for austenite and martensite could also be obtained from the data.

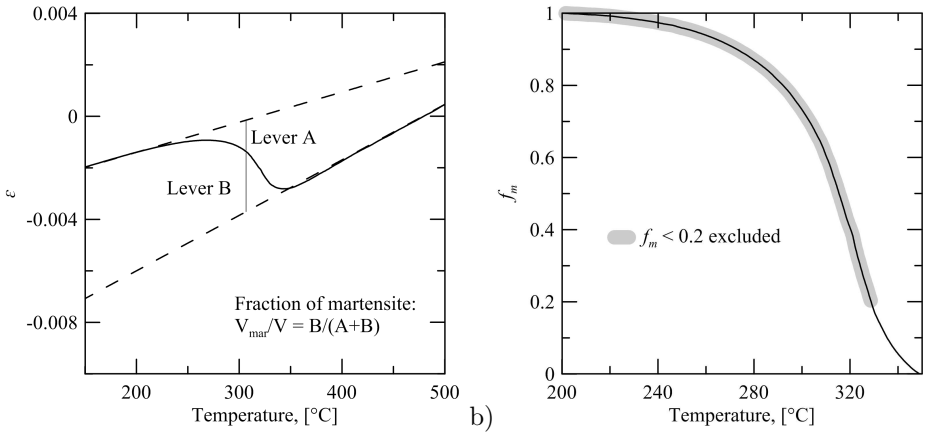


**Figure 4.3:** *a) The cooling contraction curve around the martensitic transformation, b) the martensite volume fraction with respect to temperature extrapolated from the data shown in a).*

## 4.2 Characterization

The aim of materials characterization was to study the success of the quenching and partitioning procedure with respect to the expected microstructure and mechanical properties. This included microstructural evaluation with optical and electron microscopy as well as crystallographic studies with X-ray diffraction and electron backscatter diffraction. Mechanical properties were evaluated using a standard hydraulic tensile frame.

Cross-sections were prepared from the middle of the heat treated specimens close to the thermocouple location, mounted in epoxy resin, and ground and polished with colloidal silica used in the final polishing step to obtain a deformation free surface for optical and electron microscopy studies. Some specimens were etched with a Klemm's I tint etchant

**Table 4.2:** *The calculated austenite fractions, $M_s$ temperatures and austenite phase contents (in wt-%) at indicated annealing temperatures.*

| Steel | $T_a$, [°C] | $f_\gamma$ | $M_s$, [°C] | C | Mn | Si | Al | P | Ni | Cu | Nb | Cr |
|---|---|---|---|---|---|---|---|---|---|---|---|---|
| A | 750 | 0.24 | 82.83 | 0.77 | 4.09 | 0.32 | 1.57 | 0.031 | - | - | 0.001 | 0.18 |
| | 800 | 0.31 | 203.5 | 0.59 | 3.35 | 0.33 | 1.61 | 0.027 | - | - | 0.003 | 0.15 |
| | 850 | 0.40 | 285.8 | 0.46 | 2.88 | 0.34 | 1.67 | 0.025 | - | - | 0.011 | 0.14 |
| | 900 | 0.52 | 344.6 | 0.36 | 2.55 | 0.34 | 1.74 | 0.023 | - | - | 0.030 | 0.12 |
| B | 750 | 0.26 | 136.9 | 0.72 | 3.91 | - | 2.58 | - | 0.87 | 1.27 | 0.001 | 0.18 |
| | 800 | 0.33 | 240.9 | 0.57 | 3.25 | - | 2.61 | - | 0.77 | 1.19 | 0.004 | 0.15 |
| | 850 | 0.42 | 314.1 | 0.45 | 2.82 | - | 2.66 | - | 0.70 | 1.13 | 0.011 | 0.14 |
| | 900 | 0.52 | 366.8 | 0.37 | 2.52 | - | 2.73 | - | 0.64 | 1.09 | 0.031 | 0.12 |

and examined in a Nikon DSA2 light optical microscope.

Prior to the cutting of cross-sections for the microstructural study, the retained austenite content of the Q&P specimens was measured at room temperature using X-ray diffraction. The XRD analyses were conducted with the Panalytical Empyrean X-Ray diffractometer using Cu K-radiation ($30° < 2\theta < 110°$, 40 kV, 45 mA). The peaks used in the analysis were (110), (200), (211) and (220) for martensite and (111), (200), (220) and (311) for austenite. The method for retained austenite calculation was the four-peak method described in SP-453 [88].

The crystallography of the martensitic transformation was studied with electron backscatter diffraction. The electron microscope was a Zeiss ULTRAPLUS UHR FEG-SEM system. The system was fitted with an HKL Premium-F Channel electron backscatter diffraction (EBSD) system with a Nordlys F400 detector, which was used for phase contrast and orientation mapping. The parameters for EBSD analysis were: 20 kV acceleration voltage, 15 mm working distance, tilt angle of 70 degrees with variable step size. Post processing of the data was conducted as outlined in Sections 4.3 and 4.4.

## 4.3 Determination of the orientation relationship between austenite and martensite

To study the crystallographic features of martensite such as variant selection and parent austenite texture, it is necessary to reconstruct the parent austenite grain structure as described in Chapter 3.1. Prior to reconstruction, it is necessary to obtain the orientation relationship between austenite and martensite.

The orientation relationship between austenite and martensite can be expressed in the following manner (repeating Equation 3.1 for convenience) :

$$O_\gamma \cdot C_i \cdot T_{\gamma\to\alpha} = O_{\alpha,i} \tag{4.1}$$

In Equation 4.1, $O_\gamma$ and $O_{\alpha,i}$ stand for the crystallographic orientations of austenite and martensite, $T_{\gamma\to\alpha}$ stands for the orientation relationship between the phases and $C_i$ is a symmetry operator for one of the 24 mutually equivalent crystallographic solutions present in cubic symmetry. Use of different symmetry operations results in a different $O_\alpha$ variant orientation for the same $O_\gamma$. Assuming that two different martensitic variants have been formed from the same austenitic parent grain, the misorientation $M$ between the two would be:

$$(O_{\alpha,i})^{-1} \cdot O_{\alpha,j} = M \tag{4.2}$$

or, replacing $O_{\alpha,i}$ with the orientation relationship in Equation 4.1:

$$(O_\gamma \cdot C_i \cdot T_{\gamma\to\alpha})^{-1} \cdot O_\gamma \cdot C_j \cdot T_{\gamma\to\alpha} = M \tag{4.3}$$

which can then be written as:

$$(C_i \cdot T_{\gamma\to\alpha})^{-1} \cdot C_j \cdot T_{\gamma\to\alpha} = M \tag{4.4}$$

The misorientation $M$ between two martensitic variants can be obtained experimentally by electron backscatter diffraction. The left side of the equation is equivalent to one of the 24 possible misorientations determined by cubic symmetry. By presuming some orientation relationship $T_{\gamma\to\alpha}$ between austenite and martensite, this list of theoretical misorientations can be generated using Equation 4.4. Any experimentally obtained misorientation can then be compared to the list to determine whether it can be classified as an intermartensitic misorientation. The Kurdjumov-Sachs orientation relationship is often used in this role [3]. The K-S OR predicts that the $(111)\gamma$ and $(011)\alpha'$ planes and the $[\bar{1}01]\gamma$ and $[\overline{11}1]\alpha'$ directions are exactly parallel. According to the phenomenological martensitic theory, this parallelism does not occur in real martensite [73]. It is therefore not expected to find an exact match and it is necessary to use some threshold value to classify the misorientations. The minimum angle of misorientation between the experimentally observed $M$ and the list of modeled misorientations can be used for this purpose. By taking the mean of all minimum misorientation angles, the fit of the assumed OR with the experimental data can be assessed.

By comparing a large set of various orientation relationships to the experimental data, an optimal orientation relationship of desired accuracy can be obtained. Although this method has been used to successfully obtain satisfactorily accurate orientation relationships [89], it can be somewhat time-consuming with large datasets if high accuracy is desired. Another approach is to determine the orientation relationship iteratively. Equation 4.4 can be written in the form:

$$T_{\gamma\to\alpha} = C_j^{-1} \cdot C_i \cdot T_{\gamma\to\alpha} \cdot M \tag{4.5}$$

The calculation of $T_{\gamma\to\alpha}$ in this manner is not possible, since the orientation relationship is found on both sides of the equation. If an assumed orientation relationship $T^{as}_{\gamma\to\alpha}$ is instead used on the right side of the equation, there will be a misorientation between the calculated $T_{\gamma\to\alpha}$ and the true orientation relationship. Assuming a sample of equal amounts of suitable pairs of symmetry operators, the average of the calculated orientation relationships will be

equal to the experimental orientation relationship.

The calculation is visualised in the spherical projection shown in Figure 4.4. A list of misorientations was generated with Equation 4.4 using the orientation relationship measured by Miyamoto et al. [75] as $T_{\gamma\to\alpha}$ and with symmetry operators $C_j = 1$ and $C_i = 1...24$. The Kurdjumov-Sachs orientation relationship was used as $T^{as}_{\gamma\to\alpha}$ to calculate $T_{\gamma\to\alpha}$ with Equation 4.5. Figure 4.4 shows the [100] austenite orientation, a corresponding martensitic [100] orientation as calculated with the OR by Miyamoto et al. [75] as well as the ones calculated with the OR obtained using Equation 4.5. The average of the calculated relationships yields the actual orientation relationship.

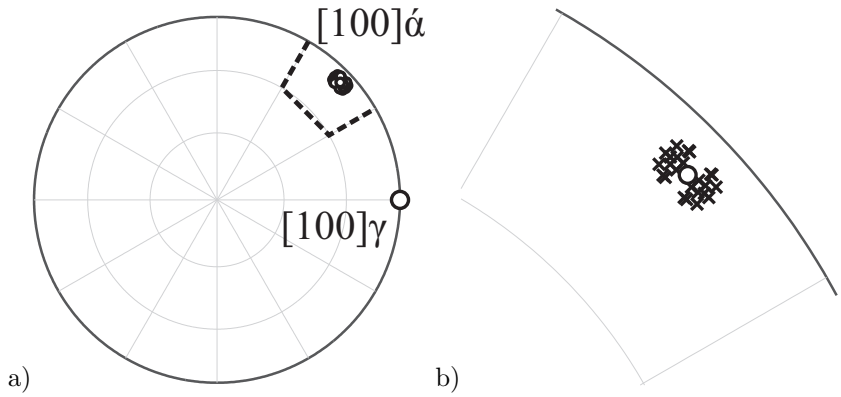


**Figure 4.4:** *a) Spherical projection showing the [100] directions of austenite and martensite calculated with the actual OR by Miyamoto et al. [75] and using Equation 4.5. b) Closeup of the area marked with dashed line in a) showing the martensitic [100] orientations calculated with the actual OR (circle) and with Equation 4.5 (crosses).*

The correct symmetry operators can be found using Equation 4.4 to determine the operators $C_i$ and $C_j$ that result in a minimum misorientation angle with the experimentally observed misorientation. It should be noted that a large difference in the assumed and experimental orientation relationship may result in the misindexation of some symmetry operators [75]. An iterative method to determine the experimental orientation relationship $T^{exp}_{\gamma\to\alpha}$ is thus proposed:

$$T_{n+1} = C_j^{-1} \cdot C_i \cdot \overline{T}_n \cdot M \tag{4.6}$$

In Equation 4.6, $\overline{T}_n$ is the input orientation relationship of an iteration and results in the output $T_{n+1}$. The average $\overline{T}_{n+1}$ calculated for all the intergranular misorientations will be used as the input in the next iteration. With a sufficient amount $n$ of iterations, $T_{n+1}$ becomes arbitrarily close to actual $T^{exp}_{\gamma\to\alpha}$. It should be noted that the actual orientation relationship is an average value ; some deviation from it is always to be expected because of local lattice distortions and slight differences between variants formed at different stages of the martensitic transformation [75]. A theoretical orientation relationship such as Kurdjumov-Sachs may be used as $T_0$ in the first iteration. The symmetry operators can be found using

Equation 4.4. As the correct indexation of the symmetry operators is crucial for the iteration to be succesfull, this step should be repeated after each iteration with $T_n$ as $T_{\gamma\rightarrow\alpha}$ to reduce the amount of misindexed symmetry operators at each iteration.

An automatic OR detection algorithm was created based on the proposed iterative method. The Kurdjumov-Sachs orientation relationship was assumed as the initial orientation relationship $T_0$. Equation 4.4 was used to determine the symmetry operators $C_i$ and $C_j$ for each experimentally determined misorientation. To avoid including any misorientations between different parent austenite grains, a minimum deviation angle of 3 degrees was selected as a threshold value for misorientations included in the analysis.

The algorithm was verified on experimental data obtained by the heat treatment of a 0.2C-2Mn-3Al-0.35Si-1Cu-0.5Ni sheet steel heated to 1200 °C at 5 °C/s, soaked for 3 minutes and quenched to room temperature at 50 °C/s. The specimens were prepared for EBSD and analyzed in the manner described in Section 4.2. A raster of 707x486 datapoints was collected using a step size of 0.5 $\mu$m, resulting in a dataset size of 343602 datapoints.

Post processing of the data was conducted on Matlab® with the MTEX texture and crystallography analysis toolbox developed by Bachmann et al. [90]. A grain map was assembled from the orientation pixel map with a 3 degree minimum grain boundary threshold. The misorientation dataset $M$ was assembled using Equation 4.1 with the average orientations of neighboring grain pairs as $O_{\alpha,i}$ and $O_{\alpha,j}$. For the high-aluminum steel, this resulted in 27600 misorientations between neighboring grain pairs for the analysis. The algorithm was run through 20 iterations on the data.

## 4.4 Parent austenite reconstruction

The parent austenite microstructure of the quenched specimens was investigated by reconstruction from martensitic EBSD data with a method similar to that suggested by Gomes and Kestens [82]. The aim was to develop a computationally efficient, fully automated algorithm suitable for the reconstruction of parent austenite in nonstrained microstructures. A full description of the Markov Cluster Algorithm can be found elsewhere [83]. Here, the focus is on how the Markov matrix $T_{G+I}$ is assembled and what operations it was subjected to in the reconstruction algorithm.

The reconstruction was performed with the MTEX toolbox. In the first step of the process, the orientation relationship between austenite and martensite was determined using the method outlined in the previous Section. In the second step, each intergranular misorientation was assigned a value determining a likelihood to be a misorientation between two martensite grains originating from the same parent austenite grain. The likelihood, with values ranging from 0 to 1, was determined using the Burr cumulative distribution survival function:

$$S(x|\alpha, c, k) = \frac{1}{[1 + (\frac{M_{mis}}{\alpha})^c]^k} \tag{4.7}$$

where $M_{mis}$ is the minimum deviation angle between a given intergranular misorientation and the experimentally obtained set of intramartensitic misorientations. $\alpha$, $c$ and $k$ are scale and shape parameters with values of 2, 5 and 1, respectively.

A graph cluster was then assembled from the grain map. First, a symmetric $m$-by-$m$ incidence matrix $G$ was generated, in which $m$ equals the total number of grains in the grain map and each individual element $e_{i,j}$ describes the edge $e = S_{i,j}$ between nodes (grains) $i$ and $j$. The diagonal elements in the matrix were set to 1. Each column of the matrix was then normalized by multiplying $G$ with a suitable diagonal matrix $d_n$:

$$T_{G+I} = Gd_n \tag{4.8}$$

The resulting stochastic matrix $M = T_{G+I}$ was then subjected to operations of expansion and inflation. Expansion consists simply of the multiplication of the stochastic matrix $M = T_{G+I}$ by itself:

$$M^2 = MM \tag{4.9}$$

Inflation consists of a Hadamard (elementwise) power of $r$ over $M^2$ and is followed by the normalisation of each column by multiplying the matrix with a suitable diagonal matrix $d_t$:

$$T_{G+I,2} = (M^2)^{\circ r} d_t \tag{4.10}$$

where $\circ r$ denotes the Hadamard power. The result is another stochastic matrix, in which the edges of nodes within clusters are strengthened and the node edges between clusters are weakened. After a sufficient amount of alternating sets of expansion and inflation, the intercluster edges become zero and the resulting graph describes a set of discrete clusters. The process can be made more efficient by pruning the matrix during each inflation step, prior to normalisation. In the pruning process, edges that fall below a certain threshold are set to zero.

An automated parent austenite reconstruction algorithm was created based on iterative orientation relationship determination and the Markov Cluster Algorithm. The inflation operator $r$ was set to 1.6 and the threshold value for pruning was set to 0.001. The stochastic matrix $T_{G+I}$ was run through alternating sets of expansion and inflation until convergence. Convergence was determined to have occurred when the difference between the maximum value in each column and the sum of Hadamard squares in each column was smaller than 0.001.

The resulting set of discrete clusters was then used to reconstruct the parent austenite orientation map in the manner described in Section 3.3.

# 5 Results and discussion

The verification of the proposed orientation relationship determination and parent austenite reconstruction algorithms, as well as the results of the dilatometry and quenching and partitioning experiments are described and discussed in this Chapter.

## 5.1 Verification of the iterative OR determination method

The evolution of the orientation relationship for the high-aluminum steel on each subsequent iteration is shown in Figure 5.1 as the angle between the close-packed planes $(111)\gamma$ and $(011)\alpha'$ and the close-packed directions $[\bar{1}01]\gamma$ and $[\bar{1}\bar{1}1]\alpha'$. The orientation relationship deviates steadily from the exact parallelism assumed by Kurdjumov-Sachs until it achieves a steady state value approximately in the 15th iteration.

The method was compared to the one proposed by Miyamoto et al. [75] based on manual selection of a parent austenitic grain from EBSD data. The parent austenite orientation for the selected grain was determined, after which $T_{\gamma\rightarrow\alpha}$ could be calculated for each orientation separately. This procedure was repeated for three manually selected parent austenite grains. The angles of misorientation between the close-packed planes and directions of the ORs are shown in Figure 5.2. There is a slight scatter in the three orientation relationships determined with the manual selection method. The average minimum deviation angle of the experimentally obtained misorientation dataset with the misorientation list determined by the orientation relationships was calculated to assess the fit of the orientation relationships

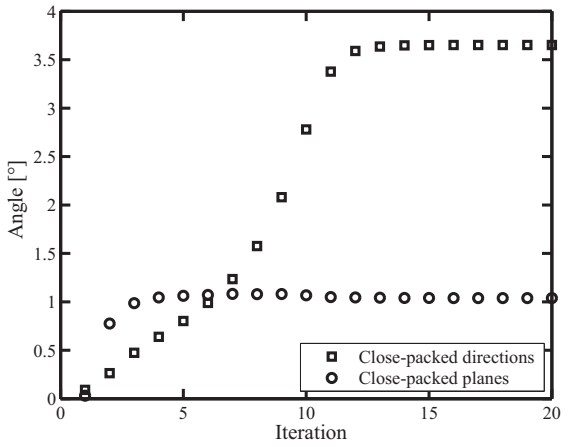


**Figure 5.1:** *Angles between the* $(111)\gamma$ *and* $(011)\alpha'$ *planes and the* $[\bar{1}01]\gamma$ *and* $[\bar{1}\bar{1}1]\alpha'$ *directions with respect to iteration number for the high-aluminum steel.*

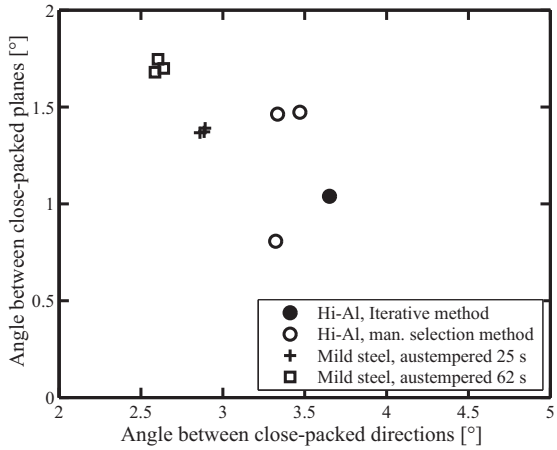


**Figure 5.2:** *Angles between the* $(111)\gamma$ *and* $(011)\alpha'$ *planes and the* $[\bar{1}01]\gamma$ *and* $[\bar{1}\bar{1}1]\alpha'$ *directions of the experimental orientation relationships.*

with experimental data. The average minimum deviation angle for the average orientation relationship between the three ORs determined with the manual selection method was 3.15 degrees, while for the iteratively determined orientation relationship it was 2.99 degrees.

The deviation between the iterative and manually determined orientation relationships is somewhat expected, as the manual selection method produces the orientation relationship from all of the orientations in a single, easily distinguishable parent austenite grain, whereas the iterative method employs the misorientations of all the grains for the same procedure. The difference in the average minimum deviation angle between the two ORs is neglibigle, but implies that both methods produce an equally usable result. The results for the partially austempered steels are also shown in Figure 5.2. The results show a very small amount of scatter and that a longer austempering time clearly affects the orientation relationship.

To visually analyse the suitability of the iteratively determined orientation relationship, the misorientations between grains in the analyzed high-aluminum steel EBSD dataset were categorized into three groups: intrapacket misorientations, interpacket misorientations and parent austenite grain boundaries. The intrapacket and interpacket misorientations were determined according to the classification by Morito et al. [5]). Figure 5.3a) shows the band contrast map of the EBSD measurement overlaid with the grain boundaries of the grain map. The boundaries have been colorized as green (intrapacket boundaries), red (packet boundaries) or black (parent austenite grain boundaries). The parent austenite grain structure is clearly visible and morphologically sound. While there are a few gaps in the parent austenite boundary network, these are the result of the particular grain pair misorientations falling under the minimum deviation angle threshold of 3 degrees. There are also some boundaries within the larger grains that have likely erroneously been classified as parent austenite boundaries: these are the result of local lattice distortions resulting in poor EBSD indexation that place the intergranular misorientations outside the minimum deviation angle threshold.

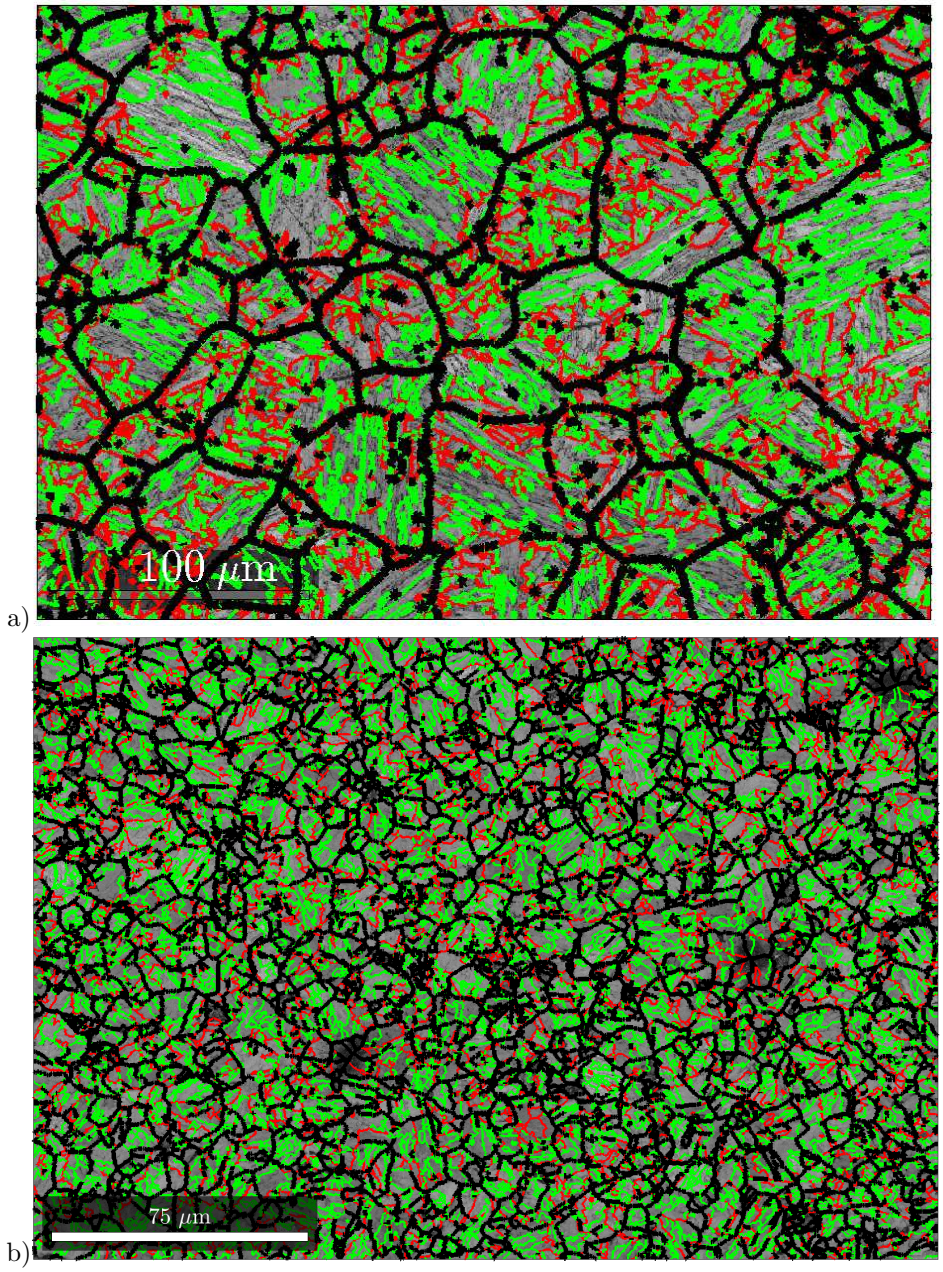


**Figure 5.3:** *Band contrast EBSD maps overlaid with parent austenite grain boundaries (black), intrapacket boundaries (green) and interpacket boundaries (red): a) high-aluminum steel with a martensitic microstructure, b) mild steel austempered for 62 s.*

A similar map is shown in Figure 5.3b) for the mild steel austenitized for 62 s. The parent austenite grain size is much finer and there are considerably fewer blocks and packets formed within each parent austenite grain. However, similarly to the high-aluminum steel, the parent austenite microstructure is clearly visible and morphologically sound. The orientation relationship between bainite and austenite would have been extremely difficult to determine using manual parent austenite grain selection. By comparison, the use of the grain pair misorientation dataset gave a large amount of useful data for OR determination with no manual data selection necessary.

The proposed algorithm was shown to work on both fully martensitic and partially bainitic steels. In all cases, an experimental orientation relationship was produced that gave a good average fit with the experimental data. The algorithm was verified to produce a comparable result to the manual parent grain selection method. It was shown that the repeatability of the method is excellent in the case of partially bainitic steels. It should be noted that for a mixed bainitic-martensitic microstructure, the determined OR is an average one that can be used to characterize both the martensitic and bainitic phases present in the microstructure.

## 5.2 Verification of the method for parent austenite reconstruction

The original EBSD grain map with IPF TD coloring is shown in Figure 5.5a). The dataset contains 5357 grains, from which MCL found 203 discrete clusters. Figure 5.4a) shows a part of the initial graph overlaid on a partial grain map before MCL processing. The graph is a typical example of clear clusters with sparse but strong connections to other clusters. Figure 5.4b) shows the groups of discrete clusters resulting from the process. The prior sparse connections have disappeared.

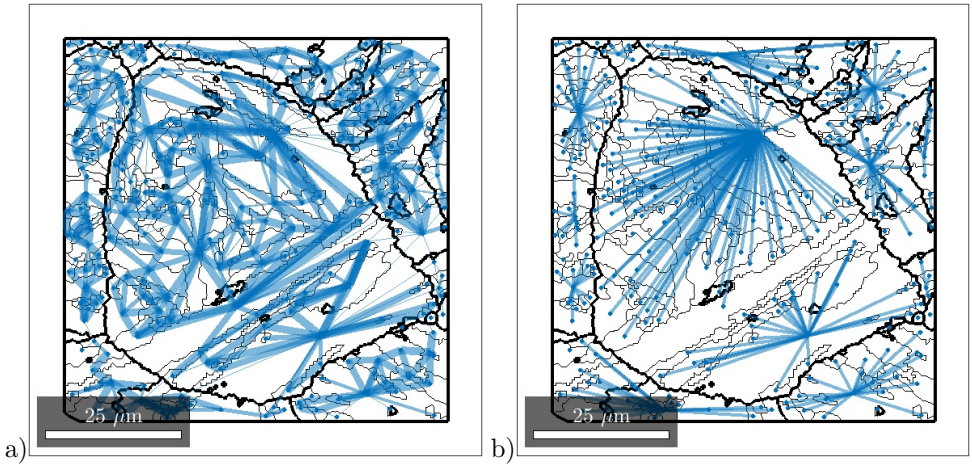


**Figure 5.4:** *Grain maps created from EBSD data with an overlaid graph cluster showing the connections between grains for a) the starting condition, b) after MCL, $r = 1.6$.*

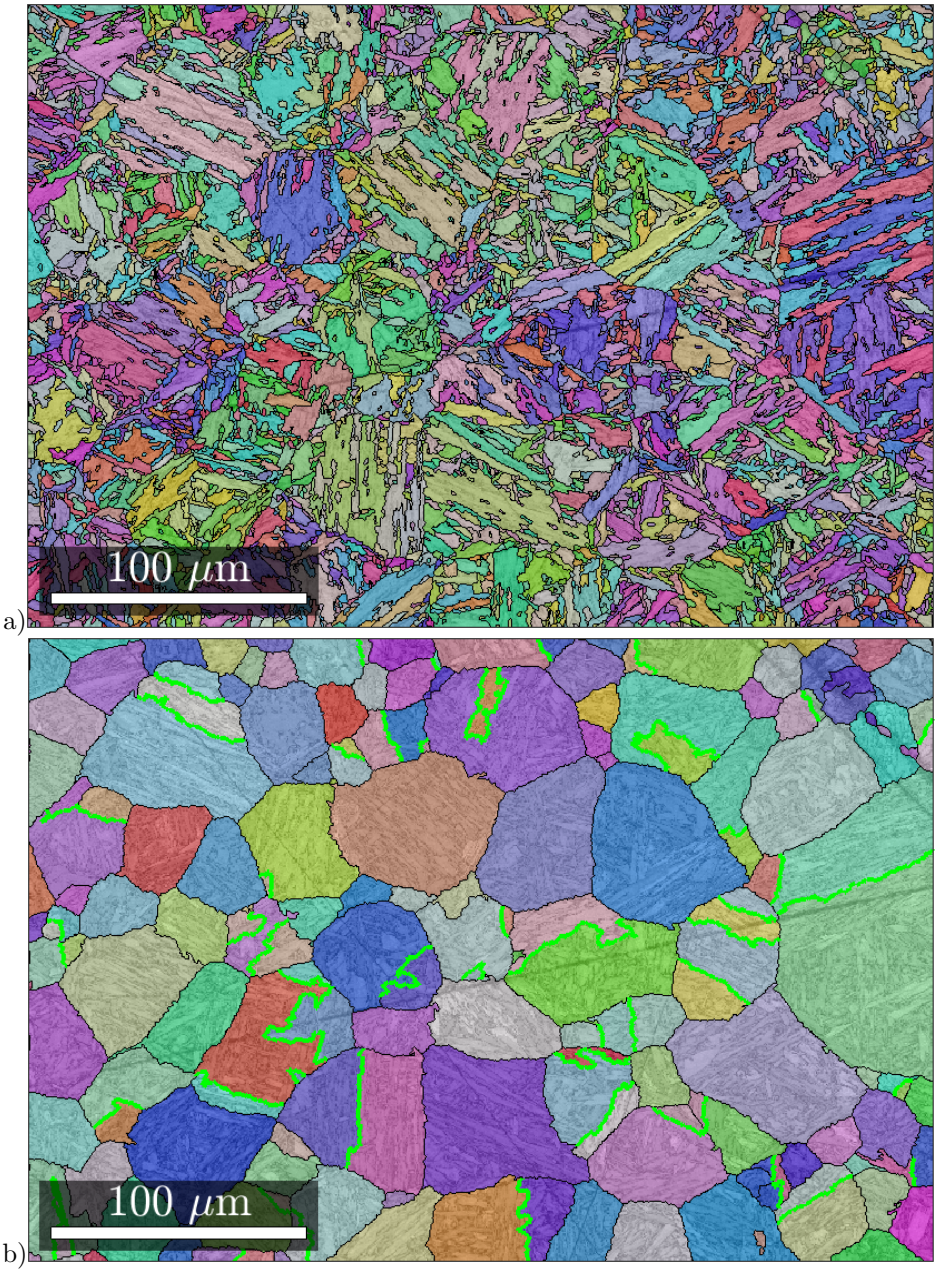


**Figure 5.5:** *a) Original EBSD band contrast map overlaid with IPF colored martensite grain map and b) reconstructed parent austenite grain map with IPF coloring.*

The parent austenite orientation was calculated separately for the orientation data in each cluster as described in Section 3.3. A separate grain map was then constructed from the reconstructed austenitic orientation dataset. The grain map with IPF coloring is shown in Figure 5.5b). The result of the reconstruction appears to largely follow the results of the grain boundary classification, with some clear exceptions. It is notable that the boundary reconstruction result does not take thermal twins (twin boundaries marked green in the reconstruction) in the parent austenite into account in any way; this is a consequence of the twins sharing variants with each other.

The reconstruction result can be evaluated based on the misorientation between a reconstructed austenite orientation and the original martensitic orientation. If the misorientation between these is close to the experimentally obtained orientation relationship in the previous section, the reconstruction can be considered good. The mean of the deviation angles between the martensitic/austenitic misorientations and the experimentally obtained orientation relationships was 2.14 degrees, indicating a successful reconstruction.

According to literature, the growth of individual laths in a packet occurs on the habit plane in the austenite. This means that the long axis of individual laths (that appear to have an acicular morphology on the two-dimensional specimen surface) should be oriented in the same direction as the traces of the $\{111\}\gamma$ family of planes on the specimen surface. Figure 5.6a) shows the $\{111\}\gamma$ traces of an individual parent austenite grain superimposed on a band contrast image showing the approximate lath morphology. The laths are oriented in the direction of the traces, as predicted by the phenomenological martensite nucleation theory [37].

The reconstruction of the austenitic orientation map makes it possible to analyze austenite texture and variant selection in martensite. Figure 5.6b) shows the transformation variants as per Morito et al. [5] for a single parent austenite grain. According to the phenomenological theory, laths oriented in the same direction share the same habit plane and thus belong to the same packet. This is confirmed by the visual observation of the variant indexation in Figure 5.6b). All variants in a single packet have been assigned to pixels belonging to laths oriented in the same direction.

A histogram of the variant distribution for the entire measured area is shown in Figure 5.7. It is clear that variants 1-6 with parallel $(111)\gamma$ and $(011)\alpha'$ are favored over others. In studies by Miyamoto et al. [76], this type of behavior was associated with the preferred nucleation of martensite with the $(111)\gamma$ and $(011)\alpha'$ parallelism, with $(111)\gamma$ being the primary slip plane in austenite. The slip plane had activated as a result of appr. 10 % plastic deformation prior to martensitic transformation. Figure 5.7b) shows an inverse pole figure in the rolling direction of the specimen of the reconstructed austenite orientations. There are indications of [001] and [111] type fibers. As the specimen was not subjected to hot deformation prior to quenching, the texture is likely inherited from the previous stage of microstructural evolution. During austenization, the nucleation of the austenite phase has evidently not been completely random. It has been observed by Li et al. [91] that during reverse transformation from a pearlitic structure, austenite preferably nucleates at high-angle boundaries of ferrite, often forming a Kurdjumov-Sachs-type orientation relationship to one of the boundary ferrite orientations.

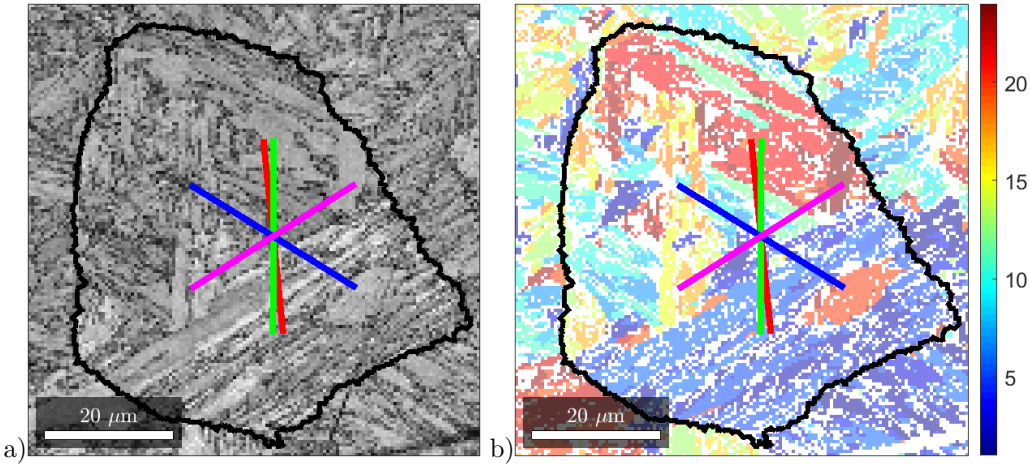


**Figure 5.6:** *a)A band contrast EBSD map with parent austenite grain boundaries overlaid. Traces of* $\{111\}\gamma$ *planes shown as colored lines. b) Transformation variants 1-24 for each reconstructed orientation pixel as per Table 3.2.*

.

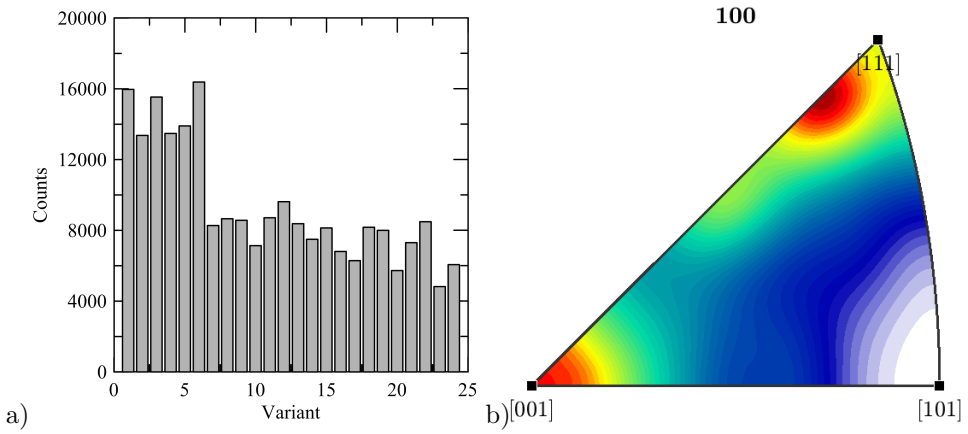


**Figure 5.7:** *a)Variant selection histogram for the reconstructed dataset. b) An inverse pole figure showing the reconstructed austenite texture in the rolling direction.*

## 5.3 Dilatometry experiments

The dilatometry experiments consisted of the measurement of $M_s$ temperatures with the methodology described in Chapter 4.1 for both fully austenitized and intercritically annealed specimens. The microstructure of the quenched samples was studied with the aid of electron backscatter diffraction and parent austenite reconstruction.

### 5.3.1 Full austenitization

EBSD studies were conducted on the specimens to determine their parent austenite grain size and texture by means of parent austenite reconstruction, as well as to assess the morphology and possible variant selection behavior of the martensite phase and their effects on $M_s$. Four datasets of 164x238 $\mu$m were collected for each specimen with a step size of 0.3 $\mu$m. Before parent austenite reconstruction, a grain map was assembled and the grains divided into intercritical ferrite and martensite based on band slope thresholding, a method used previously [92, 93] to succesfully separate ferrite and martensite. Band slope describes the slope of the intensity change between the background of the pattern and the band, essentially giving a numeric value to the visual sharpness of the Kikuchi bands. Each grain in the grain map was given a mean value of the measured band slope values, after which grains with a mean band slope above the threshold value were classified as intercritical ferrite. The threshold value was determined separately for each dataset based on the band slope histogram analysis. The orientation relationships between austenite and martensite were then determined using the iterative method described in Section 4.3. They are reported in Figure 5.8a) as the deviation angles between the close-packed directions and close-packed planes. There are no major differences in the OR between the cooling rates.

Following the reconstruction, the grain size of the austenite phase could be accessed directly from the processed data. The grain size of the reconstructed parent austenite grains is reported in Figure 5.8b) as a mean grain circle equivalent diameter weighted with grain areas. The grain size in steel B is in the 20 $\mu$m range, distinctly smaller than in steel A in the 50-70 $\mu$m range. The standard deviation of the austenite grains is large both because of the natural distribution of grain sizes in the measured datasets as well as the large size of the grains in relation to the dataset size. The fraction of intercritical ferrite was also determined for the specimens. This data is presented in Figure 5.9.

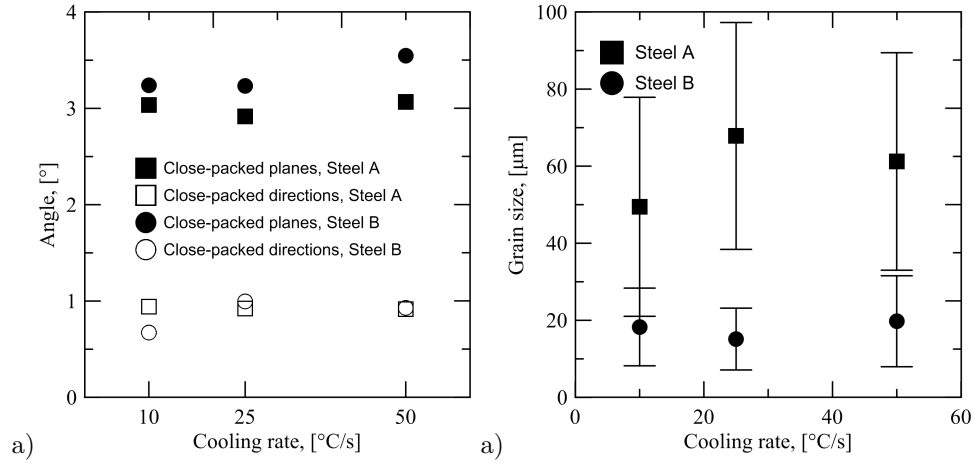


**Figure 5.8:** *a) The angles between the* $(111)\gamma$ *and* $(011)\alpha'$ *planes and the* $[\bar{1}01]\gamma$ *and* $[\bar{1}\bar{1}1]\alpha'$ *directions. b) Grain diameters for the reconstructed austenite phase.*

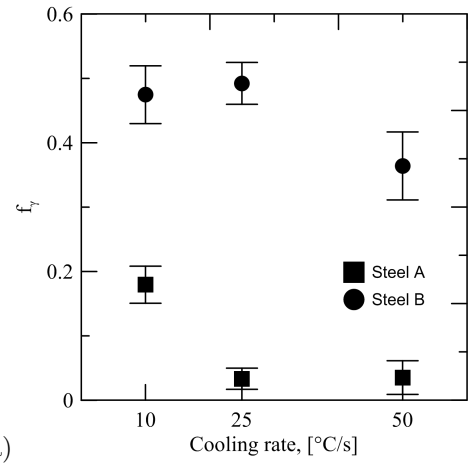


**Figure 5.9:** *The ferrite fractions measured for the steels annealed at 1200* °C *from EBSD scans by band slope grain averaging and thresholding.*

Band contrast images of the specimens are shown in Figures 5.10 and 5.11. It can be seen that for both steels, some intercritical ferrite has been retained in the microstructure for the cooling rates of 25 and 50 °C/s. In both cases, the amount of ferrite in the microstructure has clearly increased for the specimen with a cooling rate of 10 °C/s. The reconstruction result is shown in Figures 5.10b),d) and f) and 5.11b),d) and f). Despite the differences in the amount of intercritical ferrite, the morphology of the martensite is largely unchanged, indicating a similar mechanism of martensite formation. This is also supported by the small observed differences in the orientation relationships between martensite and austenite.

Dilatation during cooling could only be measured for the specimens cooled at a rate of 50 °C/s from 1200 °C. The $M_s$ measured for steel A was 420 °C and for steel B 388 °C. The measured values were significantly lower than the theoretically calculated values of 459 and 473 °C. The low $M_s$ value for steel B is at least partially explained by the presence of intercritical ferrite and its effect on the chemical composition on the austenite phase. For steel B the fraction of intercritical ferrite was approximately 34 %, while for steel A it was only approximately 3 %. Assuming full partitioning of carbon from the ferritic phase to austenite, the carbon content of the austenite at a ferrite fraction of 34 % would be approximately 0.31 wt-%. Recalculating for this carbon content would give $M_s = 406$ °C, closer to the observed value.

The dilatation curves along with the differential of the dilatational strain with respect to temperature are shown in Figures 5.12a) and b). Both steels show a gradual change in the rate of thermal contraction when cooling from 1200 °C. This might be an indication of a phase change occurring during cooling. However, it is possible that there is a significant thermal gradient present in the specimens during cooling (especially from a high temperature of 1200 °C, complicating the reliable analysis of dilatation curves. Still, based on the EBSD measurements, some degree of ferrite nucleation and growth is present in the specimens, most prevalent in steel B.

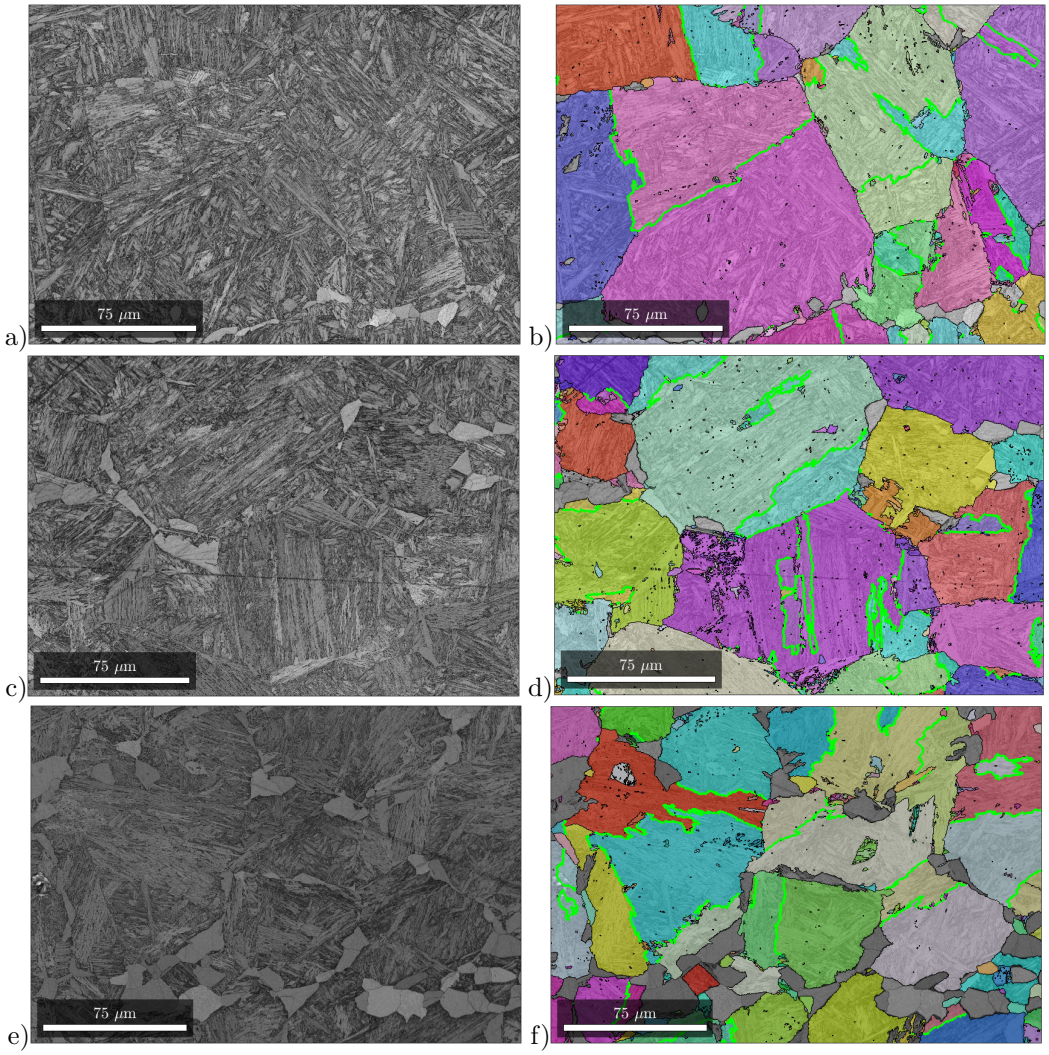


**Figure 5.10:** *EBSD band contrast image of Steel A annealed at 1200* °C *for 2 minutes and then quenched to RT at 50* °C/s*. Reconstructed austenite overlaid in IPF coloring (images b,d and f). Cooling rates of a) and b) 50* °C/s*, c) and d) 25* °C/s *e) and f) 10* °C/s.

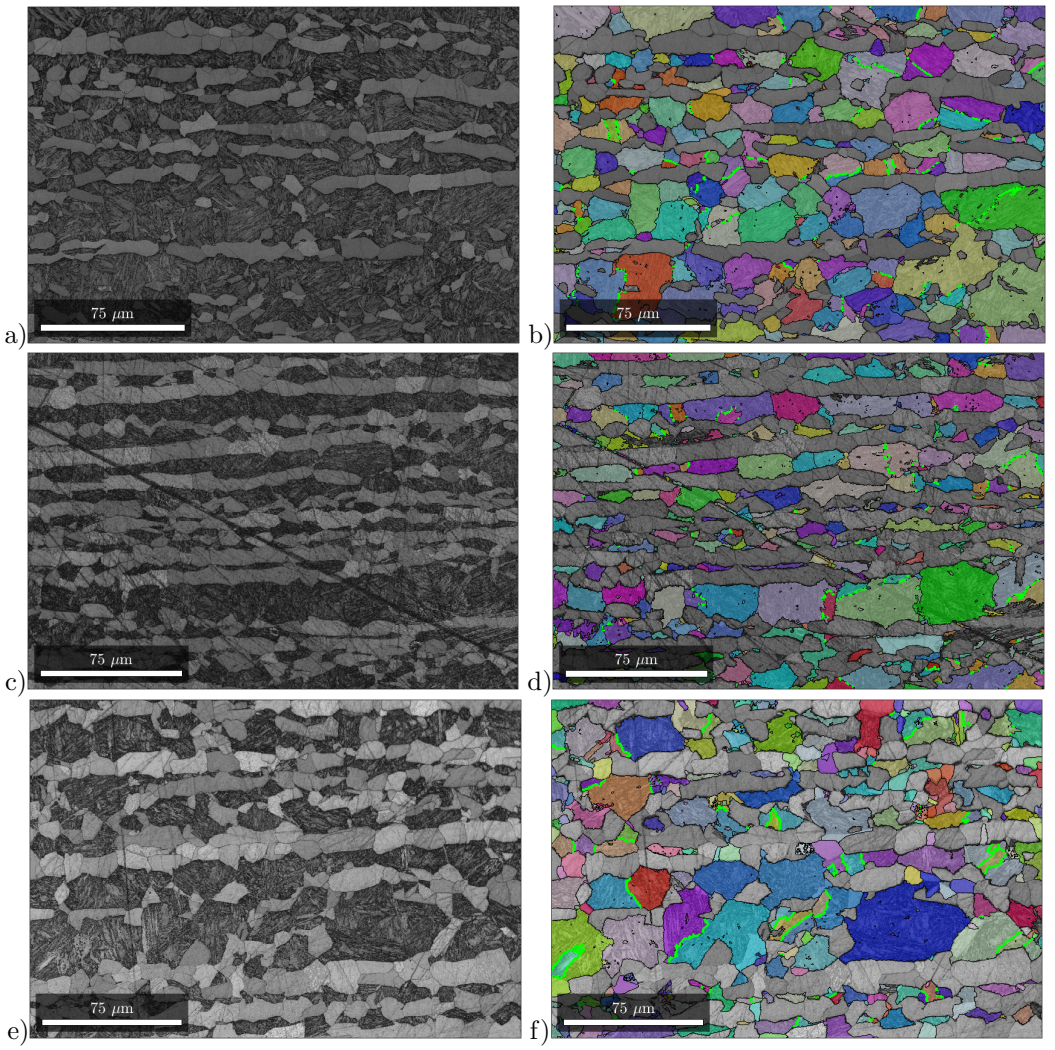


**Figure 5.11:** *EBSD band contrast image of Steel B annealed at 1200 °C for 2 minutes and then quenched to RT at 50 °C/s. Reconstructed austenite overlaid in IPF coloring (images b,d and f). CSL Σ3 type twin grain boundaries are indicated with a green color. Cooling rates of a) and b) 50 °C/s, c) and d) 25 °C/s e) and f) 10 °C/s.*

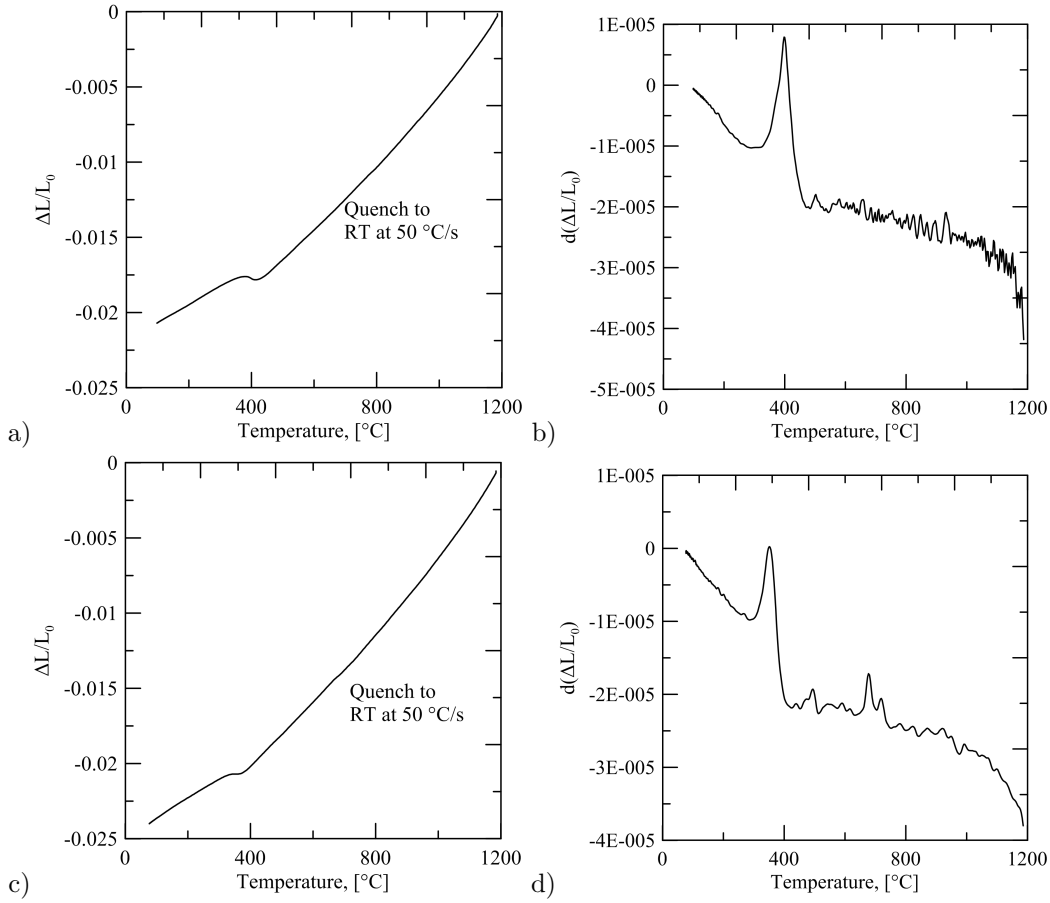


**Figure 5.12:** *Dilatation curves for steels A and B annealed at 1200* °C *for 2 minutes and then quenched to RT at 50* °C/s. *a) The dilatation strain of steel A, b) the differential of dilatiation strain in steel A with respect to temperature, c) the dilatation strain of steel B, d) the differential of dilatation strain in steel B with respect to temperature.*

### 5.3.2 Intercritical annealing

$M_s$ values were measured for the annealing temperatures of 750, 800, 850 and 900 °C for holding times of 3 minutes, 10 minutes and 1 hour and for the cooling rate of 25 °C/s. For 900 °C, only the holding time of 3 minutes was investigated. The measured $M_s$ values are compared against calculated $M_s$ in Figure 5.13 for all tested conditions. The measured $M_s$ temperatures fall well below the predicted values at all annealing temperatures and holding times. The numerical $M_s$ values are shown in Table 5.1.

There are three possible explanations for the unexpectedly low $M_s$ temperatures. The first explanation is that the chemical balance between the phases has not achieved equilibrium at the studied holding times. This explanation is not likely, because carbon is the major component affecting the $M_s$ temperature and its imperfect partitioning would raise $M_s$ rather than lower it.

The second possible explanation is the effect of the parent austenite grain size on $M_s$, as discussed in Section 2.1. To determine the parent austenite grain size, EBSD studies were conducted on the specimens annealed at a temperature of 850 °C. The grain size data was accessed by means of parent austenite reconstruction as per Section 5.2. Three sets of 35x24 $\mu$m were measured with a step size of 0.05 $\mu$m. Prior to the reconstruction, the intercritical ferrite data was separated with band slope analysis, using a similar methodology as with the fully austenitized specimens. The reconstruction resulted in approximately 200 reconstructed austenite grains per handled dataset. The austenite grain sizes are shown in Figure 5.14 as circle equivalent diameters. Table 5.1 shows the effect of parent austenite grain size on the amount of undercooling below $M_s$ calculated with Equation 2.4. The parent austenite grain size was recalculated for the Equation as mean linear intercepts from the reconstructed EBSD data with the point-intercept methodology by Lehto et al. [94]. Table 5.1 clearly shows that the effect of parent austenite grain size on undercooling below $M_s$ is not enough to explain the differences between the measured and theoretical values. It should

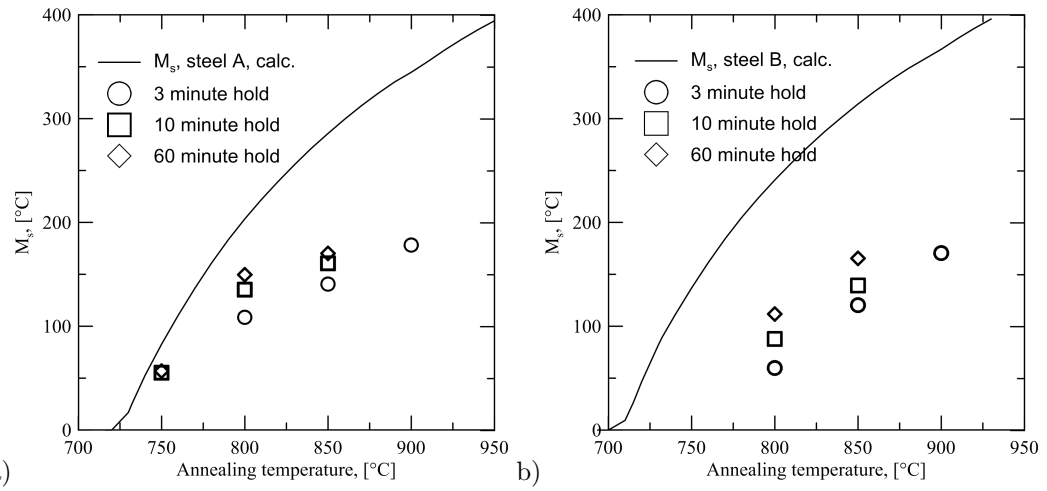


**Figure 5.13:** *$M_s$ temperature with respect to annealing temperature, a)steel A, b) steel B.*

**Table 5.1:** *Measured $M_s$ temperatures in* °C. *No test indicated by '-'. Values in parentheses indicate the amount of theoretical undercooling to calculated $M_s$ values caused by the measured parent austenite grain size.*

| Steel | $T_a$ | $M_s, calc.$ | $M_{s,3min}$ | $M_{s,10min}$ | $M_{s,60min}$ |
|---|---|---|---|---|---|
| A | 750 | 82.83 | <RT | 55 | 57 |
| | 800 | 203.5 | 109 | 135 | 150 |
| | 850 | 285.8 | 141 *(-75)* | 161 *(-70)* | 170 *(-67)* |
| | 900 | 344.6 | 178 | - | - |
| B | 750 | 136.9 | <RT | <RT | <RT |
| | 800 | 240.9 | 60 | 88 | 112 |
| | 850 | 314.1 | 120 *(-73)* | 139 *(-68)* | 165 *(-66)* |
| | 900 | 366.8 | 170 | - | - |

also be kept in mind that Equation 2.4 by Yang and Bhadeshia [35] describes the effects of grain size in a general case of a fully austenitized steel with a well-defined martensite lath morphology and may therefore not be suitable for the evaluation of the effect of austenite grain size on martensite formation in dual-phase steels.

The third explanation for the unexpectedly low $M_s$ temperatures is that the JMATPRO® predictions for phase fractions at the annealing temperatures are simply incorrect. Because of the high solubility of carbon in the austenite phase and the considerable effect of carbon content on $M_s$, the $M_s$ temperature is sensitive to even a small variation in the austenite fraction during intercritical annealing.

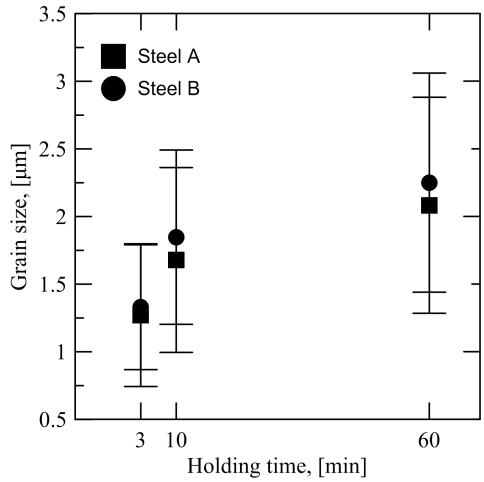


**Figure 5.14:** *Reconstructed parent austenite grain size obtained from EBSD maps for the holding temperature of 850* °C.

The austenite fractions could be determined directly from the reconstructed austenite EBSD datasets and are shown in Figure 5.15a). Keeping in mind that the electron backscatter diffraction sample areas were rather small for reliable quantitative analysis, the phase fractions of austenite prior to the martensitic transformation were also determined via optical microscopy for steels A and B held at 850 °C for 1 hour. The specimens were prepared for optical microscopy in the manner described in Section 4.2 and etched with Klemm's I tint etchant. Six images were taken at a 500x magnification. The images were converted to 8-bit grayscale and the phases separated from each other based on intensity value thresholding. The phase fractions measured via optical microscopy are shown in Figure 5.15b). For correlation, phase fractions were also extrapolated by comparison of the measured $M_s$ values with the curves shown in Figure 4.1e). Figure 5.15a) shows that the extrapolated austenite fraction is somewhat smaller than the one measured directly from optical micrographs, on the same level with the austenite fractions measured from the reconstructed EBSD datasets. However, if the phase fractions calculated from the measured $M_s$ values are offset with the correction for austenite grain size determined with Equation 2.4, the correlation becomes rather good with the austenite fractions measured directly from optical micrography. It is a likely explanation that the low measured $M_s$ values are a result of a combination of factors: low fractions of intercritical austenite at the martensite start temperature as well as the small parent austenite grain size.

There are two possible explanations for the low intercritical austenite phase fraction. Either the balance of phases is lower at the studied intercritical annealing temperatures than indicated by the predictions, or the phase fractions have changed during cooling to room temperature. The change of phase fractions during cooling would be facilitated by the Widmanstätten growth of ferrite into austenite, diffusion-aided interfacial migration, or the formation of bainite. No clear ferritic Widmanstätten-type protrusions were found in the

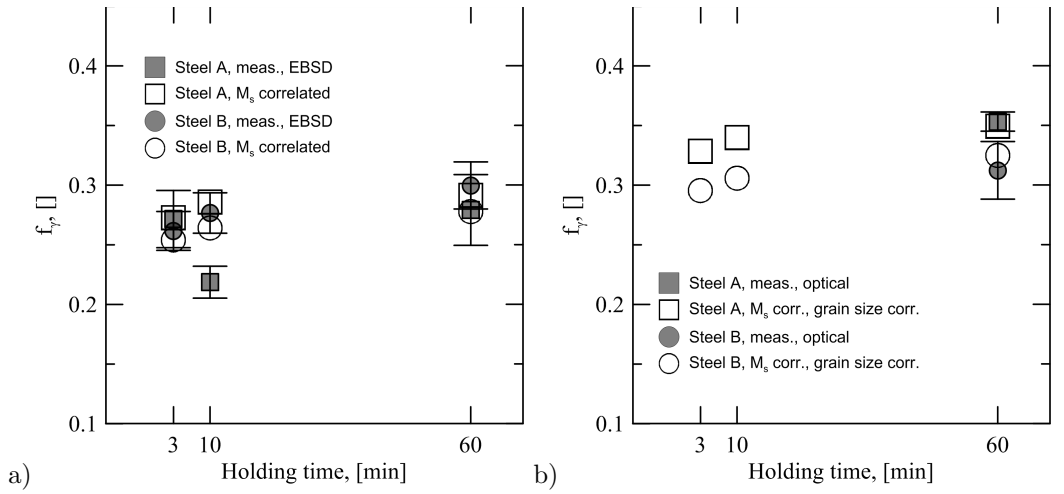


**Figure 5.15:** *a) Reconstructed parent austenite grain size obtained from EBSD maps for the holding temperature of 850 °C and b) phase fractions from $M_s$ correlation and EBSD parent austenite reconstruction.*

microstructure, leaving the interfacial growth of ferrite into austenite or bainite formation as the most likely possibility. The interpretation of the cooling curves in the high-temperature regime where diffusion-aided phase transformation might occur is not straightforward, however.

Figure 5.16 shows the dilatometric curve for Steel A held at 850 °C for 10 minutes and quenched to room temperature. The Figure is a typical example of the cooling portions of the observed dilatometric curves, which should have discernible deviations from linearity if ferrite or pearlite growth or bainite formation would be taking place during cooling. Such features are not evident in Figure 5.16, precluding reliable quantitative analysis. Figure 5.17 shows differential dilatation plots for the specimens cooled from 850 °C. The martensite transformation shows clearly as a sharp peak near the end of the cooling cycles. There are smaller deviations in the data as well, especially in the plot for steel B and in the plot for steel A held for 1 hour at the annealing temperature. Small peaks close to the temperature of 400 °C indicate a possibility of limited bainite formation. For steel B, there are also peaks discernible around the temperature of 700 °C, which might indicate ferritic growth. In the full austenitization dilatometry, the hardenability of steel B was shown to be poorer, as more intercritical ferrite had been formed at a cooling rate of 25 °C/s. It is reasonable to assume that some ferrite growth has taken place during cooling from intercritical annealing temperatures for steel B. In the case of steel A, the differential plots are more difficult to interpret. The sharp peaks at high temperatures in Figures 5.17a),c) and d) are likely to be the result of vibration caused by the initiation of the argon gas cooling, masking possible fluctuations caused by phase change. The austenite phase fraction at $M_s$ is likely influenced both by ferrite formation during cooling as well as a lower than expected phase fraction at the annealing temperature.

The dual-phase microstructures obtained from the EBSD measurements are shown in Figures 5.18 and 5.19. Both steels consist of intercritical ferrite with islands of martensite

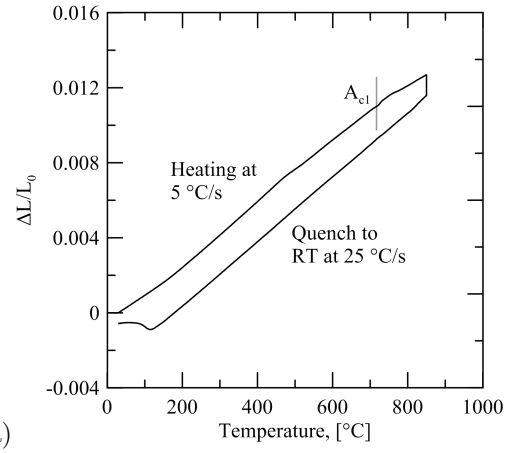


a)

**Figure 5.16:** *a) The dilatometric curve for steel A held at 850* °C *for 1 hour and quenched to room temperature at 25* °C/s.

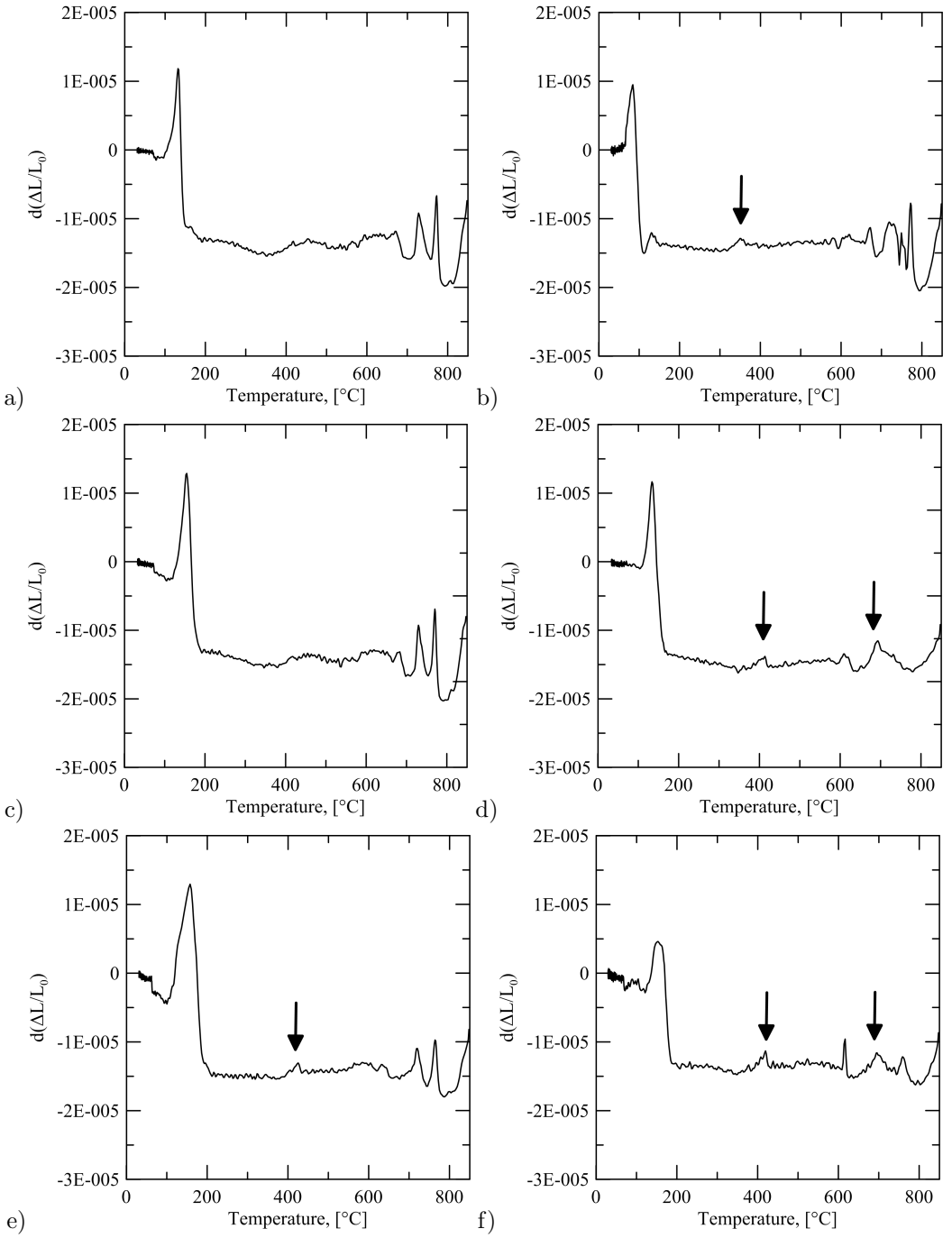


**Figure 5.17:** *Differential dilatation plots with respect to temperature for steels held at 850* °C *and quenched to room temperature at 25* °C/s*: a) steel A, 3 minute hold, b) steel B, 3 minute hold, c) steel A, 10 minute hold, d) steel B, 10 minute hold, e) steel A, 1 hour hold, f) steel B, 1 hour hold.*

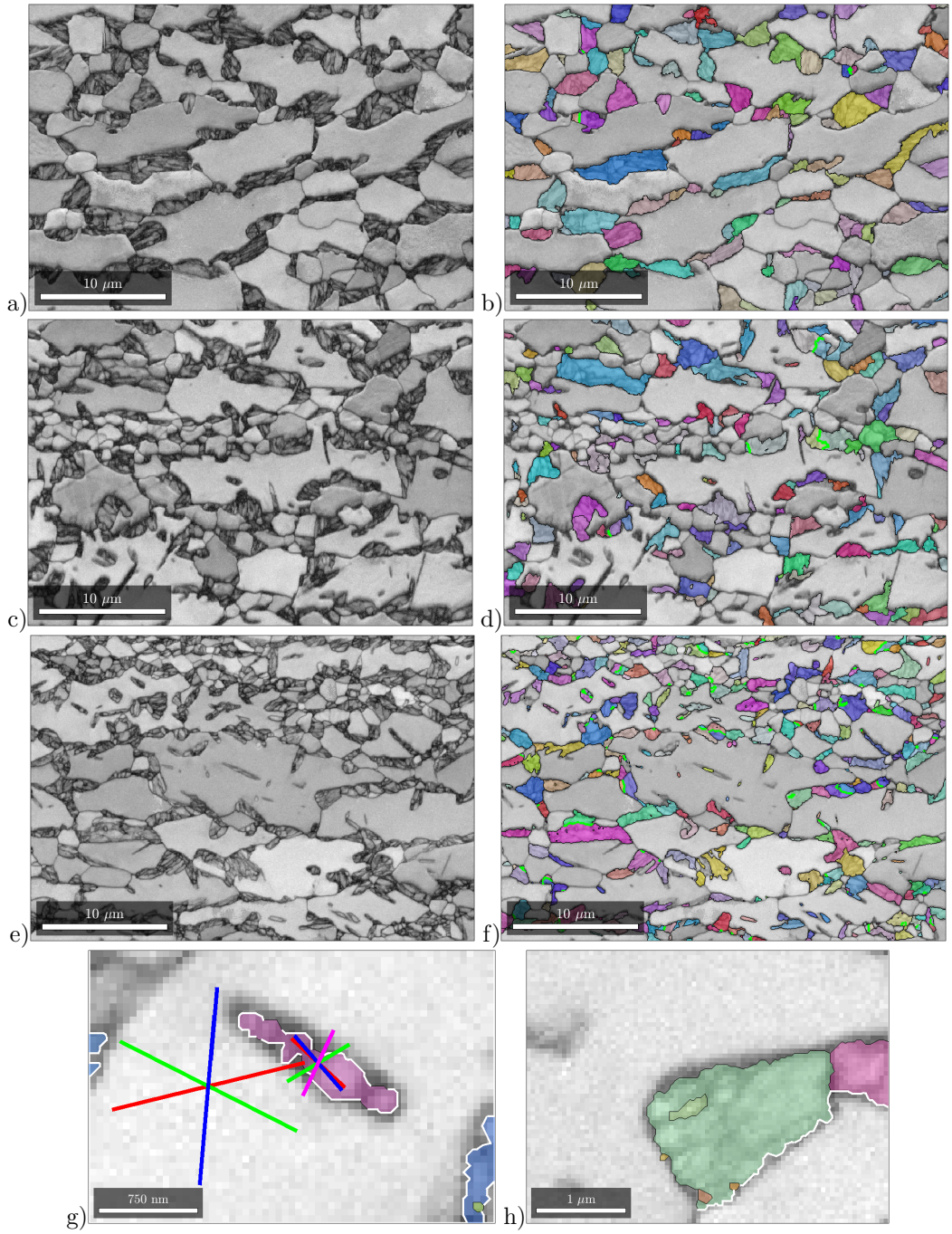


**Figure 5.18:** *EBSD band contrast images of steel A (images a,c and e) with reconstructed austenite overlaid in IPF coloring (images b,d and f). Holding times of a) and b) 60 minutes, c) and d) 10 minutes e) and f) 3 minutes. g) Example of apparent displacive grain growth.* {011} *plane traces indicated in ferrite and* {111} *in austenite. h) Reconstructive growth into ferrite. K-S-type boundary indicated in white.*

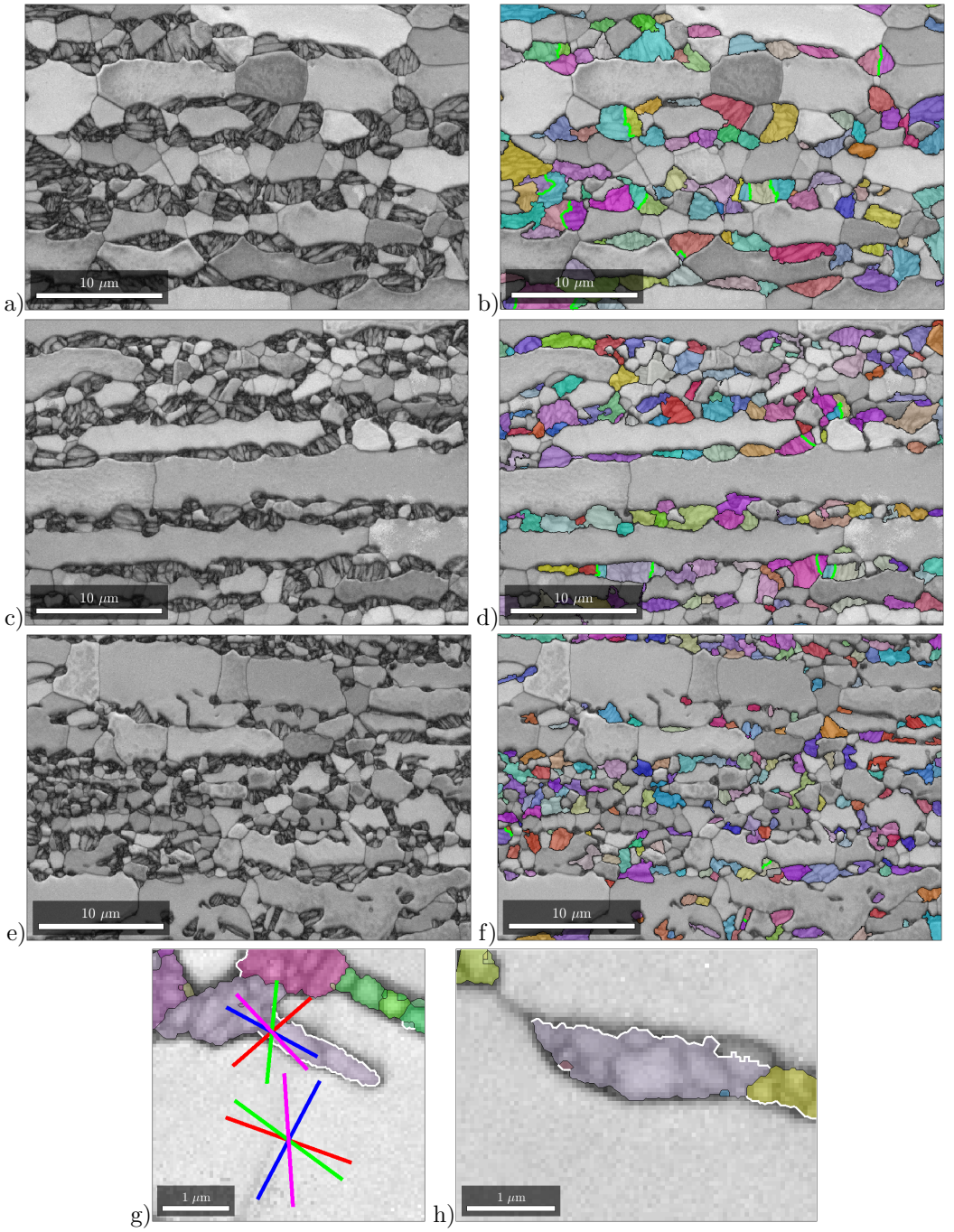


**Figure 5.19:** *EBSD band contrast images of steel B (images a,c and e) with reconstructed austenite overlaid in IPF coloring (images b,d and f). Holding times of a) and b) 60 minutes, c) and d) 10 minutes e) and f) 3 minutes. g) Example of Widmänstatten-type grain growth.* {011} *plane traces indicated in ferrite and* {111} *in austenite. h) Reconstructive growth into ferrite. K-S-type boundary indicated in white.*

located mostly at ferrite grain boundaries. There appears to be a bimodal distribution in the intercritical ferrite size, ranging from sub-micron to large elongated grains of over 10 $\mu$m in diameter. The martensite formed in the specimens is for the most part of the single-packet type, with each packet consisting of multiple variants. The presence of multiple variants in a packet is explained by the need for effective plastic self-accommodation, as the martensitic transformation will be constrained by both small parent austenite grain size and the increased carbon content resulting from intercritical annealing. The block structure within the packets is very fine, with each block consisting only of a single variant.

Most of the parent austenite has nucleated at the grain boundaries of the recrystallized ferrite grains, likely after carbide dissolution has provided a carbon-rich volume preferential to austenite nucleation. Nearly all of the reconstructed parent austenite grains were found to share a Kurdjumov-Sachs type orientation relationship with at least one of its ferritic neighbors; when this was the case, the growth direction of the austenite grain was away from the ferrite grain with this type of ordered boundary. Ryde et al. [95] have noted that the orientation relationship between intercritical austenite and ferrite is closer to the K-S than to the Nishiyama-Wasserman OR. This was also the case in this study, as shown by the angular deviation histogram in Figure 5.20. Figure 5.20 shows the histogram of misorientation angles of the predefined K-S, N-W and Kelly [96] orientation relationships with the measured boundary misorientations between intercritical ferrite and reconstructed austenite. Interestingly, there appears to be a bimodal distribution in the histogram showing the deviation angles for the Kurdjumov-Sachs OR. This indicates that there may be some misindexations of the individual misorientations in the histogram, if the true orientation relationship differs from K-S [75].

To study this further, the OR between intercritical ferrite and reconstructed austenite was determined iteratively in a similar manner as outlined in Section 4.3 for steel A annealed for 1 hr. This experimentally obtained orientation relationship is plotted on a $(001)\gamma$ stereographic projection in Figure 5.21 along with experimental data. Each individually measured martensite-austenite misorientation is re-indexed and shown in Figure 5.21 as the orientation relationship of $(111)\gamma$ and $[\bar{1}01]\gamma$ between $(011)\alpha$ and $[\overline{1}\overline{1}1]\alpha$, which are seen to be almost but not exactly parallel. The measurements are presented as contour maps, with the peaks of the contours naturally coinciding with the experimentally determined orientation relationship (presented as white circles). Figure 5.21 shows that there is a deviation of approximately 1.5 degrees between $[\bar{1}01]\gamma$ and $[\overline{1}\overline{1}1]\alpha$ directions.

The primary mode of parent austenite growth appears to be reconstructive in the direction of the ferritic grain with a shared incoherent interface. Considering that the activation energy of movement for an incoherent interface has been determined to be smaller than that of coherent or semicoherent interfaces [42], this is not surprising. There are also several parent austenite grains that have nucleated inside intercritical ferrite. In these cases, the parent austenite grains have typically assumed an acicular morphology. The long axis of these elongated grains is parallel to the trace of a {011} plane in the ferrite. These types of parent austenite grains are in a minority in the processed EBSD datafiles. Figures 5.18g) and h) show examples of both types of parent austenite grains for steel A and 5.19g) and h) for steel B.

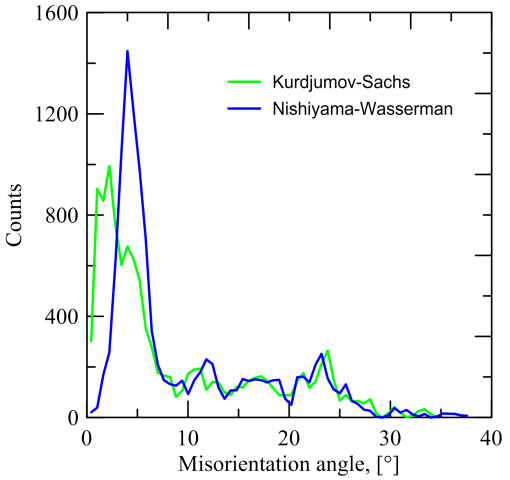


**Figure 5.20:** *Histogram of deviation angles between martensite-austenite boundary misorientations and certain predefined orientation relationships. Determined from EBSD measurements on steel A annealed for 1 h.*

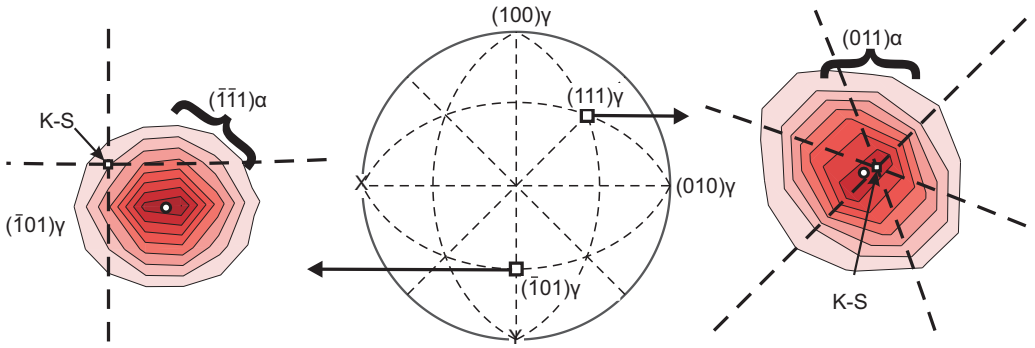


**Figure 5.21:** *(001)γ stereographic projection showing the Kurdjumov-Sachs (indicated with arrows) and the experimentally obtained OR ( indicated with circles) between parent austenite and adjacent intercritical ferrite in steel A annealed for 1 hour at 850 °C. The measured martensite-austenite misorientations are shown as density contours of the orientation relationship of (111)γ and $[\bar{1}01]\gamma$ between (011)α and $[\bar{1}\bar{1}1]\alpha$. The experimentally determined OR coincides exactly with the peaks of the density contours.*

## 5.4 Quenching and partitioning treatments

### 5.4.1 Q&P with calculated optimal parameters

The quenching temperature for the initial Q&P treatments was selected as 270 °C based on the theoretical calculations with an annealing temperature of 900 °C, as described in Chapter 4.2.

Optical micrographs for the studied steels etched with Klemm's I tint etchant are shown in Figure 5.22 a) - d). The martensite phase appears as distinct dark brown, ferrite as blue and retained austenite as white. For both steels, the microstructure has retained a considerable amount of intercritical ferrite. In Figure 5.22b), the dark brown martensite has been replaced by an off-white phase, which based on the tint color is identified as austenite. Curiously, the amount of ferrite appears to grow in both steels with increased holding time: in Figures 5.22a) and c), the microstructure consists of large ferritic islands surrounded by martensite grains, whereas in Figures 5.22b) and 5.22d) the ferrite islands have become an interconnected matrix.

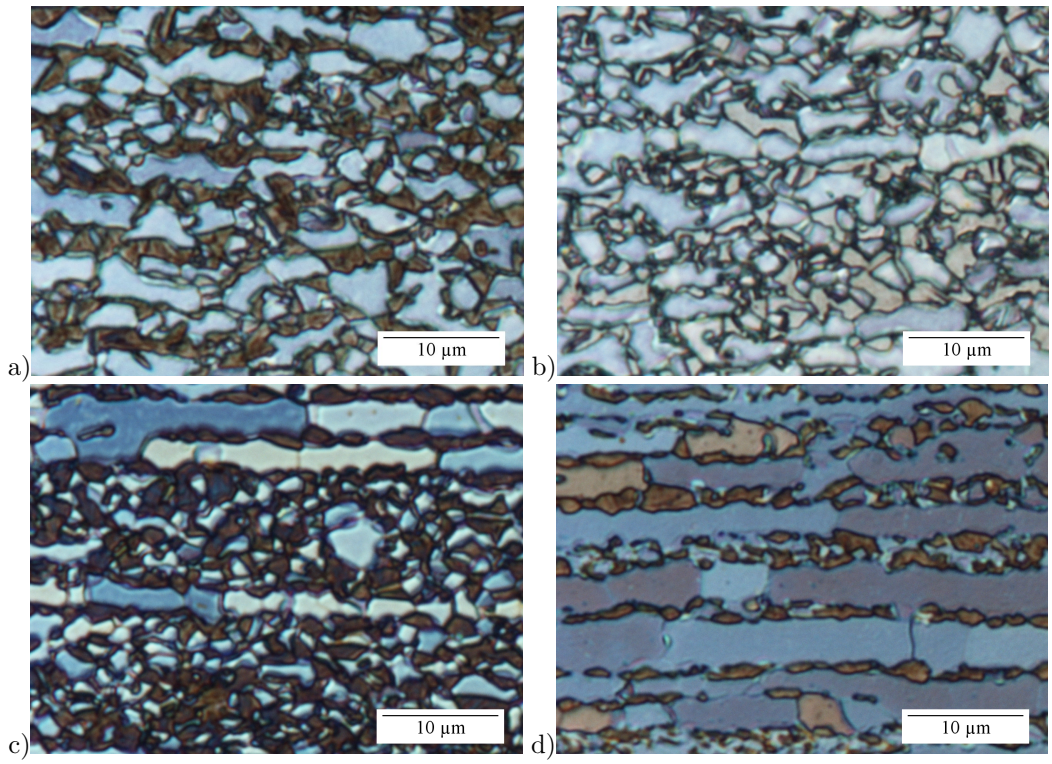


**Figure 5.22:** *Optical micrographs of steel etched with Klemm's I tint etchant: a)steel A, partitioned for 10 s, b) steel A, partitioned for 1000 s, c) steel B, partitioned for 10 s, d) steel B, partitioned for 1000 s. Partitioning at 450* °C

The ferrite phase in Steel B (and to a lesser extent in Steel A) is somewhat elongated. The elongated features are likely inherited from the hot and cold rolling processes of the steel and possibly also affected by the segregation of alloying elements during casting. During the laboratory hot rolling process, the steel has gone through a temperature regime of approximately 1200 - 900 °C, after which it has been quenched to 600 °C and allowed to cool slowly. Both steels have therefore been in an intercritical state during hot rolling, resulting in local chemical variation as the chemical constituents have diffused between phases. The microstructure of steels A and B after hot rolling and cooling to RT are shown in Figures 5.23a) and b). For both steels, the microstructure consists of recrystallized ferrite and secondary phases likely formed into austenite during cooling.

The Figures show that the steels have been in a coarse dual-phase state when subjected to cold rolling. This has led to an heterogenous dislocation distribution in the material during deformation, which has in turn likely affected recrystallization behavior. In addition, the carbides in the microstructure have been similarly heterogenously distributed, which has affected the nucleation of austenite during the Q&P heat treatment. The cold-rolled microstructures are shown in Figure 5.23c) and d).

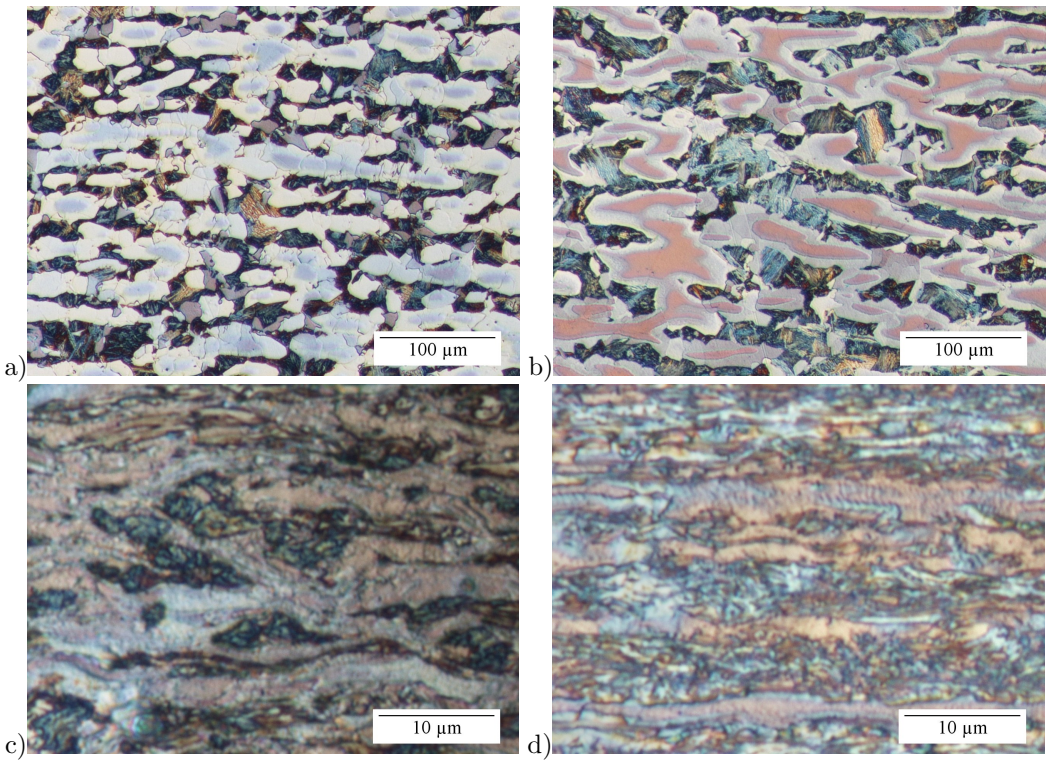


**Figure 5.23:** *Optical micrographs of steels A and B etched with Klemm's I tint etchant: a)steel A, hot rolled, b) steel B, hot rolled, c) steel A, cold rolled, 90 % reduction and d) steel B, cold rolled, 90 % reduction.*

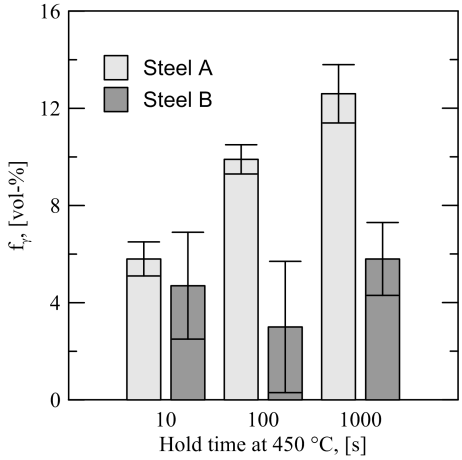


**Figure 5.24:** *The retained austenite contents measured for the quenched and partitioned steels.*

The retained austenite contents of the Q&P treated steels were measured by XRD and are shown in Figure 5.24. The amount of retained austenite clearly increases for Steel A with increased partitioning time, while for steel B there is no extensive variation of retained austenite content.

EBSD measurements of the specimens are shown in Figure 5.25. The microstructure of steel A consists of large ferritic grains and blocky retained austenite with a heterogenous grain size distribution. Steel B shows a banded ferrite structure with small-sized blocky retained austenite next to martensite islands interspersed with smaller ferrite grains. The austenite remaining in the microstructure was not associated with martensite but had been retained as blocky grains at intercritical ferrite grain boundaries or within ferrite grains.

Based on the XRD results and the observed microstucture in EBSD and optical micrographs, it appears that no martensitic reaction has taken place at the calculated optimal quench temperature. During partitioning, the steels have remained in an intercritical state. From the XRD measurements for steel A it is clear that there is some mechanism of austenite stabilization at work. As virtually all of the carbon has already diffused into the austenite during intercritical annealing, the fraction of phases needs to change in order for austenite to stabilize further. One possible mechanism for this is the formation of carbide-free bainite in the austenite phase. However, at least in the case of Steel A, the morphology of the retained austenite phase seen in Figure 5.25a) does not support this explanation, as the blocky retained austenite in steel A is not associated with bainitic lath structures. The microstructure of steel B is more difficult to interpret. The smaller amount of martensite in the micrographs of the specimens held for 1000 s suggests that epitaxial growth of intercritical ferrite takes place during partitioning. This growth is associated with gradual transfer of carbon from the ferrite phase to the austenite. During final quenching, limited martensite transformation can then take place, depending on the length of holding time: some grains have been completely stabilized, while others have transformed completely. The heteroge-

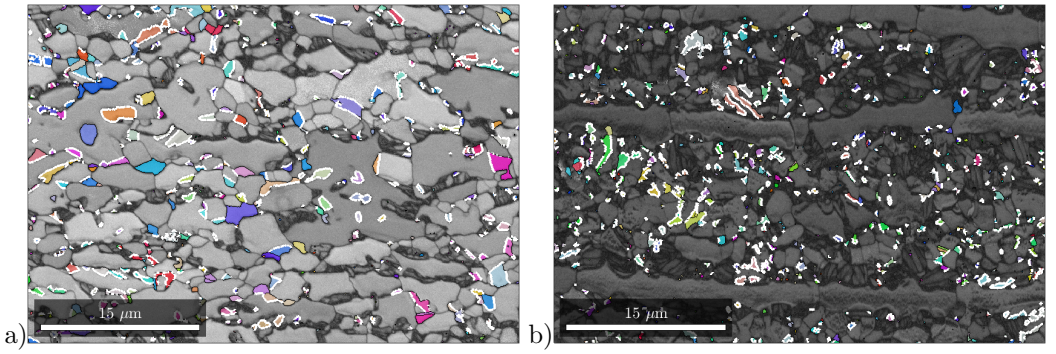


**Figure 5.25:** *EBSD band contrast image with austenite overlaid in IPF Z coloring for a)steel A, b) steel B. 100s partitioning at 450 °C. Grain boundaries marked with white indicate close fit with the Kurdjumov-Sachs orientation relationship between austenite and neighboring ferrite.*

nous distribution of austenite grain size is one probable cause for this behavior, as smaller grains will be more mechanically stable [35]. The stress-strain curves for the steels are shown in Figure 5.26. All of the tested steels exhibited continuous yielding and a high degree of work hardening during tension, except for a single Steel A specimen held for 10 s that unexpectedly broke at the edge of the gauge section close to the radius, Figure 5.26. All of the tested specimens showed increase in elongation and corresponding decrease in UTS with the increase in holding time at the partitioning temperature (450 °C). It is clear that in addition to retained austenite content, the morphology of the microstructure as a whole affects mechanical properties. In the case of steel A partitioned for 10s, the martensitic matrix has been incapable of supporting the deformation of the ductile ferritic grains, resulting in premature fracture. Care should be taken, then, to ensure that the initial annealing results in a continuous ferritic matrix as well as large, homogeneously sized austenite islands.

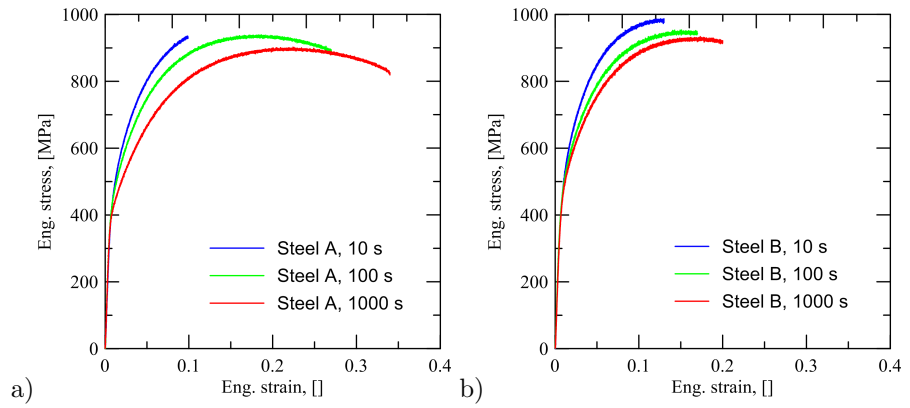


**Figure 5.26:** *Stress-strain curves for the steels annealed at 900 °C for 3 minutes, quenched to 270 °C and partitioned at 450 °C: a) steel A, b) steel B.*

### 5.4.2 Q&P parameters selected according to dilatometry

The quenching and partitioning parameters were selected according to the results of the dilatometry experiments for the intercritically annealed specimens. The dilatometry curve for the specimen held at a temperature of 850 °C for 3 minutes was analyzed and the temperatures of 50 and 75 °C were selected as the initial quench temperatures. The heat treatment cycle is presented schematically in Figure 5.27.

Salt bath heat treatments were made to obtain specimens for tensile testing. 18 mm wide strips were cut from the cold rolled sheets and heat treated by immersion in a 850 °C salt bath for a holding time of 3 minutes. The specimens were then immersed in a heated oil bath for interrupted quenching, after which they were immediately transferred to a 450 °C salt bath for partitioning. Finally, the specimens were quenched to room-temperature water. An additional set of specimens was manufactured with a heat treatment cycle that was otherwise similar but the initial annealing was done by heating in a tube furnace for 6 minutes. This corresponds to heating to annealing temperature at approximately 5 °C/$s$ and a holding time of 3 minutes. The heating rate in a salt bath is quite rapid and may not reflect the processing environment in a continuous annealing line.

Sub-sized tensile specimens with a 6 mm gage length and 3.5 mm gage width were manufactured from the heat treated specimens. The tensile direction was the direction transverse to the rolling direction. Prior to tensile specimen manufacture, sections were cut from the ends of the strips for retained austenite measurement with XRD and quantitative carbide analysis using Mössbauer spectroscopy. The XRD specimens were prepared by chemical polishing with a solution of 10:10:1 de-ionized water:hydrogen peroxide (70% water:30% H2O2):hydrofluoric acid (52% water:48% hydrofluoric acid) until 0.2 mm of material had been removed from the surface. After the measurement, EBSD specimens were prepared from the XRD samples by cutting a cross-section from the sample and then preparing the specimen as per Section 4.2. Three measurements were made on a 35x24 $\mu$m area for each specimen quenched to 75 °C using a step size of 0.05 $\mu$m. The Mössbauer specimens were ground by hand to 0.1 mm thickness and then immersed in the chemical polishing solution until they had thinned to approximately 20 $\mu$m thickness. In addition, dilatometry experiments were made with the TA805L dilatometer at the Colorado School of Mines to study the dilatometric changes of the specimens during quenching and partitioning. 5x10mm strips

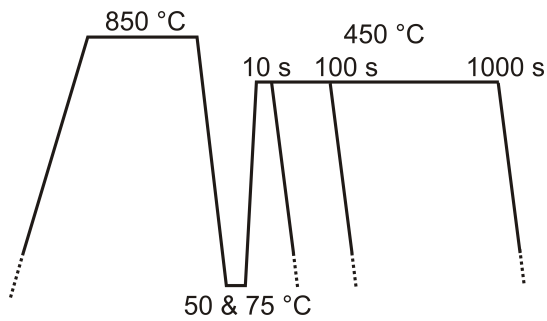


**Figure 5.27:** *A schematic of the heat treatment cycle for the Q&P tests.*

were cut from the sheets and induction heated in a low vacuum to the annealing temperature. After holding, the specimens were quenched with an argon gas jet at a rate of 25 °C/s to the quench temperature, held for 10 s and then heated to the partitioning temperature at a rate of 50 °C/s. After partitioning, the specimens were cooled to room temperature at a rate of 25 °C/s.

EBSD examination of the salt-bath and furnace annealed specimens revealed a microstructure consisting of intercritical ferrite and austenite interspersed with islands of martensite. Retained austenite with two distinct morphologies could be distinguished: blocky austenite at intercritical ferrite boundaries as well as austenite retained after an incomplete martensitic transformation. Example microstructures are shown in Figure 5.28. The effect of annealing on the microstructure is evident in the EBSD measurements: the specimens immersed for 3 minutes in the 850 °C salt pot have a much finer intercritical ferrite size when compared to the furnace-annealed specimens. In addition, many grains in the salt pot specimens have sub-grain boundaries, indicating incomplete recrystallization. The ferrite grain sizes for the specimens are shown in Figure 5.30c).

The retained austenite content was determined by XRD, supplemented with the Mössbauer technique for the salt pot annealed specimens. The specimens annealed in the salt pots have retained a considerable amount of austenite compared to the furnace annealed specimens. XRD analysis indicates some changes in the retained austenite content of the specimens during partitioning. However, the standard deviation of the measurements is significant and the Mössbauer results indicate more stable behavior. Figure 5.30b) shows the retained austenite and carbide content measured with the Mössbauer technique; it is evident that 3 wt-% of aluminum is enough to prevent cementite formation even at an extended holding time. At an aluminum content of 2 wt-%, a limited amount of carbides have formed after partitioning for 1000 s. The low amount of carbides present in the microstructure precluded the resolution of $\eta$-carbide and cementite, so they are referred here only to as "carbide".

TEM analysis was undertaken to determine the type of carbides present in the microstructure. Carbon extraction replicas were prepared from the same specimens used for the Mössbauer studies and subjected to examination in a TEM. The only type of carbide found in these studies were niobium carbides ranging from 5 to 20 nm in diameter (an example shown in Figure 5.29). The carbides were found finely dispersed within the ferritic grains. The orientation relationship between the carbides and the surrounding ferrite could not be determined, as the surrounding metallic matrix had fully dissolved in the replica. It is likely that the niobium carbides have not been fully dissolved during intercritical annealing. However, the effect of these carbides on possible carbon partitioning can be considered neglibigle, both because of their position far from any austenite-martensite interfaces as well as the very small amount of total carbon tied by the compounds.

All of the XRD measurements indicated a very high carbon content in the austenite phase, in the range of 1.3 - 1.5 wt-%. The carbon content was also measured using the Mössbauer method for the Steel B partitioned for 1000 s, indicating $X_c = 5.2$ at-% (approximately 1.2 wt-%). The austenite has clearly been enriched with carbon during the heat treatment. The exact mechanism of carbon enrichment will differ depending on whether a parent austenite grain has undergone partial martensite transformation before the partitioning stage. If

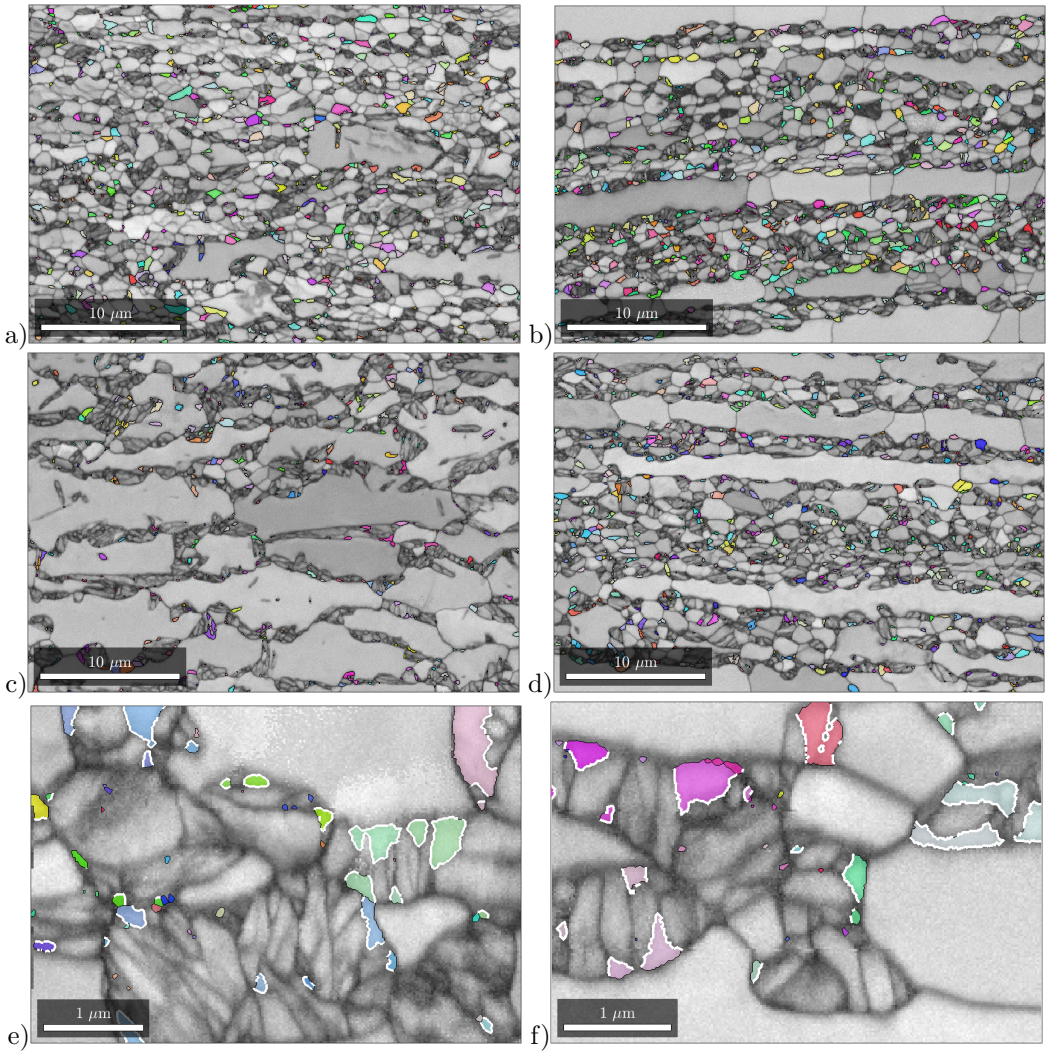


**Figure 5.28:** *EBSD band contrast images of steel A and steel B with retained austenite overlaid in IPF coloring: a) and b) Salt pot annealing for 3 minutes at 850 °C followed by quenching to 75 °C and 100 s partitioning with a) Steel A and b) Steel B. c) and d) Furnace annealing for 6 minutes at 850 °C followed by quenching to 75 °C and 10 s partitioning with c) Steel A and 100 s partitioning with d) Steel B. e) Close-up of the microstructure in c) with 0.002 μm step size showing austenite retained after an incomplete martensitic transformation. K-S-type boundary indicated in white. f) Close-up of the microstructure in d).*

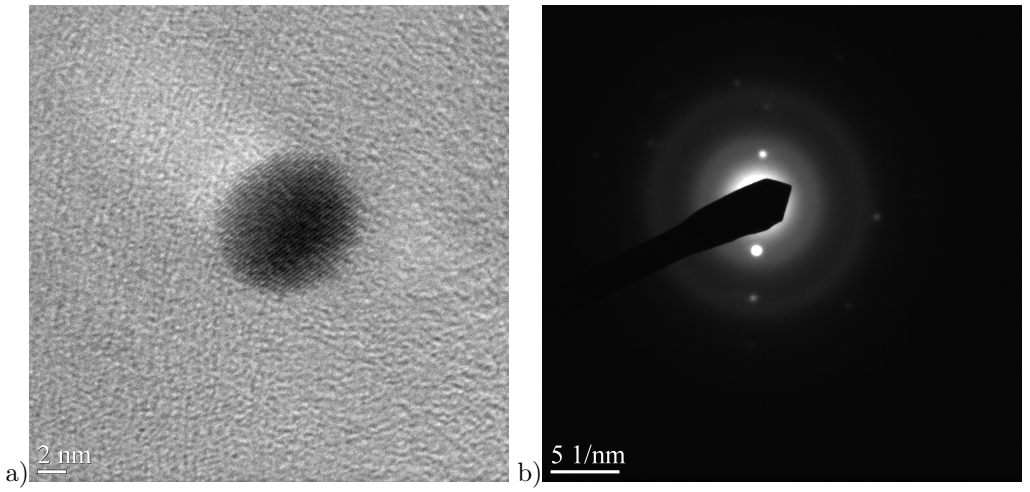


**Figure 5.29:** *a) Niobium carbide found in a carbon extraction replica of salt pot annealed steel B quenched to 75 °C and partitioned for 1000 s and b) selected area diffraction pattern from the carbide in a).*

a martensite transformation has occurred, carbon will partition to austenite rapidly from the new neighboring martensitic laths. If the parent austenite grain remains untransformed, some type of phase change is still necessary to free up carbon for enrichment. Possible mechanisms for this type of phase change are a bainitic transformation or the migration of ferrite boundaries into austenite during the partitioning stage. A third possibility is that during its initial formation, the carbon content has been locally high enough for the austenite to achieve room-temperature metastability directly. In the salt bath heated specimen, several austenite grains appear wholly untransformed either to bainite or martensite, leaving locally high carbon content and interfacial migration as the possible stabilization mechanisms.

Figure 5.31 shows the partitioning stage of the dilatation curves for selected specimens. In the Figures, $t = 0$ s indicates the measurement point where the registered thermocouple value reaches $T = 450$ °C. For all specimens, there is a near-instantaneous expansion after $t = 0$ s and a more gradual expansion until approximately 40-60 s. The initial very rapid expansion is likely at least partially due to the thermal homogenization throughout the bulk of the specimen. This is followed by a more gradual expansion that could be related to the saturation of the austenite phase with carbon [97], or possibly the formation of bainite or isothermal martensite. However, the formation of these phases will be limited by the carbon that has partitioned earlier during intercritical annealing. Assuming that carbon has fully partitioned between the phases and that the amount of intercritical austenite is approximately 27 vol-% as observed during dilatometry studies, the austenite phase would contain approximately 0.7 wt-% carbon. Using the semi-empirical equations by Bhadeshia [98], the increased carbon would depress the bainite start temperature to approximately 424 °C. If substitutional alloying elements also partitioned during intercritical annealing, the bainite start temperature would be depressed to approximately 309 °C. Of course, the possibility of bainite formation cannot be completely precluded based on empirical formulas. How-

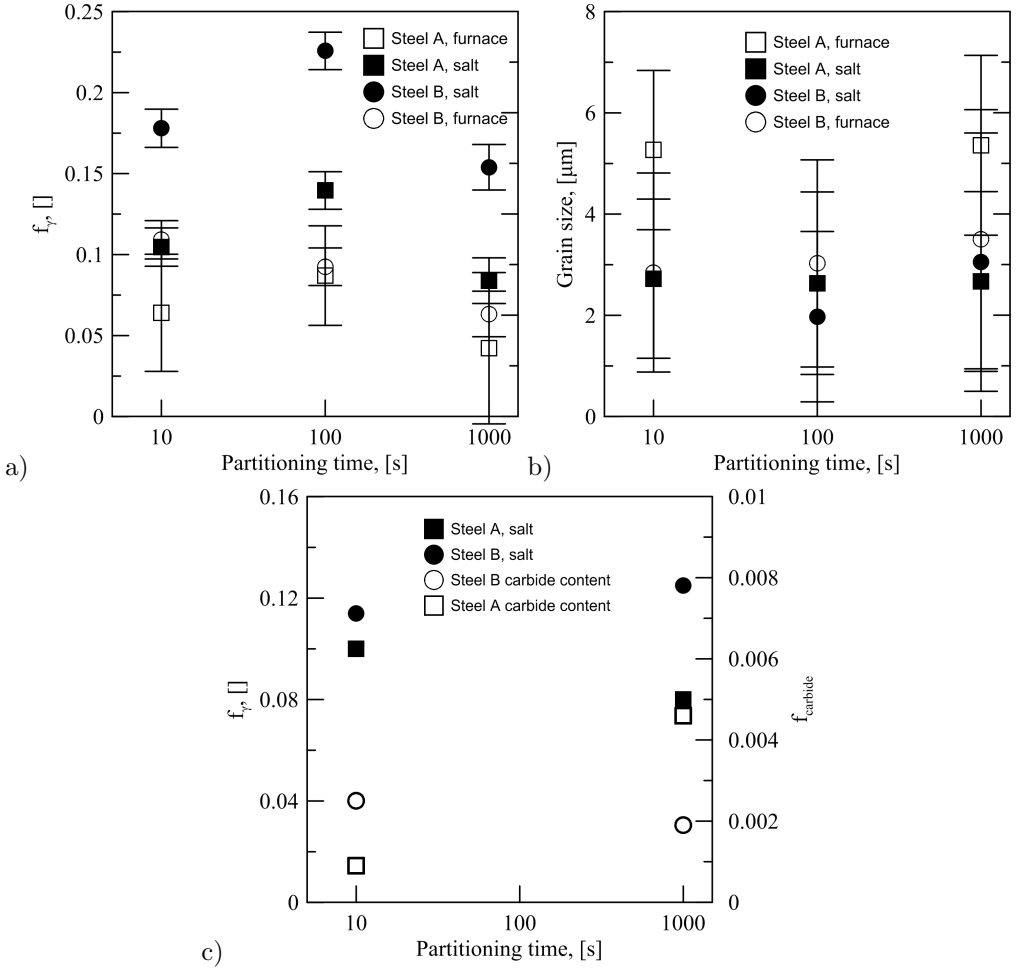


**Figure 5.30:** *Steels annealed at 850 °C, quenched to 75 °C and partitioned at 450 °C: a) The retained austenite fraction measured with XRD, b) grain sizes of the intercritical ferrite phase measured with EBSD and c) volume fractions of austenite and carbides in the steels measured with the Mössbauer method.*

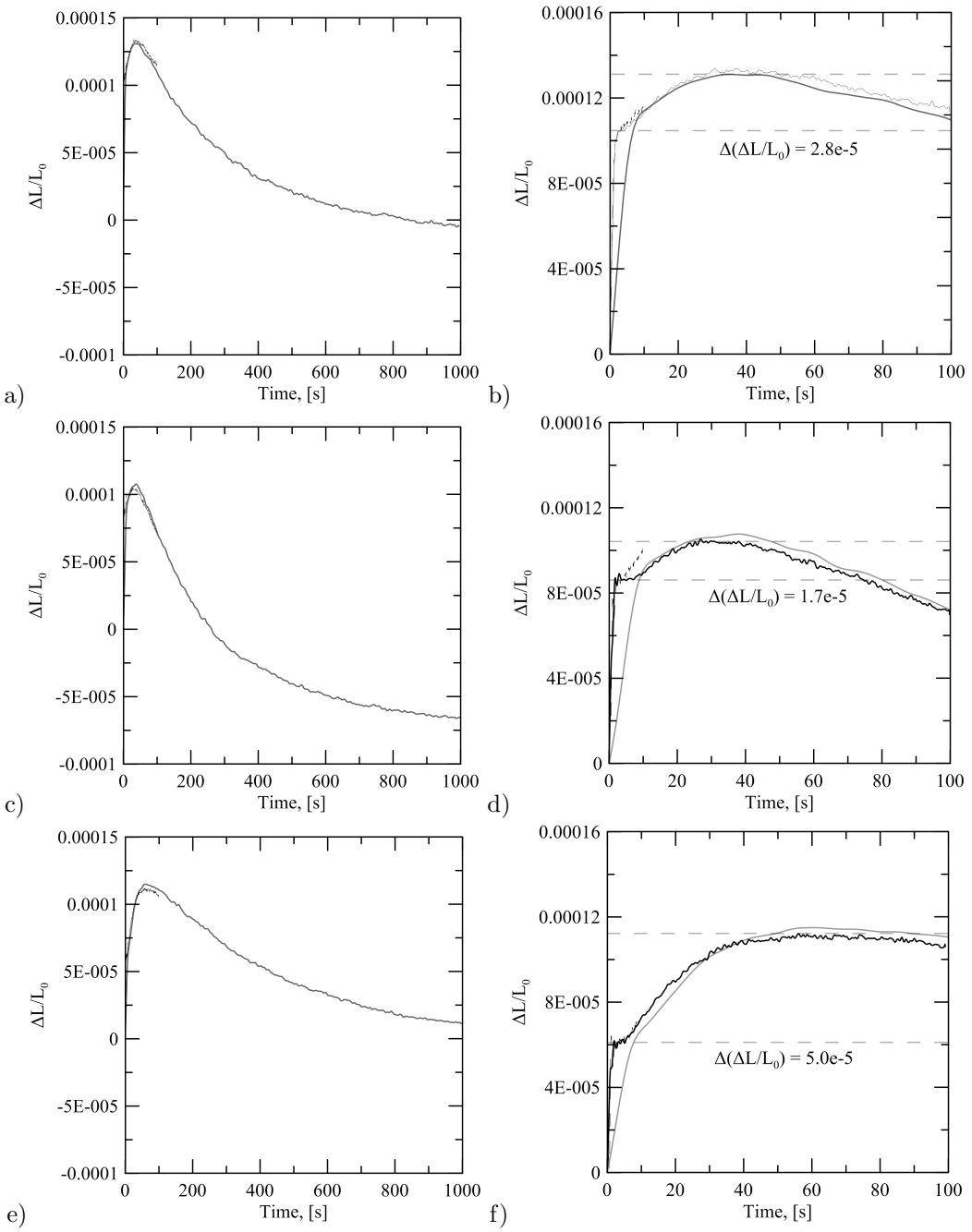


**Figure 5.31:** *Dilatometric curves for Steel A showing portions of the dilatation curves directly after the specimen has reached the partitioning temperature with partitioning times of 10, 100 and 1000 s. The dilatation strain has been set to zero at reaching 450* °C*. A) 3 minute annealing, $T_Q$ = 75* °C*, c) 10 minute annealing, $T_Q$ = 75* °C*, e) 10 minute annealing, $T_Q$ = 100* °C*, b),d) and f) curves showing the 0-100 s portion of a),c) and e) respectively. The number in the figures indicates the difference between the dashed horizontal lines.*

ever, microstructural examination and TEM studies did not reveal the presence of interlath cementite or fine intra-lath carbides associated with bainite formation. Looking at Figure 5.30a), there is a maximum in retained austenite content at partitioning times of 100 s. This would coincide somewhat with the peak of expansion in the partitioning dilatometry curves. It should be remembered that according to conventional Q&P theory, carbon partitioning should be extremely fast for nanoscale interlath retained austenite; however, the size of the retained austenite is in most cases larger than this, extending possible partitioning times.

Examples of the stress-strain curves for the steels are shown in Figure 5.32. The lack of a specific yield point, continuous yielding, and a high strain hardening rate exhibit the typical behavior of high-strength dual-phase steels. The uniform elongation of the salt bath heated steel is, notably, higher than for strict dual-phase steels with an otherwise similar microstructure. The total elongation is also very high, which is partially explained by the non-standard dimensions of the sub-sized tensile specimen. The use of the Oliver equation as implemented by ISO 2566/1 [99] can be used to estimate the total elongation for a standard test geometry:

$$A_2 = A_1 \times (\frac{k_1}{k_2})^n \tag{5.1}$$

where $A_2$ is the calculated elongation value, $A_1$ is the known elongation value, $k_1$ and $k_2$ are the proportionality ratios of the two test pieces, and $n$ is a material dependent constant. The standard adopts $n = 0.4$. The recalculated elongation values for a standard tensile specimen

**Table 5.2:** *The heat treatment parameters of the tensile tested specimens along with the results from the tensile tests.*

| Steel | $T_a$, [°C] | $T_q$ [°C] | $T_p$, [°C] | $t_p$, [s] | $Rp_{05}$,, [MPa] | $UTS$, [] | $Ag$, [MPa] | $\varepsilon_{total}$, [] | $\varepsilon_{cor.}$, [] | $n$, [] |
|---|---|---|---|---|---|---|---|---|---|---|
| A | furnace | 50 | 450 | 10 | 874 | 996 | 0.10 | 0.30 | 0.23 | 0.08 |
| | | ” | ” | 100 | 834 | 1005 | 0.09 | 0.25 | 0.20 | 0.09 |
| | | ” | ” | 1000 | 756 | 955 | 0.12 | 0.29 | 0.23 | 0.11 |
| | | 75 | ” | 10 | 734 | 953 | 0.13 | 0.31 | 0.24 | 0.12 |
| | | ” | ” | 1000 | 764 | 988 | 0.13 | 0.33 | 0.26 | 0.12 |
| A | salt | 50 | 450 | 10 | 731 | 1082 | 0.12 | 0.22 | 0.18 | 0.17 |
| | bath | ” | ” | 1000 | 758 | 1014 | 0.14 | 0.27 | 0.21 | 0.15 |
| | | 75 | ” | 100 | 780 | 992 | 0.17 | 0.32 | 0.21 | 0.11 |
| B | furnace | 50 | 450 | 10 | 823 | 986 | 0.10 | 0.20 | 0.16 | 0.09 |
| | | ” | ” | 100 | 870 | 1015 | 0.10 | 0.20 | 0.16 | 0.08 |
| | | ” | ” | 1000 | 837 | 967 | 0.10 | 0.17 | 0.13 | 0.08 |
| | | 75 | ” | 10 | 806 | 987 | 0.12 | 0.24 | 0.19 | 0.1 |
| | | ” | ” | 100 | 810 | 966 | 0.12 | 0.23 | 0.18 | 0.09 |
| | | ” | ” | 1000 | 806 | 964 | 0.12 | 0.23 | 0.18 | 0.1 |
| B | salt | 50 | 450 | 1000 | 733 | 944 | 0.14 | 0.20 | 0.16 | 0.12 |
| | | 75 | ” | 100 | 665 | 961 | 0.17 | 0.27 | 0.21 | 0.16 |

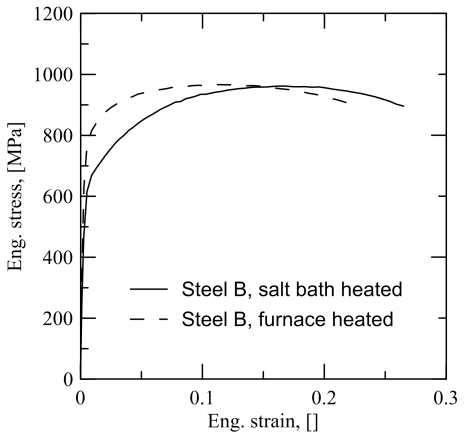


**Figure 5.32:** *Stress-strain curve for Steel B annealed at 850* °C*, quenched to 75* °C *and partitioned at 450* °C *for 100 s.*

of dimensions 25 mm x 6 mm, along with the results of the tensile tests, are presented in Table 5.2.

The mechanical properties of total elongation and ultimate tensile strength for the produced specimens are shown plotted on a diagram in Figure 5.33 containing the approximate property regimes for several advanced high strength steels [100]. It bears mentioning that the steels in Figure 5.33 cannot be put in a straightforward ranking order by a comparison based on two parameters. However, some conclusions can be drawn. The steels processed with the parameters in 5.2 are placed in and above the high-end TRIP region in terms of total elongation. When compared to dual-phase steels in the same tensile strength range, an even more favorable comparison can be made. The quenching and partitioning treatment has resulted in improved properties in terms of the tensile strength - total elongation ratio.

The heating rate of the steel has a significant impact on elongation; the furnace-heated specimens underwent necking at approximately 12 % elongation, while the corresponding salt bath heated specimens had uniform elongations of approximately 17 %. The behaviors of the steels during the initial stages of straining also differ considerably, as evidenced by the low average n-values in Table 5.2 of the furnace-treated specimens and the stress-strain curves in Figure 5.32. The salt bath-heated specimen has a lower yield point and a greater capability for strain hardening up until the point of necking. The effect of heating rate on the mechanical behavior is explained by the different ferrite recrystallization and austenite nucleation route of the material. The heating rate has been considerably more rapid in the salt bath heated specimens, leading to a more even distribution of recrystallized fine-sized ferrite grains, as shown in Figure 5.30b). The total holding time in the salt pot was 3 minutes, heating included ; compared to furnace heating, there has been less time for carbides to dissolve and parent austenite to nucleate and grow. Microstructural examination of the EBSD datasets reveals that a large fraction of the parent austenite in the salt pot specimens has remained completely untransformed to martensite.

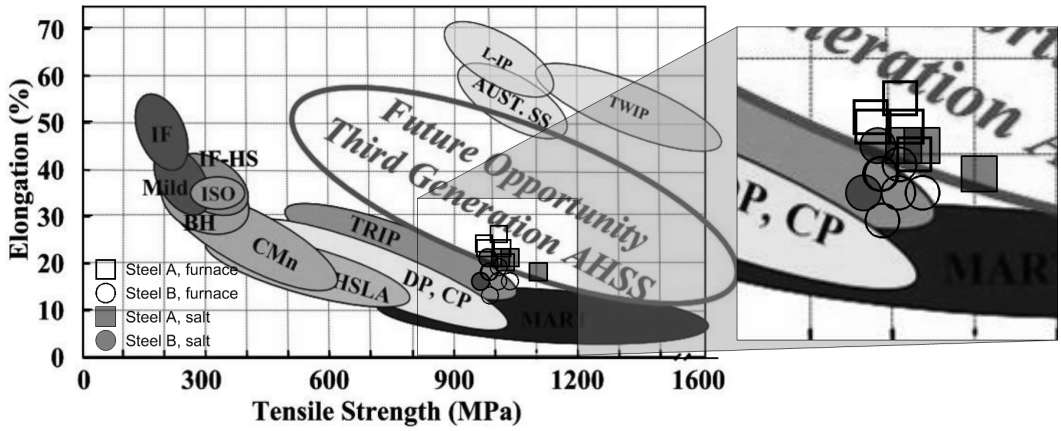


**Figure 5.33:** *The ultimate tensile strengths and total elongations of the specimens shown on a diagram containing the approximate property regimes for several advanced high strength steels.*

The effect of a partial martensitic transformation may also affect the behavior of the retained austenite during quenching. It has been established that the martensite forming in the studied steels after intercritical annealing is primarily single-packet: that is to say, only those variants that share a habit plane tend to form in each parent austenite grain during quenching. Assuming that any martensite variant forming as the result of stress or strain must also share a habit plane with the pre-existing martensite, the ability of the retained austenite to contribute to formability is severely hindered. The model by Patel and Cohen [101], experimentally verified by Kundu [79], predicts that the interaction energy between the stress state in the material and the martensitic transformation is different for each martensitic variant, depending on the orientation of the parent austenite grain and the direction of the applied stress. If martensite formation is also constrained to a single packet, the most energetically favorable variant may be unable to form, with the net effect of increasing the mechanical stability of retained austenite. This would mean that blocky, wholly untransformed retained austenite is less stable and has a greater ability to contribute to strain hardening during deformation, thanks to unimpaired variant selection.

# 6 Concluding remarks

The original research question presented in Chapter 1 was:

*Can aluminum alloyed steel processed with the Q&P route be used to produce DP steels with improved elongation and a microstructure with metastable retained austenite intermixed within the martensitic islands?*

The present knowledge of the effect of aluminum on the high-temperature thermodynamics in steels was not sufficient to predict the austenite-ferrite phase fractions at the studied intercritical annealing temperatures. Consequently, the parameters determined with information obtained from the literature survey did not result in Q&P microstructures. Experimental work revealed that even after extended annealing, there was more ferrite present in the microstructure than predicted by the existing thermodynamic models. The resulting high carbon content in the austenite phase - along with the small size of the austenite grains - lowered the starting temperature of martensite formation, preventing the formation of martensite altogether during the initial quenching in the preliminary heat treatments. By adjusting the Q&P heat treatment parameters to accommodate the observed low $M_s$ temperatures, dual-phase steels with partially quenched and partitioned microstructures could be obtained. The Q&P steels had higher total elongation values compared to conventional DP and TRIP steels.

From the viewpoint of metallurgy, the novel features in this work were the developed high-aluminum alloys and the studies on their annealing, quenching and partitioning behavior. The approach was to develop a high-end dual phase quenched and partitioned steel along with a suitable heat treatment, enhancing the formability of dual-phase steels while preserving their moderately high strength and retaining the possibility for hot dip galvanization. The resulting alloys have good mechanical properties with UTS in the 900-1000 MPa range and Ag in the 0.12-0.15 range, increasing formability when compared to conventional dual-phase steels while preserving high ultimate tensile strength. Aluminum was shown to prevent carbide formation for the duration of the partitioning cycle. It was shown that the steels are very sensitive to changes in the heating rate and soaking time when annealed at intercritical temperatures.

This work shows that the dual-phase approach can be used in conjunction with quenching and partitioning. An added benefit of the approach is that the initial quench temperatures can be much lower compared to a fully austenitized condition, requiring less drastic alterations to the industrial continuous annealing lines. With increased carbon content or alloy modification, the initial quench temperature could feasibly be lowered to room temperature, with no alterations necessary at all.

Varying the alloying contents remains the subject of future work. In addition, a more thorough analysis of the phase growth of austenite during intercritical annealing would pro-

vide useful knowledge, as well as more extensive variation of the initial quench temperatures.

From the viewpoint of crystallography, the novelty in this work is the fully automated iterative algorithm developed to measure the orientation relationship between austenite and martensite (or any daughter phase of austenite with a K-S type orientation relationship). The algorithm was shown to provide suitably accurate data for Markovian Cluster Analysis, after which parent austenite reconstruction could take place. The reconstruction algorithm requires little input from the user and was demonstrated to work well for fully austenitized and intercritically annealed microstructures that had undergone martensitic or bainitic transformations.

If the various orientation relationships occurring during recrystallization, austenite nucleation and martensitic transformation are known, then it becomes a simple matter to predict the texture of the final heat treated steel from that of the cold rolled starting material. Predictions could then be made on properties such as elastic modulus isotropy and possibly other mechanical properties.

Another venue for future work is the development and refinement of other analysis tools to benefit from new crystallographic information. After a full reconstruction of austenite texture from martensite, it would be possible to modify the various equations used for analysing dilatometric curves to take texture into account. This would provide a much more accurate basis i.e. for analysing the progress of the martensitic transformation from dilatometric curves.

The usefulness of the orientation relationship determination and parent austenite reconstruction algorithm extends well beyond the scope of this work. The knowledge of relationships between crystals in a polycrystalline material is an important part of steel metallurgy. The algorithm can shed a little light on this aspect of crystallography - hopefully leading to new questions and new research in turn.

# Bibliography


[1] T. Nyyssönen, M. Isakov, P. Peura, and V.-T. Kuokkala. Iterative determination of the orientation relationship between austenite and martensite from a large amount of grain pair misorientations. *Metallurgical and Materials Transactions A*, 47(6):2587–2590, 2016.

[2] J. Maki, J. Mahieu, B.C. De Cooman, and S. Claessens. Galvanisability of silicon free CMnAl TRIP steels. *Materials Science and Technology*, 19(1):125–131, jan 2003.

[3] H.K.D.H. Bhadeshia. *Worked examples in the Geometry of Crystals*. The Institute of Metals, 3 edition, 2006.

[4] A. Stormvinter, G. Miyamoto, T. Furuhara, P. Hedström, and A. Borgenstam. Effect of carbon content on variant pairing of martensite in FeC alloys. *Acta Materialia*, 60(20):7265–7274, dec 2012.

[5] S. Morito, H. Tanaka, R. Konishi, T. Furuhara, and T. Maki. The morphology and crystallography of lath martensite in Fe-C alloys. *Acta Materialia*, 51(6):1789–1799, apr 2003.

[6] J. G. Speer, D. K. Matlock, B. C. De Cooman, and J. G. Schroth. Carbon partitioning into austenite after martensite transformation. *Acta Materialia*, 51(9):2611–2622, may 2003.

[7] M. J. Santofimia, T. Nguyen-Minh, L. Zhao, R. Petrov, I. Sabirov, and J. Sietsma. New low carbon Q&P steels containing film-like intercritical ferrite. *Materials Science and Engineering: A*, 527(23):6429–6439, sep 2010.

[8] S. Zhou, K. Zhang, Y. Wang, J.F. Gu, and Y.H. Rong. High strength-elongation product of Nb-microalloyed low-carbon steel by a novel quenchingpartitioningtempering process. *Materials Science and Engineering: A*, 528(27):8006–8012, oct 2011.

[9] N. Zhong, X. Wang, Y. Rong, and L. Wang. Interface Migration between Martensite and Austenite during Quenching and Partitioning (Q&P) Process. *Journal of Materials Science and Technology*, 22(06):751–754, oct 2009.

[10] C. Zhao, D. Tang, H.-T. Jiang, S.-S. Jhao, and H. Li. Process Simulation and Microstructure Analysis of Low Carbon Si-Mn Quenched and Partitioned Steel. *Journal of Iron and Steel Research, International*, 15(4):82–85, jul 2008.

[11] J. Sun and H. Yu. Microstructure development and mechanical properties of quenching and partitioning (Q&P) steel and an incorporation of hot-dipping galvanization during Q&P process. *Materials Science and Engineering: A*, 586:100–107, dec 2013.

[12] M. J. Santofimia, L. Zhao, and J. Sietsma. Microstructural Evolution of a Low-Carbon Steel during Application of Quenching and Partitioning Heat Treatments after Partial Austenitization. *Metallurgical and Materials Transactions A*, 40(1):46–57, nov 2008.

[13] M. J. Santofimia, J. G. Speer, L. Zhao, and J. Sietsma. Model for the Annealing of Partial Martensite-Austenite Microstructures in Steels. *Solid State Phenomena*, 172-174:567–572, jun 2011.

[14] J. G. Speer, A. M. Streicher, D. K. Matlock, F. C. Rizzo, and G. Krauss. Quenching and partitioning: a fundamentally new process to create high strength TRIP sheet microstructures. In *Symposium on the Thermodynamics, Kinetics, Characterization and Modeling of: Austenite Formation and Decomposition*, pages 505–522, Chicago, 2003.

[15] E. de Moor, S. Lacroix, A. J. Clarke, J. Penning, and J. G. Speer. Effect of Retained Austenite Stabilized via Quench and Partitioning on the Strain Hardening of Martensitic Steels. *Metallurgical and Materials Transactions A*, 39(11):2586–2595, jul 2008.

[16] S. J. Kim, H. S. Kim, and B. C. De Cooman. Dilatometric Study of the Quench and Partitioning ( Q & P ) Process. *Materials Science and Technology*, pages 73–83, 2007.

[17] D. T. Pierce, D. R. Coughlin, D. L. Williamson, K. D. Clarke, A. J. Clarke, J. G. Speer, and E. De Moor. Characterization of transition carbides in quench and partitioned steel microstructures by Mössbauer spectroscopy and complementary techniques. *Acta Materialia*, 90:417–430, may 2015.

[18] E. De Moor, J. Penning, C. Föjer, A. J. Clarke, and J. G. Speer. Alloy design for enhanced austenite stabilization via quenching and partitioning. *Proc. of the Int. Conf. on New Developments in Advanced High-Strength Sheet Steels*, pages 15–18, 2008.

[19] M. J. Santofimia, L. Zhao, R. Petrov, and J. Sietsma. Characterization of the microstructure obtained by the quenching and partitioning process in a low-carbon steel. *Materials Characterization*, 59(12):1758–1764, dec 2008.

[20] M. J. Santofimia, L. Zhao, R. Petrov, C. Kwakernaak, W. G. Sloof, and J. Sietsma. Microstructural development during the quenching and partitioning process in a newly designed low-carbon steel. *Acta Materialia*, 59(15):6059–6068, sep 2011.

[21] M. Kähkönen, E. De Moor, J. Speer, and G. Thomas. Carbon and Manganese Effects on Quenching and Partitioning Response of CMnSi-Steels. *SAE International Journal of Materials and Manufacturing*, 8(2):2015–01–0530, apr 2015.

[22] H.K.D.H. Bhadeshia and R. Honeycombe. *Steels.* 2006.

[23] Bevis Hutchinson, Joacim Hagström, Oskar Karlsson, David Lindell, Malin Tornberg, Fredrik Lindberg, and Mattias Thuvander. Microstructures and hardness of as-quenched martensites (0.10.5%C). *Acta Materialia*, 59(14):5845–5858, 2011.

[24] Oleg D. Sherby, J. Wadsworth, D.R. Lesuer, and C.K. Syn. Structure and Hardness of Martensite in Quenched Fe-C Steels. *Materials Science Forum*, 638-642:160–167, jan 2010.

[25] W. Steven and A. G. Haynes. The temperature of formation of martensite and bainite in low alloy steel. *Journal of the Iron and Steel Institute*, (183):349–359, 1956.

[26] H. K. D. H. Bhadeshia. Thermodynamic extrapolation and martensite-start temperature of substitutionally alloyed steels. *Metal Science*, 15(4):178–180, apr 1981.

[27] H. K. D. H. Bhadeshia. Driving force for martensitic transformation in steels. (April):175–177, 1981.

[28] G. Ghosh and G. B. Olson. Kinetics of F.C.C. B.C.C. heterogeneous martensitic nucleationI. The critical driving force for athermal nucleation. *Acta Metallurgica et Materialia*, 42(10):3361–3370, oct 1994.

[29] T. Cool and H. K. D. H. Bhadeshia. Modelling the Mechanical Properties in the HAZ of Power Plant Steels I: Bayesian Neural Network Analysis of Proof Strength. In H. Cerjak, editor, *Mathematical Modelling of Weld Phenomena, Volume 3*, pages 403–443. Maney Publishing, 1997.

[30] M. Peet. Prediction of martensite start temperature. *Materials Science and Technology*, 31(11):1370–1375, aug 2015.

[31] H. K. D. H. Bhadeshia. Neural Networks in Materials Science. *ISIJ International*, 39(10):966–979, may 1999.

[32] C. Capdevila, F. G. Caballero, and C. García de Andrés. Determination of Ms Temperature in Steels: A Bayesian Neural Network Model. *ISIJ International*, 42(8):894–902, may 2002.

[33] M. Izumiyama, M. Tsuchiya, and Y. Imai. Effects of Alloying Element on Supercooled A3 Transformation. *Journal of the Japan Institute of Metals and Materials*, 34(3):291–295, apr 1970.

[34] G. Ghosh and G.B. Olson. Kinetics of F.c.c. b.c.c. heterogeneous martensitic nucleationII. Thermal activation. *Acta Metallurgica et Materialia*, 42(10):3371–3379, oct 1994.

[35] H. Yang and H. K. D. H. Bhadeshia. Austenite grain size and the martensite-start temperature. *Scripta Materialia*, 60(7):493–495, apr 2009.

[36] D. P. Koistinen and R. E. Marburger. A general equation prescribing the extent of the austenite-martensite transformation in pure iron-carbon alloys and plain carbon steels. *Acta Metallurgica*, 7:59–60, 1959.

[37] C. L. Magee. Nucleation of Martensite. In *Phase Transformations*, pages 115–156, Ohio, 1970. ASM.

[38] S. A. Khan and H. K. D. H. Bhadeshia. Kinetics of Martensitic transformation in partially bainitic 300M steel. *Materials Science and Engineering: A*, 129(2):257–272, 1990.

[39] S. M. van Bohemen and J. Sietsma. Effect of composition on kinetics of athermal martensite formation in plain carbon steels. *Materials Science and Technology*, 25(8):1009–1012, aug 2009.

[40] S. M. Van Bohemen and J. Sietsma. Martensite Formation in Partially and Fully Austenitic Plain Carbon Steels. *Metallurgical and Materials Transactions A*, 40(5):1059–1068, feb 2009.

[41] S.-J. Lee and C. J. Van Tyne. A Kinetics Model for Martensite Transformation in Plain Carbon and Low-Alloyed Steels. *Metallurgical and Materials Transactions A*, 43(2):422–427, sep 2011.

[42] M. J. Santofimia, J. G. Speer, A. J. Clarke, L. Zhao, and J. Sietsma. Influence of interface mobility on the evolution of austenitemartensite grain assemblies during annealing. *Acta Materialia*, 57(15):4548–4557, sep 2009.

[43] H. Y. Li, X. W. Lu, W. J. Li, and X. J. Jin. Microstructure and Mechanical Properties of an Ultrahigh-Strength 40SiMnNiCr Steel during the One-Step Quenching and Partitioning Process. *Metallurgical and Materials Transactions A*, 41(5):1284–1300, feb 2010.

[44] A. Hultgren. Isothermal Transformation of Austenite. *Transaction of the ASM*, 39:915–989, 1947.

[45] J. A. Lobo and G. H. Geiger. Thermodynamics and solubility of carbon in ferrite and ferritic Fe-Mo alloys. *Metallurgical Transactions A*, 7(9):1347–1357, sep 1976.

[46] J. A. Lobo and G. H. Geiger. Thermodynamics of carbon in austenite and Fe-Mo austenite. *Metallurgical Transactions A*, 7(9):1359–1364, sep 1976.

[47] E. De Moor, J. G. Speer, D. K. Matlock, J.-H. Kwak, and S.-B. Lee. Quenching and Partitioning of CMnSi Steels Containing Elevated Manganese Levels. *steel research international*, 83(4):322–327, apr 2012.

[48] L. Chang and G. D. W. Smith. The Silicon Effect in the Tempering of Martensite in Steels. *Le Journal de Physique Colloques*, 45(C9):C9–397–C9–401, dec 1984.

[49] Y. Hirotsu and S. Nagakura. Electron Microscopy and Diffraction Study of the Carbide Precipitated at the First Stage of Tempering of Martensitic Medium Carbon Steel. *Transactions of the Japan Institute of Metals*, 15(2):129–134, 1974.

[50] R. G. Baker and J. Nutting. Precipitation processes in steels. *Iron and Steel Institute, London*, 1959.

[51] Y. Hirotsu and S. Nagakura. Crystal structure and morphology of the carbide precipitated from martensitic high carbon steel during the first stage of tempering. *Acta Metallurgica*, 20(4):645–655, apr 1972.

[52] J. G. Speer, E. De Moor, K. O. Findley, D. K. Matlock, B. C. De Cooman, and D. V. Edmonds. Analysis of Microstructure Evolution in Quenching and Partitioning Automotive Sheet Steel. *Metallurgical and Materials Transactions A*, 42(12):3591–3601, sep 2011.

[53] G. M. Michal and J. A. Slane. The kinetics of carbide precipitation in silicon-aluminum steels. *Metallurgical Transactions A*, 17(8):1287–1294, aug 1986.

[54] G. Miyamoto, J. Oh, K. Hono, T. Furuhara, and T. Maki. Effect of partitioning of Mn and Si on the growth kinetics of cementite in tempered Fe0.6 mass% C martensite. *Acta Materialia*, 55(15):5027–5038, sep 2007.

[55] J. H. Jang, I. Kim, and H. K. D. H. Bhadeshia. $\epsilon$-Carbide in alloy steels: First-principles assessment. *Scripta Materialia*, 63(1):121–123, 2010.

[56] F. HajyAkbary, J. Sietsma, G. Miyamoto, T. Furuhara, and M. J. Santofimia. Interaction of carbon partitioning, carbide precipitation and bainite formation during the Q&P process in a low C steel. *Acta Materialia*, 104:72–83, 2016.

[57] D. T. Pierce, D. R. Coughlin, D. L. Williamson, J. Kähkönen, A. J. Clarke, K. D. Clarke, J. G. Speer, and E. De Moor. Quantitative investigation into the influence of temperature on carbide and austenite evolution during partitioning of a quenched and partitioned steel. *Scripta Materialia*, 121:5–9, 2016.

[58] X. D. Wang, W. Z. Xu, Z. H. Guo, L. Wang, and Y. H. Rong. Carbide characterization in a Nb-microalloyed advanced ultrahigh strength steel after quenchingpartitioningtempering process. *Materials Science and Engineering: A*, 527(15):3373–3378, 2010.

[59] Y. Wang, Z. Guo, N. Chen, and Y. Rong. Deformation Temperature Dependence of Mechanical Properties and Microstructures for a Novel QuenchingPartitioningTempering Steel. *Journal of Materials Science & Technology*, 29(5):451–457, may 2013.

[60] A. Borgenstam and M. Hillert. Activation energy for isothermal martensite in ferrous alloys. *Acta Materialia*, 45(2):651–662, 1997.

[61] A. Borgenstam and M. Hillert. Nucleation of isothermal martensite. *Acta Materialia*, 48(11):2777–2785, 2000.

[62] G.V. Kurdjumov. *Journal of the Iron and Steel Institute*, 195:26, 1960.

[63] J. Mahieu, B. C. De Cooman, and J. Maki. Phase transformation and mechanical properties of si-free CMnAl transformation-induced plasticity-aided steel. *Metallurgical and Materials Transactions A*, 33(8):2573–2580, aug 2002.

[64] M. J. Santofimia, L. Zhao, and J. Sietsma. Model for the interaction between interface migration and carbon diffusion during annealing of martensiteaustenite microstructures in steels. *Scripta Materialia*, 59(2):159–162, jul 2008.

[65] D. De Knijf, M. J. Santofimia, H. Shi, V. Bliznuk, C. Föjer, R. Petrov, and W. Xu. In situ austenitemartensite interface mobility study during annealing. *Acta Materialia*, 90:161–168, may 2015.

[66] Thermo-Calc Software TCFE7 Steels/Fe-alloys database version 7, (Accessed 10 Nov 2015).

[67] J.-O. Andersson, T. Helander, L. Höglund, P. Shi, and B. Sundman. Thermo-Calc & DICTRA, computational tools for materials science. *Calphad*, 26(2):273–312, jun 2002.

[68] N. Saunders, U. K. Z. Guo, X. Li, A. P. Miodownik, and J. Ph. Schillé. Using JMatPro to model materials properties and behavior. *JOM*, 55(12):60–65, dec 2003.

[69] J. Hamada, M. Enomoto, T. Fujishiro, and T. Akatsuka. In-Situ Observation of the Growth of Massive Ferrite in Very Low-Carbon Fe-Mn and Ni Alloys. *Metallurgical and Materials Transactions A*, 45(9):3781–3789, may 2014.

[70] L. Cheng, K. M. Wu, X. L. Wan, and R. Wei. In-situ observation on the growth of Widmanstätten sideplates in an FeCMn steel. *Materials Characterization*, 87:86–94, jan 2014.

[71] M. J. Santofimia, C. Kwakernaak, W. G. Sloof, L. Zhao, and J. Sietsma. Experimental study of the distribution of alloying elements after the formation of epitaxial ferrite upon cooling in a low-carbon steel. *Materials Characterization*, 61(10):937–942, oct 2010.

[72] E.C. Bain. The nature of martensite. *Transactions of the American Institute of Mining, Metallurgical, and Petroleum Engineers*, 70(25), 1924.

[73] P. M. Kelly. Crystallography of lath martensite in steels. *Materials Transactions, JIM*, 33(3):235–242, 1992.

[74] G. Miyamoto, N. Takayama, and T. Furuhara. Accurate measurement of the orientation relationship of lath martensite and bainite by electron backscatter diffraction analysis. *Scripta Materialia*, 60(12):1113–1116, jun 2009.

[75] G. Miyamoto, N. Iwata, N. Takayama, and T. Furuhara. Mapping the parent austenite orientation reconstructed from the orientation of martensite by EBSD and its application to ausformed martensite. *Acta Materialia*, 58(19):6393–6403, nov 2010.

[76] G. Miyamoto, N. Iwata, N. Takayama, and T. Furuhara. Quantitative analysis of variant selection in ausformed lath martensite. *Acta Materialia*, 60(3):1139–1148, feb 2012.

[77] N. Takayama, G. Miyamoto, and T. Furuhara. Effects of transformation temperature on variant pairing of bainitic ferrite in low carbon steel. *Acta Materialia*, 60(5):2387–2396, mar 2012.

[78] P. Suikkanen, C. Cayron, A. J. DeArdo, and L. P. Karjalainen. Crystallographic Analysis of Isothermally Transformed Bainite in 0.2C2.0Mn1.5Si0.6Cr Steel Using EBSD. *Journal of Materials Science & Technology*, 29(4):359–366, apr 2013.

[79] S. Kundu. *Transformation Strain and Crystallographic Texture in Steels*. PhD thesis, Darwin College, Cambridge, 2007.

[80] S. Takaki, K. Fukunaga, J. Syarif, and T. Tsuchiyama. Effect of Grain Refinement on Thermal Stability of Metastable Austenitic Steel. *Materials Transactions*, 45(7):2245–2251, 2004.

[81] C. Cayron, B. Artaud, and L. Briottet. Reconstruction of parent grains from EBSD data. *Materials Characterization*, 57(4-5):386–401, dec 2006.

[82] E. Gomes and L. Kestens. Fully automated orientation relationship calculation and prior austenite reconstruction by random walk clustering. *IOP Conference Series: Materials Science and Engineering*, 82(1):012059, apr 2015.

[83] S. van Dongen. *Graph Clustering by Flow Simulation.* PhD thesis, University of Utrecht, 2000.

[84] Y. Mi. Effect of Cu, Mo, Si on the content of retained austenite of austempered ductile iron. *Scripta Metallurgica et Materialia*, 32(9):1313–1317, 1995.

[85] E. Jimenez-Melero, N.H. van Dijk, L. Zhao, J. Sietsma, S.E. Offerman, J.P. Wright, and S. van der Zwaag. The effect of aluminium and phosphorus on the stability of individual austenite grains in TRIP steels. *Acta Materialia*, 57(2):533–543, 2009.

[86] W. Bleck, K. Hulka, and K. Papamentellos. Effect of niobium on the mechanical properties of TRIP steels. *Materials science forum*, 284-286:327–334, 1998.

[87] Y. Han, S. Kuang, H.-S. Liu, Y.-H. Jiang, and G.-H. Liu. Effect of Chromium on Microstructure and Mechanical Properties of Cold Rolled Hot-dip Galvanizing DP450 Steel. *Journal of Iron and Steel Research, International*, 22(11):1055–1061, 2015.

[88] C. F. Jatczak, J. A. Larsen, and S. W. Shin. *Retained Austenite and Its Measurements by X-Ray Diffraction; SP-453.* Society of Automotive Engineers, Inc, 1980.

[89] N.Y. Zolotorevsky, S.N. Panpurin, A.A. Zisman, and S.N. Petrov. Effect of ausforming and cooling condition on the orientation relationship in martensite and bainite of low carbon steels. *Materials Characterization*, 107:278–282, sep 2015.

[90] F. Bachmann, Ralf Hielscher, and Helmut Schaeben. Texture Analysis with MTEX Free and Open Source Software Toolbox. *Solid State Phenomena*, 160:63–68, feb 2010.

[91] Z.-D. Li, G. Miyamoto, Z.-G. Yang, and T. Furuhara. Nucleation of austenite from pearlitic structure in an Fe0.6C1Cr alloy. *Scripta Materialia*, 60(7):485–488, 2009.

[92] L. Ryde. Application of EBSD to analysis of microstructures in commercial steels. *Materials Science and Technology*, 22(11):1297–1306, 2006.

[93] G. Thewlis. Classification and quantification of microstructures in steels. *Materials Science and Technology*, 20(2):143–160, 2004.

[94] P. Lehto, J. Romanoff, H. Remes, and T. Sarikka. Characterisation of local grain size variation of welded structural steel. *Welding in the World*, 60(4):673–688, jul 2016.

[95] L. Ryde, J. Hagström, and W. B. Hutchinson. An EBSD Study of Austenite Formation and Stability in Low-Alloy TRIP Steels. *Materials Science Forum*, 550:321–326, 2007.

[96] P. M. Kelly, A. Jostsons, and R. G. Blake. The orientation relationship between lath martensite and austenite in low carbon, low alloy steels. *Acta Metallurgica et Materialia*, 38(6):1075–1081, jun 1990.

[97] J. Z. Zhao, C. Mesplont, and B. C. De Cooman. Quantitative analysis of the dilatation during an isothermal decomposition of austenites. *Materials Science and Engineering: A*, 332(1):110–116, 2002.

[98] H. K. D. H. Bhadeshia. Thermodynamic analysis of isothermal transformation diagrams. *Metal Science*, 16(3):159–166, mar 1982.

[99] ISO 2566-1:1984(E) Steel – Conversion of elongation values – Part 1: Carbon and low alloy steels, 1984.

[100] Third Generation Advanced High Strength Steel (AHSS). *Research and Development Solicitation*, 2006.

[101] J. R. Patel and M. Cohen. Criterion for the action of applied stress in the martensitic transformation. *Acta Metallurgica*, 1(5):531–538, sep 1953.

[102] J. R. Lacher and R. H. Fowler. The Statistics of the Hydrogen-Palladium System. *Mathematical Proceedings of the Cambridge Philosophical Society*, 33(04):518–523, oct 1937.

[103] R. H. Fowler and E. A. Guggenheim. *Statistical Thermodynamics: A Version of Statistical Mechanics for Students of Physics and Chemistry*. Cambridge University Press (printed by W. Lewis), 1939.

[104] G. J. Shiflet, J. R. Bradley, and H. I. Aaronson. A re-examination of the thermodynamics of the proeutectoid ferrite transformation in Fe-C alloys. *Metallurgical Transactions A*, 9(7):999–1008, jul 1978.

[105] M. Peet and H. K. D. H. Bhadeshia. MUCG83, 2006.

# 7 Appendix 1: Thermodynamic calculation of $M_s$

The thermodynamic calculation of $M_s$ in the model by Bhadeshia et al. [26] is based on the original formalisms by Lacher [102], Fowler and Guggenheim [103] (hereafter referred to as the LFG formalisms) adapted to the phase transformations of steel by Shiflet et al. [104]. They wrote the free energy of ferrite $F_\alpha$ as:

$$F_\alpha = RT(x_\alpha(ln(a_\alpha) + (1 - x_\alpha)ln(1 - x_\alpha)) + x_\alpha F_c^G + (1 - x_\alpha)F_{Fe}^\alpha \tag{7.1}$$

in which $R$ is the gas constant, $T$ is the temperature in K, $a_\alpha$ is the activity of carbon in ferrite, $x_\alpha$ is the molar fraction of carbon in ferrite, $F_c^G$ is the free energy of pure graphite in J and $F_{Fe}^\alpha$ is the free energy of pure iron in J/mol.

In the original work by Shiflet et al. [104], the activity of carbon in ferrite was extrapolated to accommodate their finding of the carbon-carbon interaction energy in ferrite $w_\alpha$ as negative [26, 104] and was only suitable for small carbon contents. Later, Bhadeshia [26] analysed more accurate thermodynamic data by Lobo and Geiger [45, 46] to provide a positive value for $w_\alpha$, allowing the use of the unmodified equation by Shiflet et al. [104] to represent $a_\alpha$:

$$ln(a_\alpha) = 3\ln\frac{3 - 4x_\alpha}{x_\alpha} + \frac{4w_\alpha}{RT} + 4\ln\left(\frac{\delta_\alpha - 3 + 5x_\alpha}{\delta_\alpha + 3 - 5x_\alpha}\right) + \frac{\Delta\overline{H}_\alpha - \Delta S_\alpha T}{RT} \tag{7.2}$$

where $w_\alpha$ = 48570 J/mol is the pairwise carbon-carbon interaction energy in J/mol, $\Delta\overline{H}_\alpha$ = 111918 J/mol is the partial molar heat of solution of carbon in ferrite, $\Delta S_\alpha$ = 51.44 J/(molK) is the partial non-configurational entropy of solution of carbon in ferrite and $\delta_\alpha$ is given as:

$\delta_\alpha = |9 - 6x(2J_\alpha + 3) + (9 + 16J_\alpha)x^2|^{1/2}$

where

$J_\alpha = 1 - e^{(-\omega_\alpha/RT)}$

Shiflet et al. [104] then wrote the free energy of austenite according to the LFG formalisms as:

$$\begin{aligned} F^\gamma = {} & 5RT[(1 - x_\gamma)\ln((1 - x_\gamma) - (1 - 2x_\gamma)\ln(1 - 2x_\gamma) - x_\gamma \ln x_\gamma] \\ & + 6RT\left[x_\gamma \ln\left(\frac{\delta_\gamma - 1 + 3x_\gamma}{\delta_\gamma + 1 - 3x_\gamma}\right) + (1 - x_\gamma)\ln\left(\frac{1 - 2J_\gamma + (4J_\gamma - 1)x_\gamma - \delta_\gamma}{2J_\gamma(2x_\gamma - 1)}\right)\right] \\ & + x_\gamma(\Delta\overline{H}_\gamma - \Delta S_\gamma T + 6w_\gamma + F_c^G) + (1 - x_\gamma)F_{Fe}^\gamma \end{aligned} \tag{7.3}$$

where $w_\gamma$ is the pairwise carbon-carbon interaction energy in J/mol in austenite. This variable is phase composition dependent and was evaluated by Bhadeshia in [27]. The effect of each compositional element is averaged to provide $w_\gamma$. The relations between alloying element concentration and the interaction energy were determined by Bhadeshia in [27] and

were obtained for C, Si, Mn, Ni, Mo, Cr, V, Co, Cu, Al and W from the freeware program MUCG83 developed by Peet and Bhadeshia [105].

The $\Delta\overline{H}_\gamma = 38575$ J/mol is the partial molar heat of solution of carbon in austenite, $\Delta S_\gamma = 13.48$ J/(molK) is the partial non-configurational entropy of solution of carbon in austenite and $\delta_\gamma$ is given as:

$$\delta_\gamma = |1 - 2(1 + 2J_\gamma)x + (1 + 8J_\gamma)x^2|^{1/2}$$

and

$$J_\gamma = 1 - e^{(-\overline{\omega}_\gamma/RT)}$$

As discussed in Chapter 2.1, the driving force of the martensitic transformation is thought of as the difference between the free energies of the austenite phase and a supersaturated ferrite phase of the same composition, supplemented by the Zener ordering term. The driving force is then given as $\Delta F_{M_s}^{\gamma\rightarrow\alpha'} = F_\alpha - F_\gamma + \Delta f^*$. Using Equations 7.1 and 7.3 with Eq. 7.2 as $\ln a_\alpha$ gives:

$$\begin{aligned}\Delta F_{M_s}^{\gamma\rightarrow\alpha'} = 2xRT\ln(x) + x|\Delta\overline{H}_\alpha - \overline{H}_\gamma - (\Delta S_\alpha - \Delta S_\gamma)T + 4\omega_\alpha - 6\overline{\omega}_\gamma| \\ - 4RT(1-x)\ln(1-x) \\ + 5RT(1-2x)\ln(1-2x)| \\ - 6RTx\ln\left|\frac{\delta_\gamma - 1 + 3x}{\delta_\gamma + 1 - 3x}\right| \\ - 6RT(1-x)\ln\left|\frac{1 - 2J_\gamma + (4J_\gamma - 1)x - \delta_\gamma}{2J_\gamma(2x-1)}\right| \\ + 3RTx\ln(3-4x) + 4RTx\ln\left|\frac{\delta_\alpha - 3 + 5x}{\delta_\alpha + 3 - 5x}\right| \\ + (1-x)(F_{Fe}^\alpha - F_{Fe}^\gamma) + \Delta f^* \quad (7.4)\end{aligned}$$

in which $F_{Fe}^\alpha - F_{Fe}^\gamma$ can simply be written as $\Delta F_{Fe}^{\gamma\rightarrow\alpha}$. The effect of alloying on $\Delta F_{Fe}^{\gamma\rightarrow\alpha}$ (the Gibbs free energy difference between austenite and ferrite in pure iron) is further divided into a magnetic and non-magnetic component. The effect of alloying elements is taken into account by estimating their effect on the displacement in temperature at which the energy change in pure iron is evaluated. $\Delta F_{Fe}^{\gamma\rightarrow\alpha}$ is replaced with $\Delta F_{Fe,Y_i}^{\gamma\rightarrow\alpha}$, which is written as:

$$\Delta F_{Fe,Y_i}^{\gamma\rightarrow\alpha} = |141\Sigma Y_i(\Delta T_{mag_i} - \Delta T_{NM_i}) + \Delta F_{Fe}^{\gamma\rightarrow\alpha}\{T - 100\Sigma Y_i\Delta T_{mag_i}\}| \quad (7.5)$$

In Equation 7.5, $\Delta T_{mag_i}$ and $\Delta T_{NM_i}$ represent the displacement in the temperature at which the free energy change accompanying the $\gamma \rightarrow \alpha$ transformation in pure iron (i.e. $\Delta F_{Fe}^{\gamma\rightarrow\alpha}$) is evaluated in order to allow for the changes (per at.-%) due to alloying element effects on the magnetic and non-magnetic components of $\Delta F_{Fe}^{\gamma\rightarrow\alpha}$, respectively. The variables $Y_i$ were determined by Bhadeshia in [27] and were obtained from the program MUCG83Peet2006.

Equation 7.4 gives the available driving force for the martensitic transformation. This is calculated for a range of temperatures and then compared to a prediction for the critical driving force necessary to initiate the martensitic transformation. In this work, the pre-

diction for the driving force $\Delta F_{M_s}^{\gamma \rightarrow \alpha'*}$ in J/mol is taken as the linear relationship given by Equation 7.6:

$$\Delta F_{M_s}^{\gamma \rightarrow \alpha'*} = -1120 - 10568x + 94; \tag{7.6}$$

where $x$ is the carbon content of the alloy in at-%. Equation 7.6 was obtained from the freeware program MUCG83 [105].

Tampereen teknillinen yliopisto
PL 527
33101 Tampere

Tampere University of Technology
P.O.B. 527
FI-33101 Tampere, Finland

ISBN 978-952-15-3892-6
ISSN 1459-2045